INTERFACES, INTERPHASES, AND OTHER MATERIAL INTERACTIONS IN LITHIUM ION BATTERIES

A Thesis
Presented to
The Academic Faculty

By

Naoki Nitta

In Partial Fulfillment
of the Requirements for the Degree
Doctor of Philosophy in the
School of Materials Science and Engineering

Georgia Institute of Technology

December, 2016

Interfaces, Interphases, and Other Material Interactions in Li-ion Batteries

Approved by:

Dr. Gleb Yushin
School of Materials Science and Engineering
Georgia Institute of Technology

Dr. Thomas Fuller
School of Chemical and Biomolecular Engineering
Georgia Institute of Technology

Dr. Faisal Alamgir
School of Materials Science and Engineering
Georgia Institute of Technology

Dr. Paul Kohl
School of Chemical and Biomolecular Engineering
Georgia Institute of Technology

Dr. Igor Luzinov
Department of Materials Science and Engineering
Clemson University

Date Approved: September 16, 2016

ACKNOWLEDGEMENTS

I would like to thank my family and friends for their support, and my colleagues and advisors for their guidance and encouragement. Special thanks to my grandfather Takashi Sakaguchi for showing me the working of a Cu-Zn battery in my third grade science project, Dr. Lisa Biswal for her support, and my current advisor Dr. Gleb Yushin for giving me the support, guidance, and freedom to develop into the researcher I am now.

Almost all of the work would also have been impossible without extensive collaboration and teamwork. Commercial cell degradation analysis was performed with extensive collaboration. Jung Tae Lee performed TEM and FIB/SEM analysis, Kwangsup Eom and Tapesh Joshi performed electrochemical analysis, and Jim Benson performed resistance measurements and ToF-SIMS. Hyea Kim took the lead in investigating LiFSI electrolytes for Li-S batteries. Thanks also to Cindy Huang, Jeremy Cao, Garrett Gresham, Gabriel Waksman, and Lina Zikas for assistance in various aspects of the experimental work; Enbo Zhao and Alexandre Magasinski for TEM work; Danni Lei, Hongryun Jung, and Daniel Gordon for FTIR work; and Anirudh Ramanujapuram for TGA work. Thanks also to all my lab-mates for helpful discussion and good times; Rajiv Jaini for helpful input on EIS; and Tom Fuller, Igor Luzinov, and Vojtech Svboda for guidance.

This thesis was partially supported by the NSF IGERT NESAC program and Honda R&D Americas.

TABLE OF CONTENTS

LIST OF TABLES

LIST OF FIGURES

LIST OF SYMBOLS AND ABBREVIATIONS

AES - Auger Electron Spectroscopy

BE - Binding Energy (in XPS analysis)

CE - coulombic efficiency (in electrochemical charge/discharge)

CMC – Carboxymethyl Cellulose (polymer binder material)

CNT – Carbon Nanotube

DEC – Diethyl Carbonate (electrolyte solvent)

DIOX – Dioxolane

DMC – Dimethyl Carbonate (electrolyte solvent)

DME – Dimethoxyethane (monoglyme)

DMSO – Dimethyl Sulfoxide

EC – Ethylene Carbonate (electrolyte solvent)

EDLC - Electrochemical Double-Layer Capacitance

EDS – Energy Dispersive X-Ray Spectroscopy

EELS – Electron Energy Loss Spectroscopy

EIS - Electrochemical Impedance Spectroscopy

EMC – Ethyl Methyl Carbonate (electrolyte solvent)

ExG – Exfoliated Graphite

FEC – Fluoroethylene Carbonate (electrolyte solvent)

FWHM – Full Width Half Maximum

LCO – Lithium Cobalt Oxide (Li-ion cathode material)

LFP – Lithium Iron Phosphate (Li-ion cathode material)

LiTFSI – Lithium Bis(trifluoromethane)sulfonimide

LMO – Lithium Manganese Oxide (Li-ion cathode material)

MCNP – Mesoporous Carbon Nano-Powder

NCA – Lithium Nickel Cobalt Aluminum Oxide (Li-ion cathode material)

NEXAFS - Near Edge X-ray Absorption Fine Structure

NMC – Lithium Nickel Manganese Cobalt Oxide (Li-ion cathode material)

OD - Outer Diameter

PB – Pure Black

P-C – Phosphorus Carbon Composite

PAA – Polyacrylic Acid

PEI – Polyetherimide

PES – Prop-1-ene-1,3-Sultone

PMMA – Polymethyl Methacrylate

PVDF – Polyvinylidene Fluoride

SEI – Solid Electrolyte Interphase

SEM – Scanning Electron Microscopy

SOC – State of Charge

TEM – Transmission Electron Microscopy

TGA – Thermogravimetric Analysis

THF – Tetrahydrofuran

ToF-SIMS – Time of Flight Secondary Ion Mass Spectrometry

UHV – Ultra High Vacuum

VC – Vinylene Carbonate (electrolyte solvent additive)

XPS – X-Ray Photoelectron Spectroscopy

XRD – X-Ray Diffraction

SUMMARY

Performance and long-term cycle stability of composite battery electrodes depends on interactions of active materials with electrolyte, binders and conductive additives. This thesis investigates how such interactions affect the performance of Li-ion battery electrodes using state of the art characterization techniques. First, X-ray Photoelectron Spectroscopy (XPS) was used to analyze the solid electrolyte interphase (SEI) layer in commercial and novel Li-ion battery chemistries. Ar+ ion etching was investigated as a method of measuring the thickness of the SEI, and compared with Secondary Ion Mass Spectroscopy (SIMS) and Focus Ion Beam (FIB) etching. The chemistry of the SEI decomposition was also analyzed via the chemical shifts in the detailed XPS spectra. A similar analysis was also performed on a new electrolyte chemistry for Li-S cells. Next, phosphorus-carbon (P-C) composite anodes were synthesized and systematically investigated. In particular, the chemical and mechanical interactions between the conductive carbon additives, binders, P-C composite, and solvents in electrolyte and slurry were investigated. Selected binders showed superior performance on the basis of strength, hardness and adhesion. In addition, complete removal of n-methyl-2-pyrrolidone (NMP) solvent from the electrodes were found to be critical for stability improvements.

Chapter 1. Introduction

Portable electrochemical energy storage has drastically transformed our society through portable electronics. With the advent of wearable electronics, advances in portable energy storage will continue to change our world by enabling smarter devices that collect, store, and process more and better data. Meanwhile the resurgence of electric powered vehicles may solve intensifying urban air pollution and vastly reduce our carbon footprint. As technology develops, there is no question that portable energy storage will only become more valuable.

Currently, the energy storage technology of choice for portable electronics and electric powered automobiles is the Li-ion battery, due to its high energy density and decreasing costs from improving economies of scale. However, issues such as cost, safety, and limitations on operating temperature range continue to restrict its application. For electric vehicle applications, issues of charge/discharge cycle life, aging, and charge rate limitations are also causes of slow market growth.

The defining characteristics of the Li-ion battery are dictated by its use of Li. The Li-ion battery is charged and discharged by shuttling Li^+ ions between and anode and cathode which have different Li potentials. Li is the lightest metal per mol, the second smallest single charge cation, and has the lowest reduction potential of any metal. Especially when compared to classical aqueous batteries using H^+ or OH^- as active ions, Li-ion batteries have a fundamental advantage in achieving the largest voltage, resulting in their high energy density. However, the large voltage difference between the anode and the cathode also comes at a cost, as even organic electrolytes are not

thermodynamically stable across a 4+ volt range. In fact, the Li-ion battery became commercially viable only due to the serendipitous development of a stable solid electrolyte interphase (SEI) layer on the anode surface.

Scientifically and technologically, Li-ion batteries present a steep challenge. Whereas aqueous electrochemistry is well developed, Li-ion electrochemistry involves metastable material combinations of various organic and inorganic materials. Given the numerous combinations of materials and chemicals possible, changing one material can have unpredictable consequences. Thus each improvement comes with a new set of chemical, mechanical, and electrical issues which must be solved in turn. Yet the potential reward is just as steep.

Chapter 2. Background

2.1. Li-ion Battery Materials

The standard layout of a traditional Li-ion battery, as initially developed in the early 1990's is as follows. Li metal would serve as the anode with the lowest possible voltage, but causes safety issues due to the possibility of dendrite growth during Li plating. Such dendrites may either protrude out of the metal or be deposited as a result of the local field concentration gradients and other factors [1-3]. Li dendrites can then poke through the separator and short circuit the battery and cause the battery to overheat and catch fire. Thus the traditional Li-ion battery utilizes large (1-30 micron) graphite particles, which host Li by intercalation into its interstitials and offer fast Li transport, good electrical conductivity, and a potential only slightly higher than that of Li metal. These electrodes are held together using PVDF polymer binder, and nano-sized carbon black particles are used to provide good electrical contacts between the particles. This composite is itself casted on a copper foil current collector, due to copper's good conductivity, relatively low cost, and electrochemical inertness with respect to Li^+ ions at low potentials.

A traditional electrolyte solvent is composed of a mixture of ethylene carbonate (EC) with linear carbonates, typically Dimethyl Carbonate (DMC) and/or Diethyl Carbonate (DEC). Mixing solvents is essential for acceptable electrolyte performance, as no single solvent has the requisite properties of a well-functioning electrolyte. Modern commercial electrolytes typically have over six different solvents in their mixture. The traditional electrolyte salt is $LiPF_6$, chosen for its sufficient stability and unparalleled

conductivity. The rational behind these selections will be discussed in detail later (Section 2.4).

The cathode is casted on an Al current collector, as Al cheaper and lighter than Cu, and, equally importantly, is stabilized by the $LiPF_6$ electrolyte salt and does not experimentally oxidize at high potentials. The traditional cathode active material used in the majority of electronic devices is Lithium Cobalt Oxide (LCO), which offers a relatively high potential, high density, moderately high volumetric capacity and (particularly if doped) maintains its microstructure when 50-70% of its Li is removed [4]. Carbon black nanoparticles and larger exfoliate graphite particles are used to provide electrical conductivity, and polyvinylidene fluoride (PVDF) polymer is used to bind the particles together. The anode and cathode are kept electrically separated by a porous polypropylene and/or polyethylene separator.

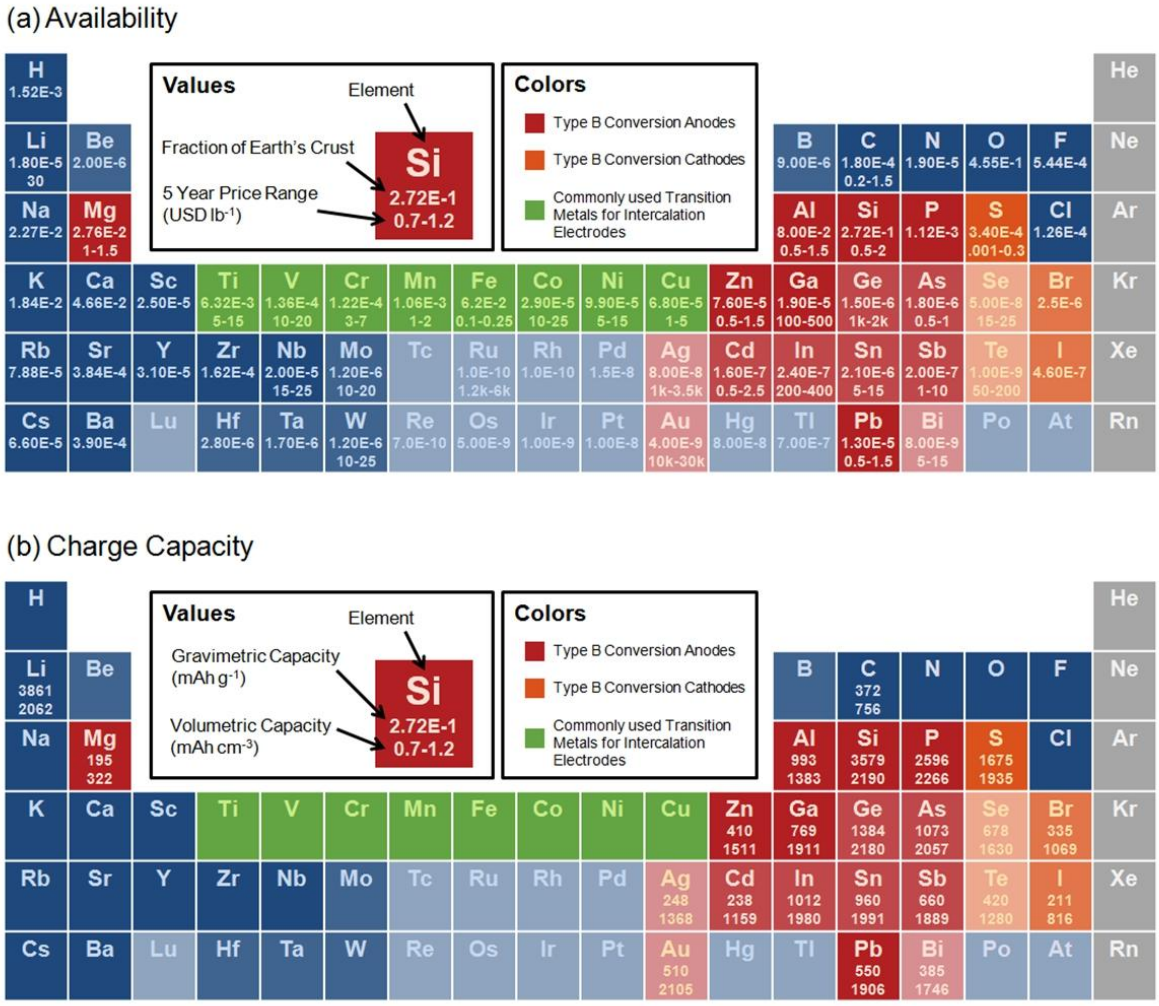

Figure 1. (a) Availability and (b) charge capacity of various alloying materials for Li-ion battery anodes. Gravimetric capacity is given as a fraction of unlithiated elemental mass, and volumetric capacity is given as a fraction of the final fully lithiated molar volume [4].

Developments in Li-ion battery technology has proceeded in all fronts, as researchers in academia and industry have modified, replaced, and improved every component mentioned above. In terms of material costs, cobalt used in the cathode has been the single largest source of raw material cost for Li-ion batteries. To reduce cobalt use, various new cathodes have been developed, such as NCA, NMC, LMO, and LFP, which use cheaper metals such as Mn and Ni (Figure 1).

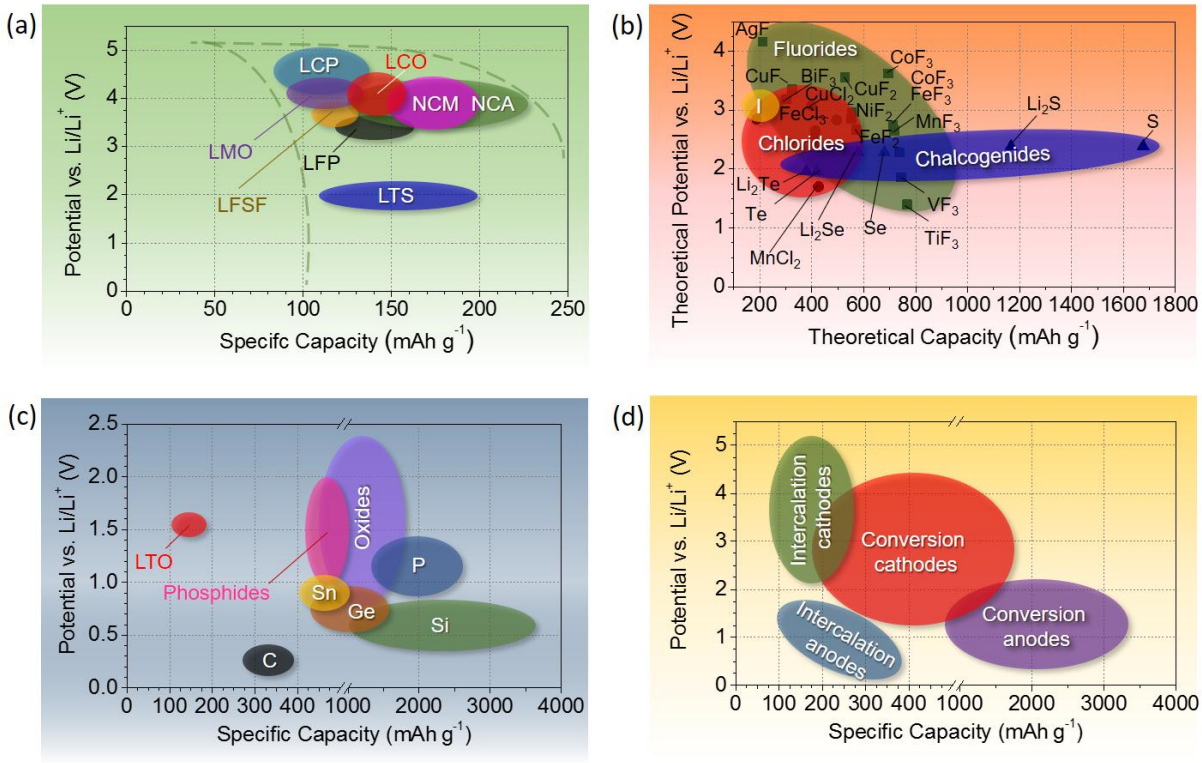

Figure 2. Potential vs. specific (i.e. gravimetric, or per mass) capacity of (a) intercalation cathodes, (b) conversion cathodes, (c) anodes, and (d) and overview comparing all three.

Researchers have also been developing conversion type electrodes, which do not maintain their original crystalline microstructure upon lithiation. Conversion electrodes can have much greater gravimetric energy density than the standard intercalation materials (Figure 2). However, conversion cathodes are generally non-metals which are electrical insulators and upon lithiation produce a salt which is often soluble in many organic electrolytes. Conversion anodes often undergo extreme volume change upon lithiation, which can cause the particles to pulverize and lose electrical contact. Repeated expansion and contraction can also destroy the passivating SEI layer, causing new SEI to be formed. As Li-ion batteries are constructed with a limited amount of Li available, starting in the cathode, much of the Li gets consumed in the formation of the SEI. This decreases the capacity of the overall battery. Furthermore, the large volume change can

create new surfaces to be exposed to the electrolyte and cause further SEI formation and thus irreversible Li loss. Consequentially, for conversion anodes, the SEI is often unstable and its constant growth eventually causes the battery to lose its charge capacity and thus depleting the Li inventory in the battery or increasing the ionic resistance of the SEI [5].

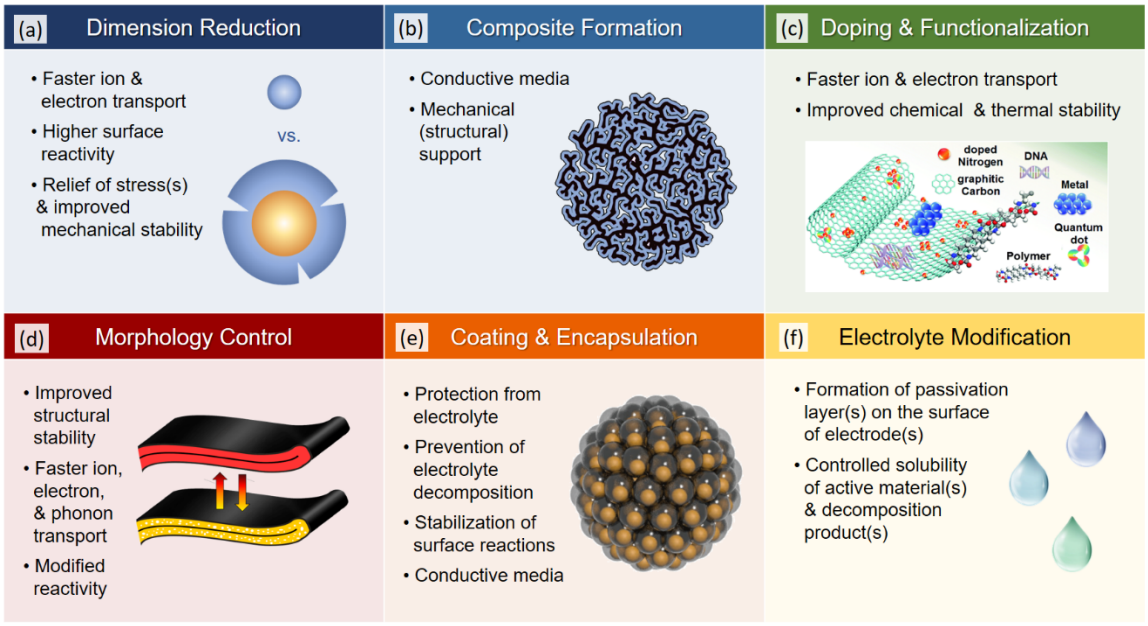

Figure 3. General strategies for electrode performance enhancement and their rationale: (a) reducing dimensions of active materials, (b) formation of composites, (c) doping and functionalization, (d) tuning particle morphology, (e) formation of coatings or shells around active materials, (f) modification of electrolyte.

Many strategies have been pursued to overcome these issues (Figure 3). For anodes, silicon have received the greatest attention and achieved the most promising results. Silicon is abundant, chemically stable, and easy to process due to the many methods and tools developed by the microelectronics industry. Silicon also has the highest theoretical specific capacity of any element other than Li, and also has one of the highest volumetric capacities. However, as with all alloying anodes, Si undergoes enormous volume change during charge/discharge cycling, causing extreme internal

stress and pulverizing the large electrode particles. Nanostructured Si containing electrodes using binders of higher hardness and small (nano-sized) Si particles were fabricated in recent years to allow the particles to withstand the stress. Smaller Si particles generate significantly smaller stresses within the particles during cycling and thus are much more mechanically stable (Figure 3a). Higher hardness / higher toughness binders that exhibit low swelling in electrolyte solvents can maintain electrical contact between the particles even when significant volume expansion occurs within individual particles (provided the electrode possess sufficient pores to accommodate Si expansion upon lithiation). However, nanostructures have disproportionately large specific surface area, meaning that a much larger volume of SEI forms and contributes to irreversible capacity losses.

2.2. Electrode Construction

Electrodes are composite materials constructed of the aforementioned active materials, carbon conductive additive, and polymer binder, and are constructed roll to roll by mixing these components in a solvent, casting the resulting slurry on metal foil followed by drying. This process typically involves a dissolution of a polymer binder in a solvent, dispersing the active particles and conductive carbon additives in the binder-containing slurry suspension, and fully drying the solvent from the mixture after casting. Unfortunately, the standard PVDF binder is not soluble in water, and many organic solvents present a flammability hazard due to their high vapor pressures. N-Methyl-2-pyrrolidone (NMP) is thus used as it dissolves PVDF effectively, has a low vapor pressure (i.e. low flammability), and has low surface energy with carbon (resulting in a

good dispersion). Water based slurries are also sometimes used with water soluble binders in order to reduce the cost of slurry casting.

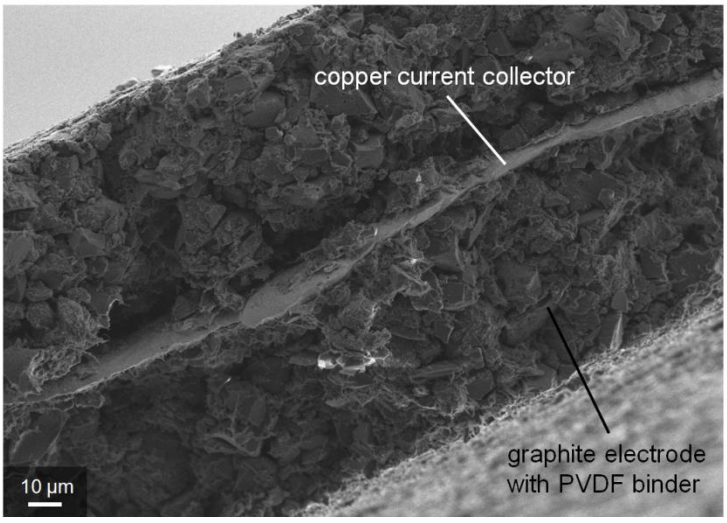

Figure 4. SEM cross-section of finished double-sided graphite anode with PVDF binder.

After a slurry has been casted, the electrodes are then dried and pressed. Electrodes must be dried thoroughly to remove any trace amounts of water, as this will react with $LiPF_6$ to produce HF in the battery cell [6]. The pressing (also known as calendaring) improves the adhesion in the electrode, improves volumetric capacity of electrodes, and increases the number of point contacts between the particles to improve electrical conductivity. However, excessive calendaring results in insufficient pore volume for Li transport by the electrolyte. Therefore, the calendaring pressure must be tuned to optimize a balance between electrical and ionic conductivity within the electrode.

2.3. Polymer Binder Adhesion and Mechanical Properties

A polymer binder is necessary in a battery electrode to keep the particles together with good electrical contacts. In order for this to be achieved, the binder must first have good adhesion to the particles and the current collector. Adhesion is a complex topic, but

in this context, there are two particular mechanisms of interest. The first is the electrostatic or Van der Waals intermolecular forces between the polymer and the solid surface. The second is the functional groups, which form chemical bonds with the solid surfaces. These forces together determine the strength of the interface between the two materials, although the truth is not always so simple. For example, although functional groups have been shown to improve adhesion, a high density of functional groups can also cause internal stress and weaken the adhesion [7].

For volume changing electrodes, the polymer binder should typically also exhibit good mechanical strength and hardness. This is not immediately apparent. In order to maintain good electrical contact for a volume changing material, an elastic and stretchable binder would intuitively appear to be better than a hard and brittle binder [8,9]. However, the opposite has been observed to be true [10-12]. Carboxymethylcellulose (CMC), polyacrylic acid (PAA), and alginate are all harder and more brittle than PVDF, but have been repeatedly shown to result in better performing conversion anodes than PVDF. This is in part due to the -OH groups which provide superior adhesion [13]. However, Komaba et al. found that PAA maintained a denser electrode where all the Si particles were electrochemically active, whereas PVDF allowed the electrode to expand and resulted in some electrochemically inactive Si particles [14]. Thus strength and hardness appear to be key properties in the performance of a binder.

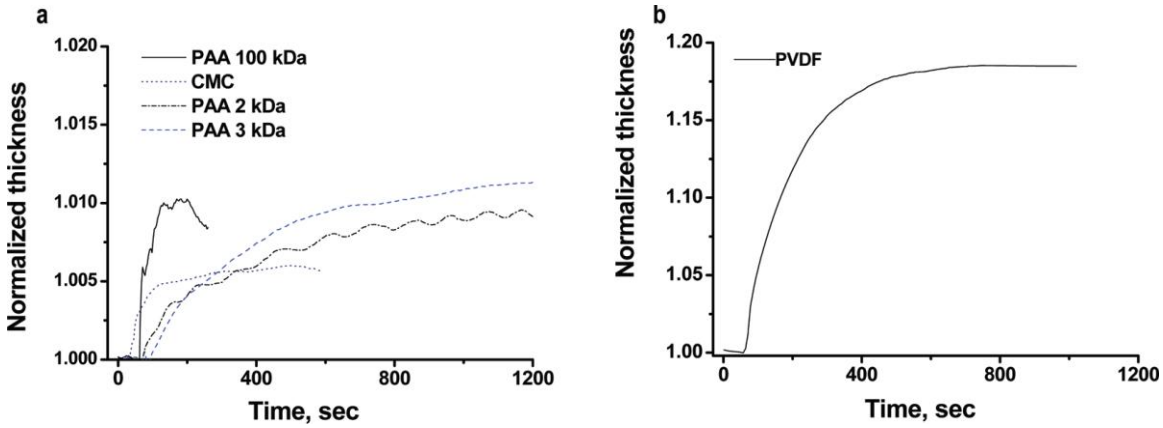

Figure 5. Swelling of (a) PAA with differentMw and Na-CMC, and (b) PVDF in diethylcarbonate vapor. The data were obtained by ellipsometric measurements and normalized to the thickness of an initial "dry" film [11].

However, choosing a binder based on its strength and hardness is slightly misguided, as these properties can change drastically with swelling in the battery electrolyte. Swelling is a phenomenon where a binder expands due to solvent intermixing. In most Li-ion batteries, binders are always in a direct contact with an organic electrolyte, which may or may not cause the binder to swell. A previous study from our group have shown that PVDF does indeed swell ~18% in DEC vapor, whereas CMC and PAA showed virtually no change ~1% (Figure 5) [11]. Figure 6 shows that PVDF also loses much of its stiffness when submerged in DEC according to AFM measurements, while CMC and PAA do not. Identical tests have shown alginate to also maintain its stiffness [15]. While these tests are not quantitative, they show that the mechanical properties of binders in the dry state can become largely irrelevant when swollen with electrolyte. Thus the choice of a good binder requires careful consideration of the electrolyte.

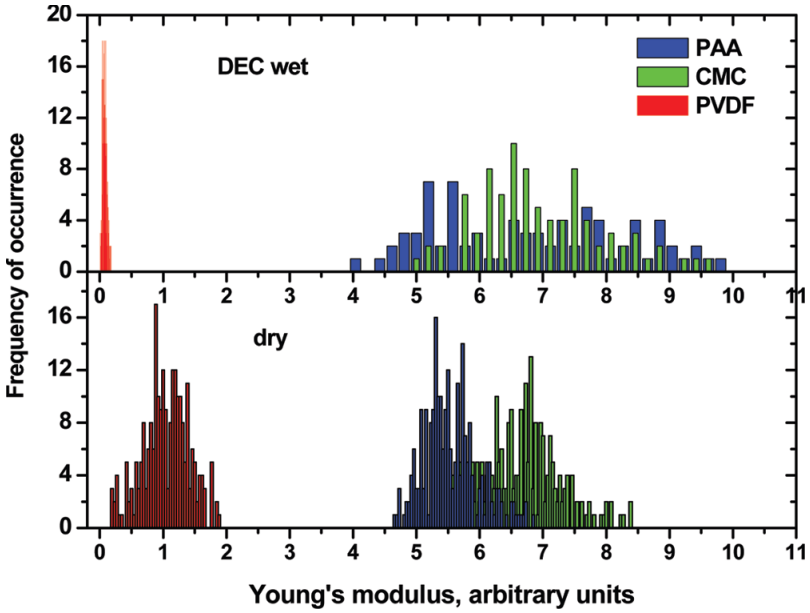

Figure 6. Results of AFM stiffness measurements for films made from PAA (100 000 g/mol), CMC, and PVDF. Results are normalized to stiffness of PVDF in dry state [11].

Swelling is in essence, a step before dissolution. The solvent diffuses into the polymer phase and is absorbed due to a thermodynamic driving force. Thermodynamic theories for solubility can therefore be used to help predict swelling. In fact, swelling tests have themselves been used to measure the solubility parameter of polymers, based on the theory that the solvent with the closest solubility parameter also has the greatest swelling. The solubility parameter (δ) is also known as the Hildebrand parameter or the cohesion parameter, and is determined by the heat of vaporization and the molar volume (V) of the solvent.

$$\delta = \left(\frac{\Delta H_{vap} - RT}{V}\right)^{1/2}$$

This equation originates from equation for the heat of mixing proposed by Hildebrand, Scott, and Scatchard that

$$\Delta H_m = V\left(\left(\frac{\Delta H_{vap,1}}{V_1}\right)^{1/2} - \left(\frac{\Delta H_{vap,2}}{V_2}\right)^{1/2}\right)^2 \varphi_1 \varphi_2$$

where V is the molar volume of the mixture and φ_i is the volume fraction of i [16-19].

Of course, a single parameter can never capture all of the complex intermolecular interactions between molecules. Indeed, the Hildebrand parameter is only useful for hydrocarbons governed only by dispersion forces. For organic solvents without strong intramolecular interactions, the Hansen parameters often provide more useful [20]. The Hansen parameters essentially split the total cohesion energy E into dispersive, polar, and hydrogen bonding components.

$$E = E_d + E_p + E_h$$

$$\delta^2 = \delta_d^2 + \delta_p^2 + \delta_h^2$$

Solvents with a similar set of solubility parameters should dissolve each other, while solvents with different solubility parameters should not dissolve each other. Calculating the contributions of each of these three components is often an extremely difficult task, however [20]. The polar component can simply be calculated from the dipole moment and molar volume. However, the dispersive and hydrogen bonding components must often be calculated by group contribution methods, which are less accurate. What is often done instead is to use a set of liquids for which the solubility parameters are known as a reference. The solubility of a new liquid is then evaluated for each known liquid, and the solubility parameters of the new liquid is thereby evaluated. In fact, Hansen developed his reference set of solubility parameters this way, while also utilizing the fact that combinations of solvents often act like their geometric mean. According to the developed theory, whether or not two solvents will dissolve depends on the 'distance' between the solubility parameters determined by

$$R_a^2 = 4(\delta_{d1} - \delta_{d2})^2 + \left(\delta_{p1} - \delta_{p2}\right)^2 + (\delta_{h1} - \delta_{h2})^2$$

A geometric sphere is then generated along the three axes within which other solvents are soluble in the liquid of interest. The radius of this sphere is R_0, and is different for each molecule. It was also discovered that molecules with smaller molar volume tend to be better solvents, dissolving other molecules even when R_a is large compared to larger molecules. Thus Hansen solubility parameters are reported along with the molar volume.

Table 1. Hansen solubility parameters (δ), molar volumes (V_m), solubility radius (R_0), and the relative energy difference (R_a/R_0) for each solvent with PVDF [20,21].

	δ_d ($MPa^{1/2}$)	δ_p ($MPa^{1/2}$)	δ_h ($MPa^{1/2}$)	V_m (cm^3/mol @ 25C)	R_0 ($MPa^{1/2}$)	$R_a/R_{0,PVDF}$
Acetone	15.5	10.4	7	74		1.1
DMSO	18.4	16.4	10.2	71.3		1.3
Ethanol	15.8	8.8	19.4	58.5		2.5
NMP	18	12.3	7.2	96.5		0.9
THF	16.8	5.7	8	81.7		1.7
Toluene	18	1.4	2	106.8		3.3
DEC	16.6	3.1	6.1	121		2.4
DMC	15.5	3.9	9.7	84.2		2.1
EC	19.4	21.7	5.1	66		2.9
PC	20	18	4.1	85		2.5
1,3-DIOX	18.1	6.6	9.3	69.9		1.5
1,2-DME	15.4	6.3	6	103.9		1.9
PVDF	17	12.1	10.2		4.1	

In general, it is clear that the Hansen solubility parameter is a simplification of a complex phenomena. However, returning to the issue of polymer binders, this theory provides a basis for predicting and understanding how the solvent molecules are likely to interact with the binder. Unfortunately, Hansen solubility parameters oversimplify hydrogen bonding, and does not capture other types of interactions such as induced

dipoles and electrostatic interactions. In fact, reported Hansen parameters generally lump all of these interactions not included by the other two parameters into the hydrogen bonding parameter. Thus this theory is not applicable to aqueous systems.

Nevertheless, Table 1 shows the solubility parameters of a variety of solvents for slurry casting and Li-ion battery electrolytes, and compares the relative energy difference (RED, or R_a/R_0) for these solvents for PVDF. $R_a/R_0 < 1$ should mean that PVDF is soluble in the solvent. This is the case only for NMP, as is expected, as PVDF is generally known to be insoluble to many standard laboratory solvents. Interestingly, while DEC was found to swell PVDF, the RED is very large at 2.4. Furthermore, Sigma-Aldrich lists ethylene carbonate as a solvent for PVDF [22], despite RED being 2.9. EC does have a small molar volume, but this is seems unusual. This discrepancy may have to do with the hydrogen bonding term which is inordinately large for PVDF. It should also be noted that the mixtures of linear carbonates (DEC, DMC) and cyclic carbonates (EC, PC) can produce RED < 1. This is mostly due to the polar term being opposite one another with respect to PVDF. PAA and CMC were not listed in the tables, most likely due to strong hydrogen bonding.

2.4. Electrolyte and SEI

As described earlier, the traditional Li-ion battery uses a combination of EC, DEC, and DMC electrolyte solvents with $LiPF_6$ salts. Table 2 shows the physical properties of many electrolyte solvents. Cyclic carbonates (EC and PC are listed) are particularly good organic electrolyte solvents, as these have high dielectric constants, and thus are good solvents for Li salts. EC is often used despite its high melting point, as it forms an

extremely stable SEI layer on the anode. DMC can also self-passivate its reaction with Li foil, although to a much lesser degree. Thus the combination of EC/DMC provides a well performing electrolyte which can operate at temperatures down to 15 ºC [23]. For commercial use, however, DEC was also added to enable low temperature operation. The EC/DEC combination can also be used, but suffers from higher irreversible capacity loss on the first cycle, and results in higher impedance [24].

Table 2. Relevant physical properties of common solvents for Li-ion batteries [25].

	Melting Point (ºC)	Boiling Point (ºC)	Dielectric Constant (@ 25 ºC)	Viscosity (cP @ 25 ºC)
EC	36.4	248	89.78	
PC	-48.8	242	64.92	2.53
DEC	-74.3	126	2.805	0.75
DMC [26]	4.6	91	3.107	0.585
EMC	-53	110	2.958	0.65
1,3-DIOX [27]	-95	76	7.13	0.59
Monoglyme	-58	84	7.2	0.46
Diglyme [28]	-64	162	7.23	
Triglyme[29,30]	-45	216	7.62	1.95

More modern electrolytes tend to use EMC rather than the DEC/DMC combination. The reasons for this is related to its somewhat superior electrochemical stability with graphite anodes combined with its low melting point. Ein-Eli et al. found that where graphite could not be lithiated in DEC and could only be lithiated to 120 mAh/g in DMC, lithiation proceeded to 345 mAh/g in EMC [31].

Conversely, the use of additives has expanded Li-ion electrolyte chemistry to a wide variety of solvents, which are generally unstable on the anode. Additives such as Vinylene Carbonate (VC), Fluoroethylene Carbonate (FEC), and Prop-1-ene-1,3-Sultone

(PES) can stabilize the SEI by decomposing on the anode first, thereby enabling previously untenable combinations such as PC solvent with a graphite anode [32]. PC solvent is normally incompatible with graphite anodes as it will intercalate into the graphite and make the graphite electrochemically inactive [33]. A stabilized SEI with PC solvent is advantageous because PC provides superior ionic conductivity in comparison to EC. However, no SEI is perfect, and the best cycle life is generally obtained by avoiding such unstable solvents.

$LiPF_6$ is used as the electrolyte salt because it results in high conductivity and passivation of Al current collector foils[34,35]. Lithium bis(trifluoromethane)sulfonimide (LiTFSI) also offers high conductivity, and thus tends to be used when $LiPF_6$ electrolyte is not suitable for the particular application and when the highest usable cathode potential is below ~ 4.0 V vs. Li/Li^+ to avoid Al corrosion. For example, at higher temperatures, $LiPF_6$ in carbonate electrolyte is a particularly unstable combination on the time scale of a battery (~ 1 year). $LiPF_6$ thermally decomposes to LiF and PF_5 very easily [36], even with small increases in temperature [37]. PF_5 can then be further reduced at the anode [23]. LiTFSI, conversely, is more stable to thermal decomposition [38], and does not cause additional thermal decomposition to the SEI. However, LiTFSI causes pitting corrosion on Al current collectors at above ~3.55V [39], and thus requires an alternative solvent [40] or passivating additive [41] for use at higher potentials. Preventing Al corrosion in $LiPF_6$-free electrolytes above ~ 4.0 V is typically very challenging and may become prohibitively expensive.

The SEI instability is often the major point of failure in a Li-ion battery. For example, battery capacity loss in a Li-ion battery is generally due to a loss of active

material or a loss in Li inventory [42]. Active material can be lost due to excessive SEI growth in a localized area, causing an increase in ionic impedance and thus making the active material ionically inaccessible [43]. SEI growth generally also consumes Li, as it occurs either electrochemically, or as a result of a chemical reaction between the active material and the electrolyte [44]. These effects are especially exacerbated at higher temperatures, as this is a diffusion driven process [45].

Physically, the SEI is a layer that is on the order of 10^0 - 10^2 nm thick [16,17]. The basic composition of the anode SEI includes Li_2CO_3 and organic semi-carbonates from the organic solvent and LiF, P_xF_y, and $P_xO_yF_z$ from the $LiPF_6$ salt [46-48]. SEI forming additives will obviously modify this composition, but these components are somewhat of a mystery, as each battery manufacturer protects their additive formulation closely. FEC and VC are two such anode SEI forming additives which have become quite popular, although FEC is preferred as VC will increase the viscosity of the electrolyte and is more expensive. Other additives that have been explored academically include phosphorus and sulfur based electrolyte additives and phosphorus and phosphorus and boron based electrolyte salt additives [49].

Native oxides can also be considered to form a component of the SEI. For example, Si anodes constructed in air will inevitably have a native oxide layer. This layer is the electrochemically lithiated when the battery is first charged, forming a Li-Si-O compound which is not easily reversible [47]. As most conversion anode materials are metallic or semimetallic, this is mechanism is applicable to many conversion anodes.

Chapter 3. Experimental Methods

3.1. Ball Milling

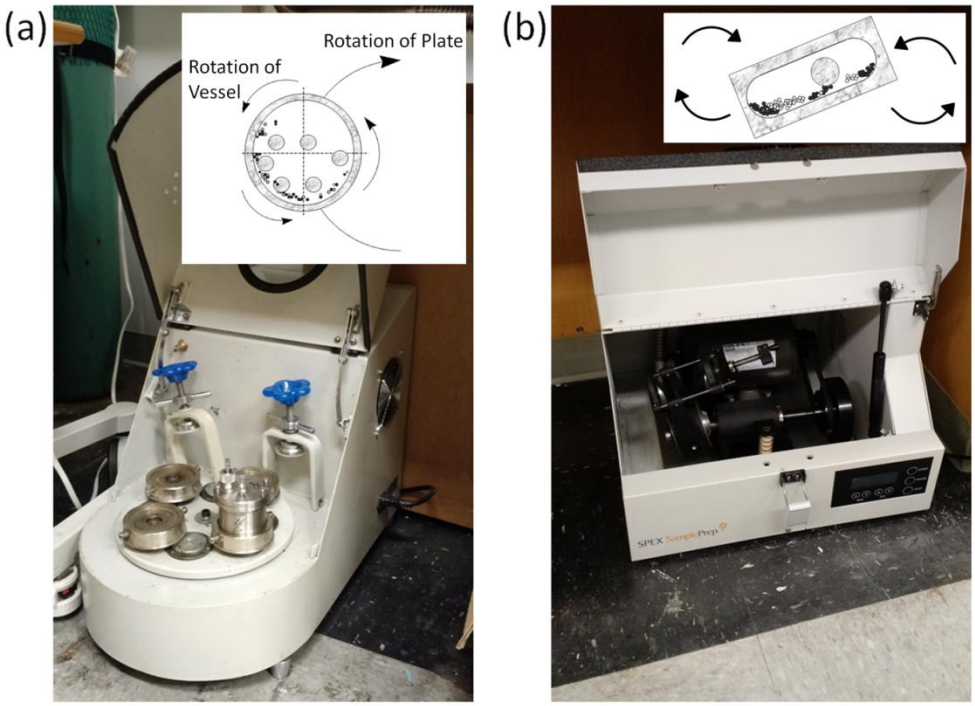

Figure 7. (a) Planetary and (b) shaker ball mills [50].

Ball milling is a process by which a powder material is put in a jar with ball milling balls (also called the grinding media) to crush the powder. Ball mills come in many forms [51], the smallest of which is the mixer or shaker mill, in which the jar is shaken in a figure eight. This type of mill produces high energy collisions, but can only process a small amount of material at once. Planetary mills rotate the jars around a central axis while spinning the jars themselves around their own axis. Planetary mills can mill slightly higher volumes, but cause lower impact collisions compared to shaker mills. Attritor mills have rotating impellers which agitate a bed of ball milling balls. Attritor mills are the largest volume laboratory scale mills, but also have the lowest energy

impact. Higher energy collisions reduces the time required to achieve the desired result, but also results in more contamination from the ball milling balls [51].

When designing a ball milling experiment, however, the rotation speed of the ball mill is generally set by the machine is not adjustable for lab scale devices. Instead, the impact of the collisions can be controlled by choosing a ball milling ball of a different size or material of a different density. Similarly, the ball/powder ratio also effects the energy of the impacts. With less powder in the jar, the energy of each impact is imparted on a smaller quantity of material, resulting in an effectively higher energy impact per quantity of powder. Finally, the fill rate determines the total amount of energy released in the jar by the impacts, controlling the overall temperature to which the jar will be heated.

Ball milling is generally performed on inorganic powder in order to reduce the size of the particles and/or mechanically cause phase transformations/chemical reactions. During ball milling, collisions of the ball milling balls create heat anisotropic compressive stress and shear stress, as well as heat from friction and strain. In terms of particle size, these impacts have been found to both decrease the crystallite size and cold weld particles of metals [52]. Eventually, after extended ball milling, particle fracturing and agglomeration reaches an equilibrium, and thus the particle size remains largely constant. For example, Si particles milled in a shaker mill decreased from ~150 micron to ~0.5 micron in about 3 hours, but did not significantly change after 38 hours of ball milling [53]. One study found the grain size of various oxides to decrease up to ~10^1 hours, but not produce any further change in the 10^2 hour time scale [54]. This suggests that individual grains cease the fracture after a certain particle size is reached, or that there is an equilbrium between grain growth and fracturing.

In terms of graphite, ball milling has been shown to eventually decrease the crystallite sizes to nm dimensions while also increasing the strain in the crystallites [55]. TEM observation of ball milled graphite has shown circular structures, suggesting that the graphite planes may even be fused together to form new sp^2 bonds [56]. Gas chromatography revealed a small amount of hydrogen release [57], suggesting that hydrogen at the edge planes were traded for sp^3 bonding with neighboring crystallites. Extended ball milling produces amorphous carbon [56], which agrees with Raman spectra showing an increased fraction of disordered carbon [57] and NEXAFS showing an increase in sp^3/sp^2 ratio [58].

Ball milling has also been reported to form phases which normally require extremely high temperatures and pressures. The cubic form of Y_2S_3, for example, normally requires 2000 °C and 7.7 GPa, but can also be formed in a mixer mill operating under ambient conditions [59]. Similarly, high pressure phases of cubic Dy_2S_3 [59], tetragonal $Cu_{2-x}S$ [60], Cubic $CuSe_2$ [60], and orthorhombic TiO_2 [61] have also been reported. However, not all high pressure phases could be formed by ball milling. For example, pyrite type $CuTe_2$ can be formed at 3.3 GPa, but not by ball milling [60]. This suggests that the impacts during ball milling result in a fundamentally different phase change mechanism compared to standard heating and pressing in a diamond anvil.

3.2. Indentation Measurement of Mechanical Properties

The theory for the indentation experiment using a power law fit can be found in a paper by Oliver and Pharr in 1992 [62]. Indentation is performed by bringing a probe of known geometry to the surface of a flat material. The probe is then pressed into and out

of the material with a set schedule, and the load (force) is measured against the displacement of the film by the tip. The schedule is generally set to linearly increase the load to a point, followed by an optional rest step where the load is kept constant, and finally reducing the load at a linear rate. Figure 8 shows a typical load vs. displacement curve for a material.

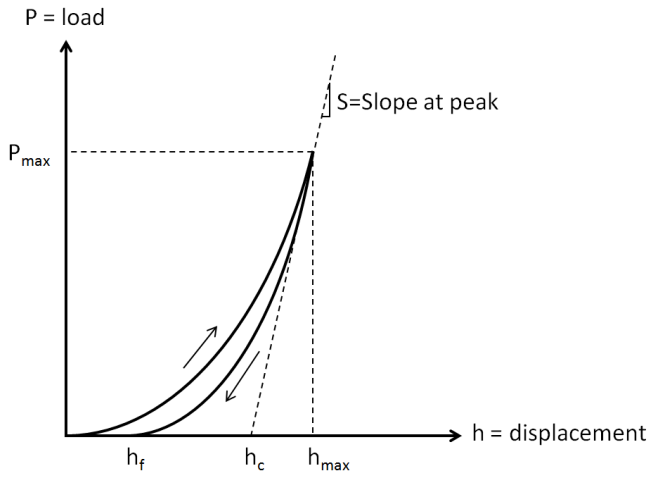

Figure 8. Schematic of the load versus displacement curve obtained from indentation experiments.

The hardness of the material can then be found based on the equation

$$H = P_{max}/A$$

where A is the contact area of the probe with the material, in this case, at the peak load. A depends on the geometry of the tip and the mechanical response of the material, and is defined by an area function relating A and h_c. The area function is found by taking multiple measurements on a material of known mechanical properties to different peak loads, keeping the load rate constant between measurements. For each measurement, A is found using the following equation

$$S = stiffness = \left[\frac{dP}{dh}\right]_{P_{max}} = 2E_r\sqrt{\frac{A}{\pi}}$$

where E_r is the reduced modulus. Unfortunately, creep can artificially increase the measured stiffness, and so the unloading curve is fit using a power law fit and extrapolated to P_{max}. The power law fit is defined by the following equation

$$P = B\left(h - h_f\right)^m$$

where B and m are the fitted parameters. Theoretically, m can be taken from Table 3.

Table 3. Parameter values for various geometries taken from Oliver and Pharr [62].

Probe tip geometry	ϵ	m
Flat	1	1
Paraboloid	0.75	1.5
Conical	0.72	2

h_c is found using the following equations

$$h_c = h_{max} - h_s$$

$$h_s = \epsilon(P_{max}/S)$$

The values for A and h_c are then plotted and a polynomial fit is found. This fit is called the area function. Conventionally, the area function takes the general form

$$A = \sum_{i=0}^{n} C_i h_c^{2^{1-i}}$$

Once the area function is known, then the Young's modulus of the material can be found from the reduced modulus using the equation for stiffness.

3.3. Scanning Electron Microscopy (SEM)

SEM is a method by which a focused beam of electrons is scanned across a sample, and the electrons emitted from the sample are collected in order to form an image. Unlike optical microscopy, the electron beam is focused, one spot at a time, and so the resolution is defined by the spot size [63]. Also, since imaging is performed with electrons, ultra-high vacuum is required to prevent scattering by atmospheric gas.

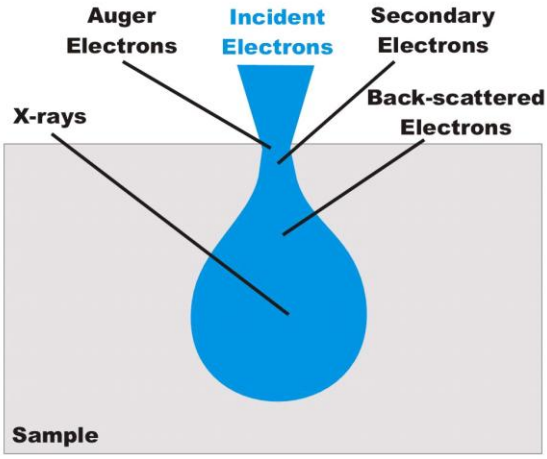

Figure 9. SEM sampling depth depending on analysis method [64].

Most SEM is performed by collecting the secondary electrons, which are electrons of > 50 eV [65]. These electrons are mostly electrons emitted from the sample as a result of inelastic scattering of incident electrons. Due to the low energy of secondary electrons, they can only escape from the very surface of the sample (Figure 9), resulting in a very high resolution. Low energy also means that the electrons can be attracted to the

detector regardless of their direction by using a potential bias. This reduces shadowing and produces high quality images with good depth of focus, but can also mask fine features on the surface of the sample if the incident electrons are too energetic. Also, highly energetic electrons tend to cause sample charging for less conductive samples. Thus, many newer models of SEM machines are made to operate with low potential electron beams, as low as 1 kV. Conversely, EDS (described later) analysis in SEM requires higher energy electrons in order to eject the core electrons, and so is operated at higher potential (5-20 kV). As the emitted x-rays are analyzed, the sampling depth is determined by the incident electron energy and the interactions with the sample. Thus the sampling depth is much larger (Figure 9), on the order of 10 μm.

3.4. Transmission Electron Microscopy (TEM)

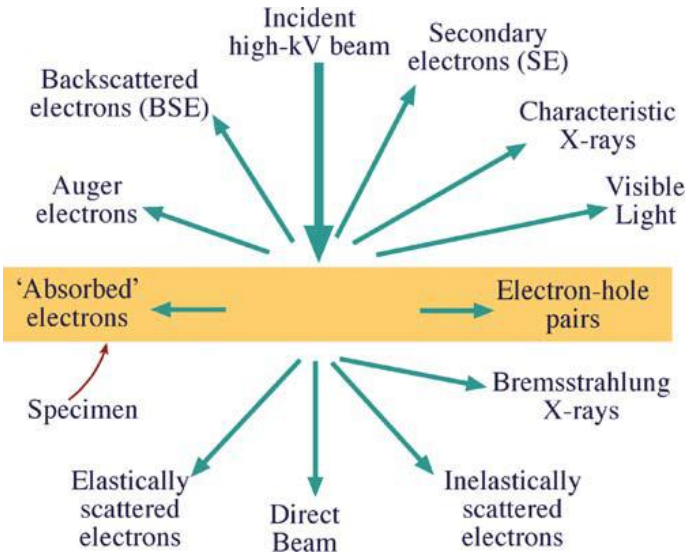

Figure 10. Interaction of high kV electron beam with thin sample in TEM [66].

TEM is an extremely powerful analysis method which allows x-y resolution down to the sub-Angstrom scale, allowing individual atoms to be visualized. Additional chemical analysis via EDS, electron diffraction, and Electron Energy Loss Spectroscopy

(EELS) make TEM an essential analysis method for modern materials science research. Just as with SEM, ultra-high vacuum is necessary. However, since electrons must pass through the sample, the sample must be thin and the electrons must be highly energetic. TEM is typically done at 100-300kV and samples are required to be no thicker than ~10^2 nm. Such high energy electrons will also damage many materials (e.g. polymers), further limiting the types of samples that can be analyzed. Also, chemical analysis via EELS requires a flat sample. Finally, it should be noted that although TEM can reveal an enormous amount of information about the microstructure of a material, the sampling is also extremely localized. Thus data from a TEM sample should not immediately be assumed to be representative of the rest of the sample.

3.5. Energy Dispersive X-ray Spectroscopy (EDS)

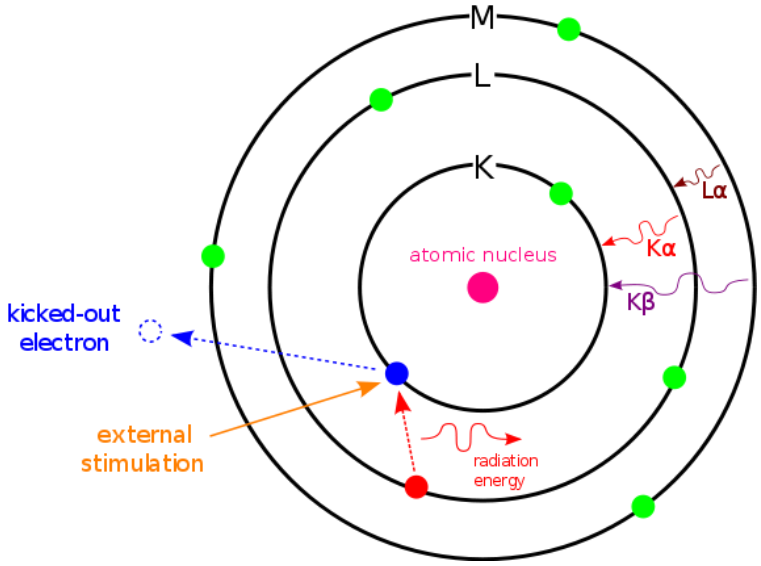

Figure 11. Mechanism of EDS x-ray radiation emission caused by external stimulation (incident electron) [67].

EDS is an extremely useful analysis method which allows the quick identification of atoms in an electron microscopy sample. The analysis can be done in an electron

microscope, and only takes minutes to perform. In both TEM or SEM, incident electrons will excite core electrons, which are emitted from the atom. The core energy level is then filled by an outer electron, and the energy loss is emitted as an x-ray photon (Figure 11). The energy level transition is limited by the selection rule to a difference in orbital angular momentum quantum number $\Delta l = \pm 1$. As the energies of these transitions are dependent on the atomic number, analysis of the x-rays allows one to identify elements and quantify their compositions. Theoretically, this means that any element down to Li can be detected with EDS. However, x-ray emission probability is higher for higher atomic number elements, and lower atomic number elements have a higher probability of Auger electron emission [68]. Thus low atomic number elements are difficult to detect. If a window film is used to protect the detector from high energy electrons, this makes low atomic number elements even more difficult to detect [69]. Majority of commercial EDS is typically limited to elements of $Z \geq 5$ (i.e. B and higher). However, the latest developments of windowless EDS systems (e.g., by Oxford Instruments, UK) showed an opportunity to detect Li and Be.

Quantification can be done by finding the ratio between peak intensity and composition, but these values are dependent on the specific experimental parameters. For example, the energy of the incident electrons can skew the calculated composition dramatically [70]. Thus calibration should be performed before the quantification using the same experimental conditions. The detection limit of EDS is ~1%.

3.6. Focused Ion Beam (FIB)

A dedicated FIB machine coupled with an SEM can be a very powerful analysis tool, providing 3D insight into nanomaterials. Imaging via SEM can be used to locate a specific area of the sample which can then be milled precisely to then 10^1 nm scale. The resulting cross-section can then be imaged again using SEM. FIB can even be used to prepare samples for TEM, although this process is extremely difficult and time consuming. Drawbacks of FIB include deposition of the ions used for milling on the sample and sample melting due to heating.

3.7. Time of Flight Secondary Ion Mass Spectrometry (ToF-SIMS)

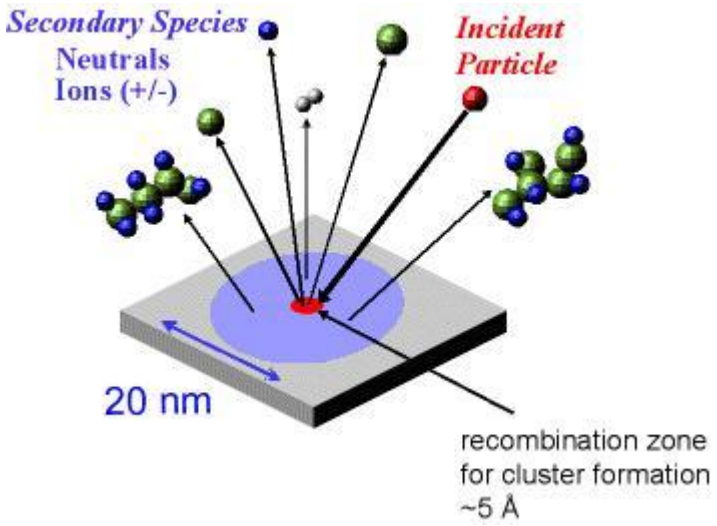

Figure 12. Fundamental mechansims of ToF-SIMS. The incident ion dislodges ions, as well as molecular compounds from locations further from the site of impact [71].

ToF-SIMS combined the power of ion beams to process nanomaterials with the analytical power of mass spectrometry. The beam can be focused to the nm scale, and the beam power can be reduced low enough to analyze mono-layers. Thus a 3D map can be constructed for various species detected in the mass spectrometer to the 10^0 nm scale, although z-resolution will be affected by surface mixing caused by the ion beam.

However, mass spectrometry analyzes the ion fragments ejected from the sample by the ion beam by analyzing the ratio between the ion mass and charge. This can only yield meaningful information when there is plenty of chemical information available. Ion milling also causes mixing of the material at the surface, can cause chemical reactions which may form new species, and mill different materials at different rates (see Appendix A).

3.8. Fourier Transform Infrared Spectroscopy (FTIR)

FTIR is a chemical analysis method in which infrared light is used to excite deformations in inter-atomic bonds. Specifically, the infrared radiation excites deformations which cause changes in the dipole moment of a group of bonded atoms. These deformations occur as a set of mutually exclusive normal modes of deformation depending on the symmetry of the bonds, each occurring at a specific energy. By measuring the wavelengths (and therefore the energy) at which the absorptions occur, functional groups and bonds can be identified. In general, wavelengths are reported in wavenumbers with greater wavenumbers to the left of the plot.

Data collection is performed either in transmission mode or in attenuated total reflection (ATR) mode. Transmission mode passes infrared radiation through the sample, thus requiring a sample that is mostly infrared transparent. The material of interest is generally ground down into a powder at a very low concentration with KBr, and pressed into a pellet. The absorption of a pure KBr pellet is then subtracted from the absorption of the sample pellet to find the FTIR spectrum of the material of interest.

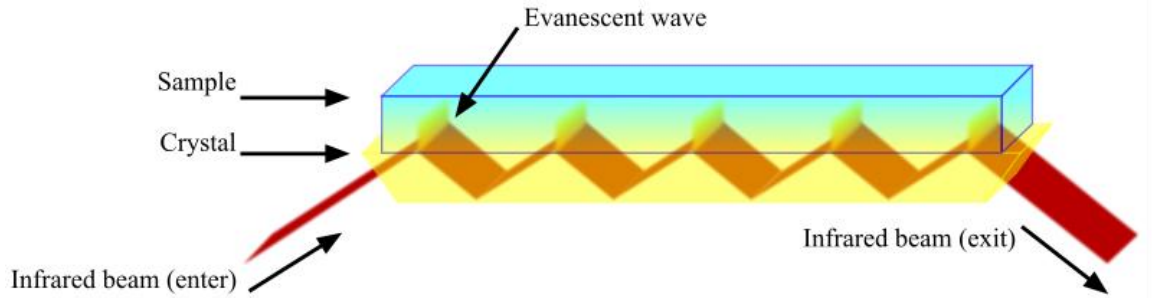

Figure 13. Sampling method for FTIR in ATR mode, using multiple total internal reflections to cause the infrared rays to interact with the sample multiple times through evanescent waves [72].

ATR mode has become very popular in recent years as it requires little or no sample preparation. In ATR mode, the sample is placed in intimate contact with a crystal, and the infrared radiation is applied at an angle so as to cause total internal reflection within the crystal. As the radiation is reflected, it produces an evanescent wave within the sample, and some of the energy becomes absorbed by the sample [73]. Sample exposure can be increased by reflecting the radiation back and forth within the crystal multiple times.

For internal reflection to occur, the angle of incidence (as measured against the normal to the interface) must be greater than the critical angle θ_c as defined by

$$\theta_c = \arcsin\left(n_2/n_1\right)$$

where n_2 is the refractive index of the sample and n_1 is the refractive index of the crystal. If the angle of incidence is smaller than the critical angle, then the resulting spectrum will include external reflectance from the sample. This is problematic, as the background is measured in air, in which case there is total internal reflection. Diamond is often used as the crystal due to its hardness (i.e. resistance to scratches) and chemical inertness. Other materials such as silicon and germanium have higher indexes of refraction, and therefore allow a smaller angle of incidence and a greater number of reflections.

The depth of the penetration of the evanescent waves is determined by d_p as defined by

$$d_p = \frac{\lambda}{2\pi(n_1^2 \sin^2\theta - n_2^2)^{1/2}}$$

where λ is the wavelength of the radiation. Typically, the depth of penetration is on the order of 1 micron.

3.9. X-Ray Diffraction (XRD)

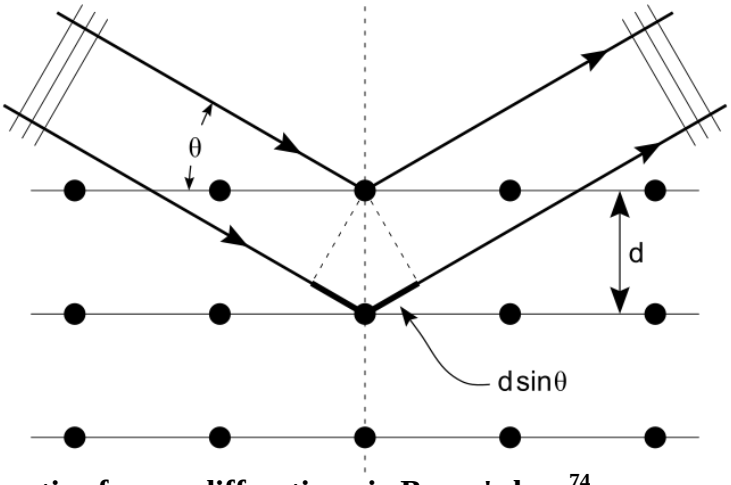

Figure 14. Schematic of x-ray diffraction via Bragg's law [74].

Being perhaps the most fundamental method of analysis in materials science, XRD utilizes the diffraction of parallel x-rays of a specific wavelength by planes of atoms in a crystal structure to impart microstructural information. Diffracted x-rays produce peaks in the spectrum, only when the path length causes constructive interference. (i.e. The electromagnetic oscillations of the x-rays overlap to magnify the oscillation amplitudes, rather than cancel each other out.) The phenomenon is described by Bragg's law:

$$n\lambda = 2d\sin(\theta)$$

where λ is the x-ray wavelength, d is the spacing between the crystal planes, θ is the angle of between the crystal plane and the x-rays, and n is a non-zero integer. The most popular method of XRD is powder diffraction, in which a powder of many crystallites of the material is laid flat on a sample holder, and the diffraction is performed in reflection mode. The spectrum is collected in a range of angles, and the result is plotted as intensity vs. 2θ. As with any x-ray method, Al K-alpha radiation is preferred as the source in laboratory scale equipment as it provides x-rays with the narrowest energy range [75].

3.10. X-Ray Photoelectron Spectroscopy (XPS)

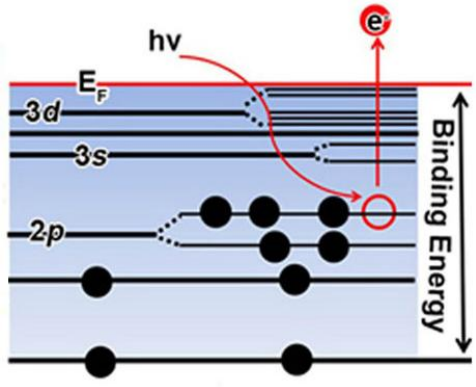

Figure 15. Mechanism of photoelectron emission [76].

XPS is an analytical method whereby an x-ray beam is used to excite core electrons out of the sample. The energy of the electrons released are then analyzed to determine the binding energy of the electrons to the core shells they originated from. By analyzing the binding energy, the element can be identified as well as some chemical information about the atom. Similar analyses can also be done by Auger Electron Spectroscopy (AES), which occurs when an outer shell electron loses energy to fill in the core shell. This process can be coupled with an electron of lower energy, which will then

be excited and released from the atom. Thus a general XPS spectra will usually also include Auger electron peaks.

In a sense, XPS is merely the opposite effect of EDS. However, the two methods differ in depth sensitivity. In EDS a high energy electron beam (5-30 kV) is used, meaning that the exposure depth is on the order of microns. In XPS, the emitted electrons only have several hundred eV energy, meaning that the inelastic mean free path of the electron is no more than several nm of material. XPS is therefore considered a surface sensitive technique. XPS also has a greater sensitivity, and has a detection limit of ~ 0.1%, and can reliably detect elements of atomic number 3 (Li) and greater (although with less sensitivity for very low atomic number elements).

The binding energy of the core shells changes, firstly due to electrostatic effects. Atoms with more protons have higher binding energy. Binding energy is also affected by the density of the electrons in the other energy states, as well as spin states. In particular, XPS is especially useful because small shifts in binding energy caused by changes in the valence levels can be detected.

However, binding energy is also effected by sample charging, when the number of electrons entering the sample does not equal the number of electrons escaping the sample. This tends to occur with less conductive samples, and to compensate, a flood gun is normally used to bombard the sample with electrons. However, charge compensation via flood gun is never perfect, and thus the sample must be calibrated using a peak for which the position is known. Charge shifts in binding energy can especially become problematic when different materials within the sample exposure area have different conductivities, and end up having what is called differential charge shifting. In this case,

detailed analysis becomes necessary to attempt to differentiate the peaks of each material. In general differential charging is not observed, and the C1s peak is used to identify the charge shift, as every sample inevitably has "adventitious carbon" which has deposited on the sample from the atmosphere. This practice has caused some protest as the peak position is not always reliable [77], but has become standard practice due to convenience.

A note should also be made about peak fitting, peak shape, and background. In XPS, the background level is changes at binding energies higher than an XPS peak, and this phenomenon has been empirically modeled as inelastic scattering by outer shell electrons by D.A. Shirley in 1972 [78]. Shirley assumes a constant scattering function however, and more physically meaningful backgrounds have been developed since, namely by the Tougaard background [79]. In practice, a combination of a linear and Shirley background is generally seen to be sufficient for most applications [80]. The peak shapes are defined by a variety of peak broadening mechanisms are believed to be Gaussian or Lorentzian in nature. For example, lifetime broadening due to the uncertainty of the energy of the end state after the photoemission causes Lorentzian broadening while thermal Doppler effects cause Gaussian broadening [75]. In laboratory scale XPS machines, however, the broadening tends to be dominated by the electron energy analyzer which causes Gaussian peak broadening. The energy analyzer reduces the energy of the incoming electrons to a constant energy (known as constant analyzer energy), known as the pass energy. The higher the pass energy, the stronger the signal to noise ratio and the wider the peak width. Thus a balance must be struck between signal and binding energy resolution. In any case, XPS peaks are often simply modeled as Gaussian peaks, and the

peak broadening from the analyzer is constant for all energies. Thus XPS peaks generally all have the same peak width.

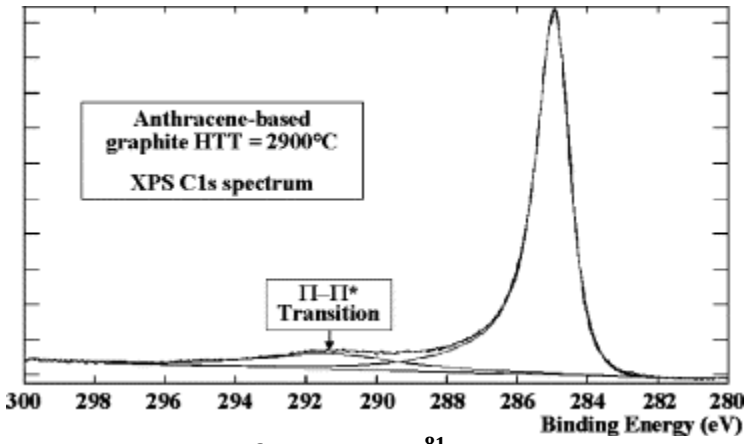

Figure 16. Asymmetric C1s peak for graphite [81].

The Gaussian function often fails to capture the peak shape for metals however, due excitations in the conduction band around the Fermi level. These can occur due to interactions with the core hole or due to the photoelectron being scattered on its way out [82]. The result is a distinctly asymmetric peak shape. The resulting peak shape can be modelled using a Doniach-Sunjic line shape [83], although this lineshape has an infinite integral. A similar lineshape can be achieved with a finite integral using the function derived by Mahan [84].

Finally, XPS analysis can be coupled with an ion beam to perform depth profiling on the 10^0 - 10^3 nm range. The lower limit is due to the XPS detection depth, and the upper limit is due to the practical etch rate and experiment length. Most often this is performed with an Ar^+ ion beam to prevent the ions from reacting themselves. However, the high energy ion beam generally causes even Ar^+ ions to become implanted in the sample, mixes material from the top of the sample with material underneath it, and can cause other chemical reactions to occur. Etch rates can also differ between materials by multiple orders of magnitude (see Appendix A), and is affected by shadowing for uneven

surfaces. Thus depth profiling via ion etching is generally unreliable beyond basic information on elemental composition. More reliable depth profiling can be done on the nm scale using Angle Resolved XPS (for flat samples), and on the 10^0 - 10^2 nm scale with a synchrotron x-ray source by varying the energy of the incident x-rays, thus providing the escaping electrons with different amounts of kinetic energy.

Chapter 4. Introduction to XPS Analysis of Li-ion Materials

XPS analysis has become an integral part of analyzing SEI layers due to its surface sensitivity and rich chemical information. However, interpretation of SEI XPS data can often be problematic due to the multitude of overlapping peaks. Furthermore, the exact binding energies (BE) of chemicals from literature are often uncertain to the range of ± 0.5-1 eV. The shift in BE caused by chemical bonds is often of the same magnitude. Reference samples are often necessary, and analysis generally focuses on relative differences in peak BE rather than absolute values.

Table 4 and Table 5 show the various peak positions of lithium salts, SEI components, and binder materials. The variety in peak positions reported is due to different charge references of varying reliability, as well as the asymmetry of some of the peaks. The Au reference is perhaps the most reliable, as it provides a relatively sharp peak without an oxide layer. Meanwhile, 'elemental carbon' is vague, as sp^2 and sp^3 hybridized carbon have slightly different BE [85]. Also, the differences in the BE for the CH_2 peak in PVDF can be explained by the asymmetry of the graphitic carbon peak used as a charge reference. Peak fitting is generally performed using symmetric Gaussian peaks. Therefore, some literature may report skewed results in the C1s spectrum due to overlap with the asymmetric tail of the graphitic peak, depending on the relative quantity of graphitic carbon present. Hydrocarbon (i.e. adventitious carbon) contamination, sp^3 hybridized elemental carbon, and functionalization of the carbon can be further causes of error.

Experimentally, the SEI is sensitive to air, and any air exposure can result in artifacts in the analysis [86]. Convenient vacuum sealed sample transfer chambers have become available in recent years due to widespread use of XPS for SEI analysis, and should be utilized whenever available. It is standard practice in many laboratories to wash the electrode in a volatile electrolyte solvent (e.g. DMC, DEC, or EMC). This can help remove low volatility solvents to prepare the sample for UHV, as well as remove any precipitated Li salts.

Table 4. XPS Binding Energies (BE) of various Li salts and SEI components.

Material	Li_{1s}	$P_{2p3/2}$	$S_{2p3/2}$	C_{1s}	N_{1s}	O_{1s}	F_{1s}	Charge Reference
$LiPF_6$		137.8					688	Cu standard? [87]
		138					687.7	Graphite 284.5 / Hydrocarbon 285 eV [88]
	58.2	138.2					687.9	Hydrocarbon 285 eV [89]
LiTFSI			170.2	294		533.9	689.9	Cu standard? [87]
	56.6		169.4	293	399.6	533	688.6	Hydrocarbon 285 eV [89]
	56.6		169.7	293.5	400.3	533.5	688.8	LiF 685.2 eV [90]
LiFSI	56.5		170.2		399.9	533.1	687.9	Carbon Tape 284.9 eV, LiF 685.2 eV [90]
Li_2CO_3				290-291		531.5		Cu standard? [87]
	55.1			289.6		531.4		$Au_{4f7/2}$ 84 eV [91]
R-CO_3Li				289				Elemental Carbon 284.86 eV [92]
LiF	56.7						685.9	Graphite 284.3 eV [93]
							686	Cu standard? [87]
	56.1						685.1	Hydrocarbon 285 eV [94]
	56						685	Hydrocarbon 285 eV [89]

Table 5. XPS Binding Energies (BE) of two binder materials.

Material: Polyacrylic Acid (PAA)

Peak	C_{1s} C-C	C_{1s} C-CO_2	C_{1s} C-O2	O_{1s} C=O	O_{1s} COH	Charge Reference
BE (eV)	285	286	289.5	532.7	534.1	C1s C-C Peak of PAA [95]

Material: Polyvinylidene Fluoride (PVDF)

Peak	C_{1s} C-H_2	C_{1s} C-F_2	F1s C-F	Charge Reference
BE (eV)	286.4	290.9		Carbon Black 284.5 eV [96]
	285.8	290.9	687.8	Graphite 284.5 eV [97]

Chapter 5. Comparing XPS, ToF-SIMS, and FIB/SEM for SEI Analysis

5.1. Introduction

Battery materials scientists have long been interested in measuring the thickness of the SEI layer Li-ion battery anodes. Continued growth of the SEI layer is believed to be a major cause of Li-ion batteries losing reversible capacity. However, the SEI is an *in situ* formed composite layer which stabilizes the interface between a lithiated anode (with reductive potential close to that of Li, the element with the lowest potential), and the electrolyte. Furthermore, the layer must transport Li^+ ions freely without causing too much internal resistance. Thus it comes as no surprise that the SEI layer is a highly reactive and extremely thin composite layer which is exceedingly difficult to study.

Ion milling has recently become a widely used method for depth profiling nano-layers of materials, although with the drawbacks discussed earlier in Chapter 3. An attempt was made to utilize ion milling techniques in characterizing the SEI layer. Three analysis methods were compared: Ga FIB milling combined with SEM imaging, ToF-SIMS depth profiling with a O_2 ion beam, and XPS depth profiling with an Ar beam. FIB is the only method by which an absolute value of the SEI layer thickness can be discerned. However, its results are highly localized, and it is unknown how beam damage will change the material being analyzed. ToF-SIMS is a very fast depth profiling method and yields an enormous amount of data. However, parsing the meaning of the wide variety of ions with only m/z to differentiate between them is impossible without complementary data from other sources. XPS is the slowest analysis method, but provides the most detailed chemical information. This section combines and compares the three analysis

methods, to provide a better understanding of the SEI and compare how each method contributes to the analysis of the SEI layer.

5.2. Experimental Methods

This study was conducted on anodes taken from three commercial pouch cells of the same design with a graphite anode and $LiMn_{1/3}Ni_{1/3}Co_{1/3}O_2$ cathode. Some of these cells were cycled extensively, and the degree of degradation was provided by the testing facility. The cells were ranked by level of retained capacity. Cell L (least degradation) experienced only the formation process to form a protective SEI film on the surface of the graphite electrode. Cell I (intermediate degradation) was stored 14 days at 10% of state of charge (SOC) at 25°C and then cycled 700 times between 50-100% of SOC at 45°C. Cell H (highest degradation) had 495 cycles between 0-50% of SOC at 45°C and had additional 1317 cycles between 50-100% of SOC at 45°C. All cells were discharged to 2.7 V prior to analysis to eliminate variations in the SEI due to SOC.[98]

Table 6. Cell degradation information.

Name	Degradation status	Capacity [mAh]	Capacity Retention [%]	Energy of discharge [mWh]	Energy of discharge retention [%]
Cell L	Lowest degradation (cell after formation)	767.7	100.00%	2798	100.00%
Cell I	Intermediate degradation	710.2	92.51%	2580	92.18%
Cell H	Highest degradation	669.9	87.53%	2428	87.12%

In order to determine the composition of the electrolyte, liquid NMR spectroscopy studies were conducted. The electrolyte, separated from the pouch cell by using a

centrifuge (5000 rpm), was mixed with 0.5 cm^3 deuterated acetonitrile in a glove box and transferred into a Teflon liner in a 5 mm screw-cap NMR tube (Wilmad). ^{1}H NMR, ^{19}F NMR, and ^{31}P NMR spectra were obtained on a Bruker AVANCE III spectrometer at 400 MHz, 376 MHz, and 161 MHz respectively. The proton spectrum was calibrated to the residual proton peaks from acetonitrile (CD_3CN); however, ^{19}F NMR and ^{31}P NMR were not calibrated exactly (± 1 ppm). The quantitative ^{1}H NMR spectrum was recorded on a Varian Mercury 400 MHz spectrometer with an acquisition time of 2.65 s.

The cells were opened in a glove box (<1ppm H_2O) to remove the anode, and kept under Ar atmosphere until analysis, minimizing exposure to air. The anodes could be easily separated with tweezers and they were not washed or submerged with an organic solvent such as dimethyl carbonate (DMC) to avoid the dissolution of lithium salts within the SEI.[99] Geometric variations in the electrodes were also avoided by collecting samples far from the current collector's connection to external circuitry.[100] TOF-SIMS was performed using an Ion-TOF-SIMS5-300 configured with a 25 keV Bi^+ primary liquid metal ion gun at a current density of 1.25 nA/cm^2 in positive ion collection mode with a 250 x 250 μm analysis area. Charge compensation was not used to avoid damage to the delicate SEI layers before data acquisition and the pressure was maintained below $5 \cdot 10^{-8}$ Torr. The mass calibration was performed with reference to H^+, Li^+, C^+, Na^+, Mn^+, and Cu^+ peaks, and all mass spectra were collected from 1-800 amu/z using a reflectron TOF type mass analyzer. Surface maps were performed using a 40 s acquisition time over a 250 x 250 μm analysis area. Depth profiles were performed using 2kV O_2 sputtering with a 500 x 500 μm raster area at a current density of 21.8 mA/cm^2, which resulted in a 0.78 nm/s etch rate for 100 nm SiO_2 on Si wafer.

XPS analysis was done using the Thermo K-Alpha (Al K_α peak), and an Ar^+ ion beam etch at 1 kV was used to qualitatively analyze the depth profile of the SEI's elemental composition and chemical states. The elliptical analysis spot size was set to 0.25 mm^2, giving a similar analysis area as the TOF-SIMS. Sample preparation was also done in the same way for TOF-SIMS and XPS analyses. The samples were transferred from a glove box atmosphere with < 1ppm water to the analysis chamber in a sealed vial, reducing air exposure to < 1 min. Analysis was performed on Avantage software using mixed linear-Shirley "smart" backgrounds and Gaussian peaks with FWHM within ±0.2 eV of the main peak.

FIB milling was carried out using a Nova 200 NanoLab (FEI COMPANY). A Ga^+ liquid metal ion source accelerated at 30 kV and 5 nA was used to mill a sample of 10 x 10 x 7(w x d x h) μm^3 volume. At least three different regions from the same sample were milled and the cross-section of the samples observed. As mentioned earlier, the main problems in using FIB are Ga contamination and heat generation. Ga contamination is primarily observed on the surface, and heat generation is minimized if the material is conductive. [101] To avoid these problems, the surface of the electrode was coated via Hummer V (Anatech) with gold for prompt heat dissipation, and uncontaminated inner carbon particles were observed. Gold sputtering was done at ~155 mTorr and 25 mA for 45 seconds. Air exposure was minimized to < 5 min by using a sealed pouch bag for material transfer.

5.3. Results and Discussion

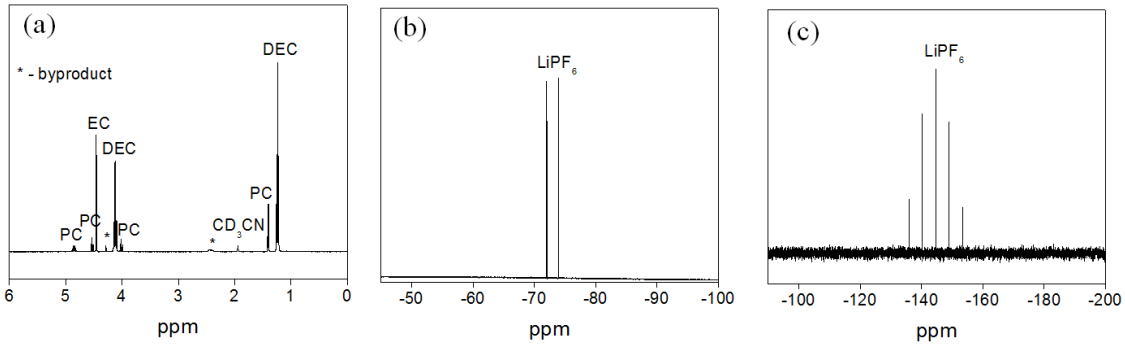

Figure 17. (a) ^{1}H NMR, (b) ^{19}F NMR, and (c) ^{31}P NMR spectra of the electrolyte obtained from Cell H.

The liquid electrolyte was investigated by NMR spectroscopy to identify the organic solvents and the salt utilized by the cells. Figure 17a shows ^{1}H NMR spectrum of the electrolyte and the peaks correspond to ethylene carbonate (EC), propylene carbonate (PC), and diethyl carbonate (DEC) based on the reference studies. [102,103] Two peaks labeled as * are unknown, and they may be byproducts of the electrolyte decomposition. Due to the complex nature of NMR spectral data, decomposed products could not be identified. We also could not observe any common electrolyte additives, such as vinylene carbonate (VC), fluoroethylene carbonate (FEC), or lithium bis(oxalate)borate, some of which we expected to be present in the cells. Either the electrolyte did not contain these additives, or they were decomposed during the formation cycles beyond the detection limit. To determine a relative ratio of organic solvents, quantitative ^{1}H NMR was carried out, and integrated peak areas were divided by number of protons to obtain molar ratio of EC:PC:DEC. This molar ratio was multiplied with molar mass and divided by density to determine volume ratio, which was roughly EC:PC:DEC 1:1:3. Figure 17b,c show ^{19}F NMR, and ^{31}P NMR spectra of electrolyte, and both of them showed fluorine-phosphorus coupling, which indicates that the electrolyte contains a $LiPF_6$ salt. Furthermore, peak

positions in ^{19}F NMR, and ^{31}P NMR spectra are closely matched with a previous study.[104] Molar concentration of the salt could not be determined in the electrolyte due to the small volume obtained from centrifuge and prompt evaporation during handling. However, the concentration of the salt is expected to be close to 1 M $LiPF_6$.

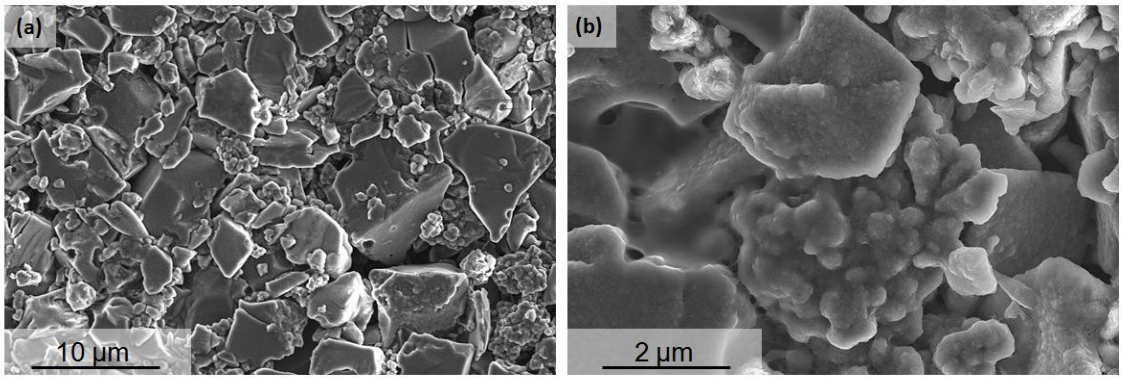

Figure 18. SEM micrographs of the top of the anode surface taken from (a) Cell L and (b) Cell H at different magnification. Particle size distribution and the SEI/binder coating is visible.

SEM studies showed relatively broad distribution of the graphite particles in the anode, from 1 to 20 µm (Figure 18). The samples additionally contained agglomerations of spherical sub-µm particles, likely carbon black additives, commonly added for porosity control and thus improved ionic transport through the anode and for improved mechanical properties. The top view of all the electrodes (from cells L, I and H) showed similar particles size distributions (Figure 18a) and the presence of a coating around the particles (Figure 18b). This coating is comprised of PVDF binder, SEI, and possibly lithium oxides, formed in the course of unintentional oxidation during sample transfer of Li left in the anode after discharge. It is not feasible to identify variations in the coating thickness with SEM.

Dynamic SIMS studies were performed to elucidate the composition of the SEI as a function of depth and further to estimate the SEI thickness and its correlation with the

observed capacity fade. Since the electrode consists of individual particles with pores between them (Figure 18) and not of a flat thin film, the ion beam etching/sputtering of the top of the electrode layer does not remove the electrode material uniformly. This causes the SIMS profiles to exhibit broad elemental distributions without sharp interfaces visible, as some of the SEI and PVDF on the side surface of the graphitic particles will always be visible even when graphite sputtering progresses significantly.

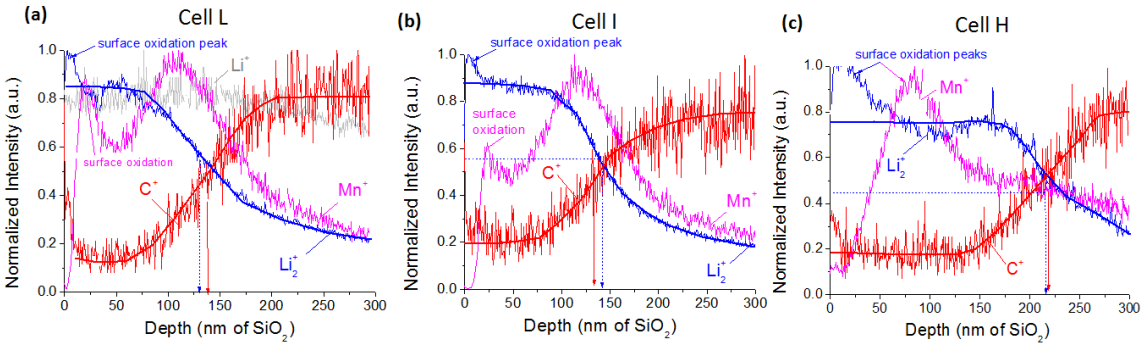

Figure 19. 375 nm ToF-SIMS depth profile showing a distribution of the selected SEI and active material species in anodes of: (a) Cell L, (b) Cell I, and (c) Cell H through the depth of the SEI as well as into the underlying graphitic structure. The depth was calibrated by oxygen ion etching of SiO_2.

At this point it might be appropriate to clarify that our prior studies indicate that PVDF swells in typical electrolyte solvents [105,106]. This swelling suggests that electrolyte solvents permeate through the PVDF and form an SEI upon their electrochemical reduction (decomposition) at both the carbon/binder interface and more importantly within the swollen PVDF layer. Unfortunately, however, negatively charged ions (such as F^- ions) are very difficult to image in a SIMS depth profile due to their low TOF-SIMS sensitivity and detection limits when oxygen ions are used for sputtering and in positive ion collection mode. In addition, F is present in both the SEI and PVDF. As a result, we could not visualize the expected correlation between the depth profiles of PVDF and SEI coatings.

The S-curve-shaped depth profile of C^+ allows us to monitor the initiation of the graphite sputtering. The increase and subsequent saturation in the concentration of the sputtered C likely correspond to the PVDF/SEI layer being slowly removed from the majority of the surface particles, exposing pure graphite to the ion beam. If this hypothesis is correct, the average PVDF/SEI layer thickness of the imaged portion of the anode increases from ~140 nm (for L cell anode) to ~220 nm (for H cell anode) (Figure 5).

From both static and dynamic analysis the main component of the SEI is the LiF from the Li_2^+ peak followed closely by the $(C_2H_2)_nLi^+$ series of peaks. Other literature results suggest that the $(C_2H_2)_nLi^+$ species are formed from the decomposition of vinylene carbonate into lithiated polyacetylene.[107] In either case, the Li_2^+ depth profile must correlate to the SEI distribution within the anode surface. Significant decrease in Li_2^+ likely corresponds to the removal of the majority of the SEI from the graphite surface. The sharp increase in the Li_2^+ concentration at the surface is believed to be related to the formation of lithium oxide species due to unintentional anode oxidation occurring during transfer to the analysis chamber. The larger value for this peak in the anode of H-cell (Figure 19c) may be related to the unintentionally stronger sample oxidation. The broader Li_2^+ peak that propagates deeper into the sample likely follows the SEI distribution. The depth, which corresponds to Li_2^+ concentration decreasing half way from the maximum to minimum level, is roughly equal to the depth at which the C^+ concentration increases half way from the minimum level at the surface to the maximum level in the bulk, supporting our hypothesis. Interestingly, the Li^+ depth profile (shown in cell L only,

Figure 5a) is very flat and does not have any features that could be correlated with the SEI.

A strong signal from Mn^+ was present on the surface of all the samples, suggesting Mn dissolution from NMC cathode (Figure 19) and diffusion to the anode, as previously described [108]. Similar to Li_2^+, the Mn^+ distribution within the PVDF/SEI layer exhibits a bi-modal profile. However, the Mn^+ peaks are shifted to the bulk, presumably due to the lower mobility of the Mn ions (or atoms). In addition, the surface Mn^+ peaks are less pronounced compared to the surface Li_2^+ peaks (Figure 19a,b), with the exception of the anode from Cell H (Figure 19c), which exhibits a surface peak larger than the bulk one. This sample also contains a very strong surface Li^{2+} peak (Figure 19c). Notably, the Mn^+ peaks (both the surface and the bulk) initiate at a depth at which the corresponding Li_2^+ peaks start fading. This juxtaposition means that Li, in average, is located closer to the top surface than Mn, as might be expected from higher Li mobility and higher Gibbs free energy driving force for Li to move to the surface and oxidize.

In addition to the diffusion of some of the Li and Mn ions towards the surface after the cell disassembling and brief exposure of the anode to the oxidizing media (air), two alternative (but less likely in the view of the authors) explanations could be offered to justify the bi-modal distribution of Li_2^+ and Mn^+. First, Li and Mn ions may exhibit different mobilities (diffusion coefficients) in different layers inside the SEI. Second, the two types of carbon present in our samples – graphite and agglomerated carbon additives (Figure 18) may potentially exhibit a difference in the average SEI and PVDF thicknesses. The later may indeed contain the SEI and a binder deep inside the agglomerates and thus correspond to the "bulk" or 2nd peak. However, we find it unlikely

that Mn and Li concentrations within the SEI increase with cycling disproportionally higher on graphite versus on agglomerated carbon additives (the surface peaks become more pronounced in Cell H versus cell L, compare Figure 19a and Figure 19c).

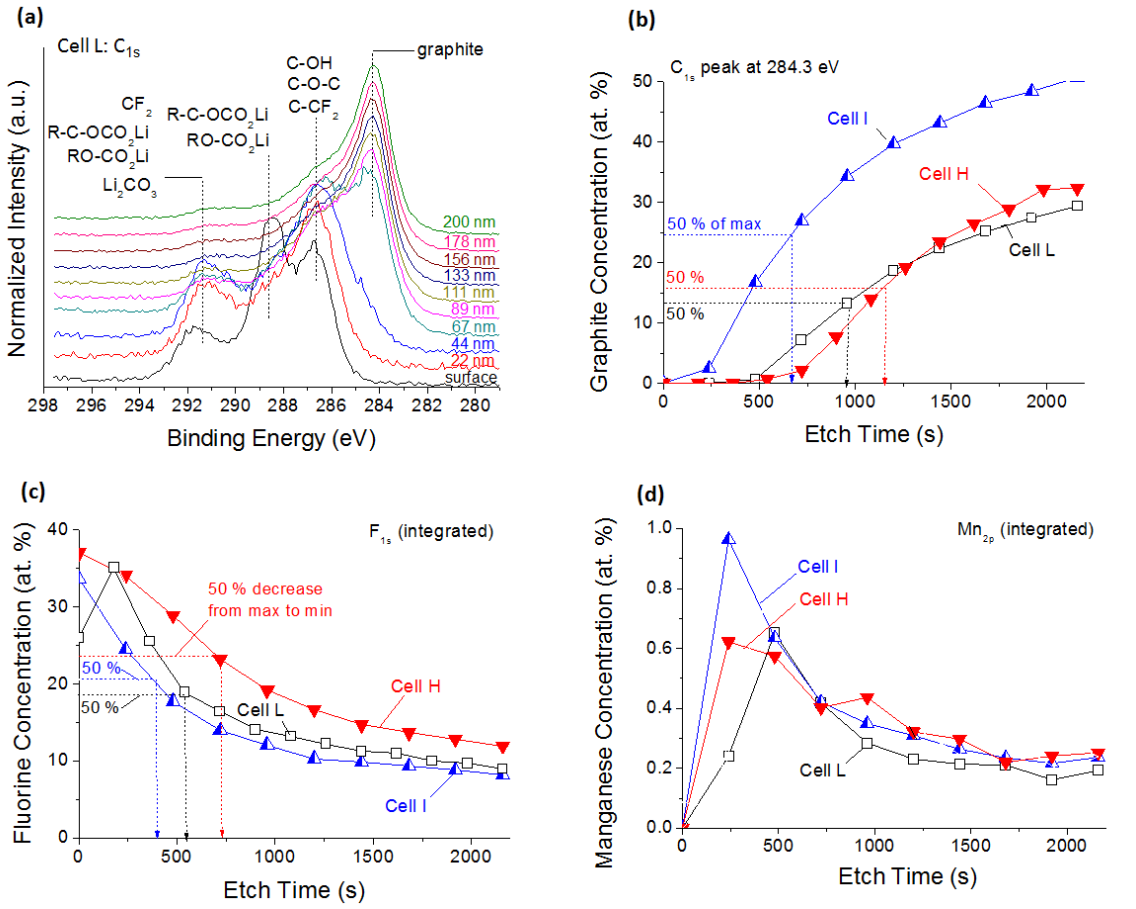

Figure 20. XPS studies on the graphitic anodes: (a) a typical change in the C_{1s} XPS spectra of an anode surface during Ar ion etching , (b) graphite, (c) fluorine and (d) manganese concentration at the surface as a function of the etch time. The depth in (a) was calibrated by argon ion etching of SiO_2.

In order to gain additional information about the type of bonds and obtain complementary information about the changes in the relative thickness of the SEI, we have conducted extensive XPS studies. Unfortunately, this technique requires considerably longer spectra accumulation time than SIMS, and thus XPS can only be performed in a static mode after etching a certain thickness of the electrode, as calibrated during sputtering of a SiO_2 layer by Ar^+ ions. Figure 20a shows the XPS C_{1s} spectrum for

the Cell L, while Figure 6b shows the depth spectra for all samples. Overall features of the spectra are as expected in a PC and EC based SEI. [109-112] Peaks were identified at ~284.3 eV (graphite), ~286.2 eV (C-O-C / C-CF_2), 287.5-288.5 eV (R-C-OCO_2Li / RO-CO_2Li), and 289-291.5 eV (RO-CO_2Li / Li_2CO_3/ CF_2) (Figure 20a).[97,105,113-115] The graphite peak at 284.3 eV does not appear until later etch depths, providing a tool for measuring relative SEI thickness.

Similarly to SIMS (Figure 19), the etch depths at which the graphite peak appears suggest that the SEI/PVDF thickness is evidently larger in the anode of Cell H compared to that of Cell I (Figure 20b). Surprisingly, however, and in contrast to the previously discussed SIMS data, the SEI/PVDF thickness is evidently larger in the anode of the Cell L compared to that of the Cell H (Figure 20b). We have performed the same measurements on 3 anodes from the Cell L and the results were consistent. We may offer two plausible explanations. First, the PVDF (binder) thickness in the Cell L was incidentally larger. Second, the resistance of the PVDF to sputtering by Ar^+ ions decreases during electrochemical cycling at elevated (45 °C) temperatures and is significantly higher in the anode of Cell L, which only was exposed to a formation cycle.

Finally, literature review revealed that Ar^+ ion milling for Kapton film can produce elemental carbon [116]. A similar process may be occurring with PVDF in this experiment, although this is not necessarily the case for several reasons. Firstly, whereas Kapton is largely composed of sp^2 hybridized aromatic carbon, PVDF is composed of sp2 hybridized carbon. Thus the overall carbon content of PVDF is lower than Kapton (33% and 56% respectively). This implies that more of the carbon will be removed by the ion etching for PVDF rather than converted to carbon as species such as $(C_2H_2)_nLi^+$, which

were detected by TOF-SIMS. Furthermore, XPS clearly shows a large composition of SEI components (Figure 20a) which further promotes such as species. Finally, the energy of the ions were kept low at 1 kV specifically to reduce ion damage, and lower energy impacts have been shown to reduce the conversion to elemental carbon [116]. Unfortunately, without a separate and detailed study, there is no way to confirm the extent to which ion milling has produced elemental carbon on the surface of the sample. Ar gas cluster ion beams can avoid this issue, but it should be also be alleviated with O_2 milling used in ToF-SIMS as elemental carbon should be converted to CO_2.

XPS studies also revealed the F concentration profiles in the samples (Figure 20c). Similar to the results of the C1s XPS, the F depth profile suggest the SEI/PVDF layer increases with cycling (compare anodes of Cells I and H in Figure 20c) with the anode of the Cell L not following this trend. The F_{1s} spectra are dominated by F bonded to Li (as in LiF), as was evidenced by the major F_{1s} peak positioned at ~686 eV, indicating LiF to be the major component of the SEI, corroborating prior studies [113]. The F bonding to C (as in PVDF) and to P (as in $LiPF_6$) have similar positions (see Table 4 and Table 5). This overlap does not allow obtaining separate profiles for F in the SEI and in the PVDF binder. In such situations, the XPS peaks of the other elements (e.g. P2p and C1s) are often used to separate the spectra. However, the C1s spectrum is much too convoluted to identify any individual chemical state. The P2p sensitivity factor is also ~1/4 of that of F1s and the P composition in $LiPF_6$ is 1/6 that of F. Thus peak deconvolution is not practical due to the extremely thick SEI layer.

The Mn profiles in the samples (Figure 20d) show good correlations with the distribution of the SEI, reaching a maximum composition just before the graphite peak

appears (Figure 21b). The Mn is not present at the very surface of the samples. This corroborates TOF-SIMS results on the presence of Mn in the SEI (Figure 19), and its tendency to accumulate at the graphite surface.[46] A bi-modal profile was not revealed by XPS due to much larger depth step size.

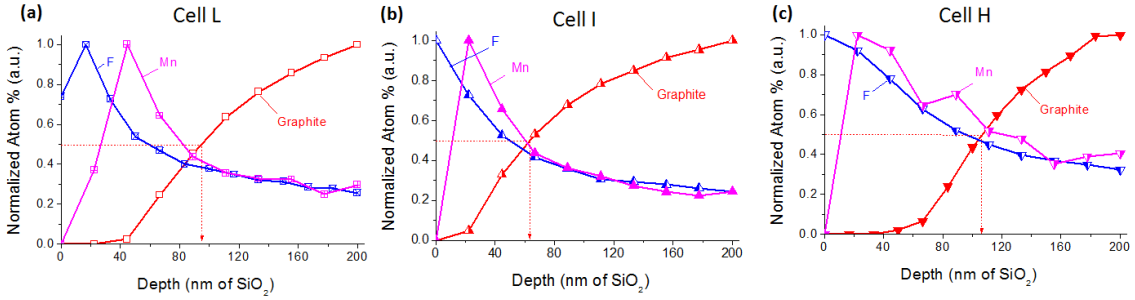

Figure 21. XPS depth profile showing a distribution of selected SEI and active material species in anodes of: (a) Cell L, (b) Cell I, and (c) Cell H through the depth of the SEI as well as into the underlying graphitic structure. The depth was calibrated by Ar ion etching of SiO_2.

Figure 21 shows the normalized XPS depth profiles of graphite, Mn and F within the top layer of the anodes taken from Cell L, Cell I and Cell H. The average SEI/PVDF layer thickness appears smaller from the XPS measurements (60-90 nm) than from the TOF-SIMS (140-230 nm) (compare Figure 19 and Figure 21). The difference between TOF-SIMS and XPS depth profiles can be explained by the different ions used. TOF-SIMS utilized O_2^- to maximize positive ion yield, while XPS utilized Ar^+, resulting in differing etch rates of species within the SEI. Therefore, as the SEI's chemical composition changes with degradation, the ion etch rate changes as well, depending on the particular ion utilized. As discussed earlier, in the case of the Ar^+ ion beam, elemental carbon can even be a byproduct produced by ion damage. The depth profiles for the other elements detected were generally not differentiable and thus are not shown.

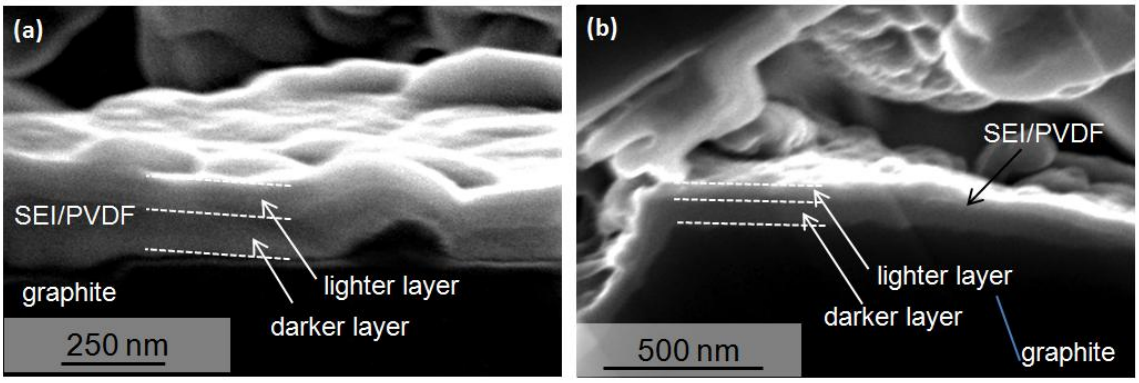

Figure 22. SEM of the SEI/PVDF layers in the anodes of (a) Cell I and (b) Cell H, after being cross-sectioned by FIB.

In order to directly identify the thickness of the SEI/PVDF layer in various cells and better calibrate both the TOF-SIMS and the XPS depth profiles we have cut individual graphite particles within the electrodes of various cells using FIB and performed SEM analysis on the cross-section of these particles. Unfortunately, the thicknesses of the SEI/PVDF layers within individual anodes (and even within individual anode particles) vary significantly, which demands analysis of multiple samples for statistically meaningful data. However, FIB sample preparation is an expensive, elaborate, and time consuming procedure. The preparation of a large number of samples to gain better statistical distribution of the SEI/PVDF thicknesses in each sample is not practical. From the samples prepared and analyzed we found that the average SEI/PVDF layer thickness increases from 111.36 (± 55.43) nm in the anode of Cell L to 169.78 (± 78.85) nm in the anode of Cell I and finally to 314.56 (± 187.22) nm in Cell H. Each average thickness was calculated using an image processing program Fiji. The polygon area of the SEI was divided by the total length of SEI from at least three different images. Figure 23a compares the changes in the relative thickness of the SEI/PVDF layer deduced from the TOF-SIMS, XPS and FIB-SEM measurements. The average thicknesses were normalized by the thickness of such a layer in the anode of Cell I.

Whereas the thickness increases from Cell I to Cell H and the values are consistent and comparable by all three techniques, large and inconsistent variations were observed with Cell L. Large variations in the thickness in the PVDF binder layer likely contribute to such inconsistencies.

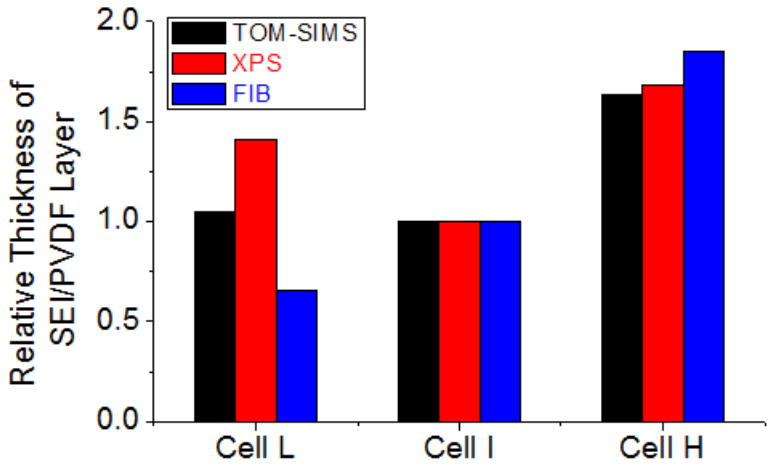

Figure 23. Studies of the SEI/PVDF layers: (a) comparison of the average SEI/PVDF thicknesses in Cells L, I and H, as identified by TOM-SIMS, XPS and FIB-SEM techniques.

Our SEM studies of the cross-sections of the individual particles in the anodes of Cell I and Cell H revealed the presence of two separate layers with different contrast within the SEI/PVDF (the brighter layer being closer to the surface). This distinction was particularly clearly seen in the thicker layers (Figure 22 b,c). The brighter region in SEM images indicates either the presence of heavier elements, such as F from LiF (Figure 20c) or the lower electrical conductivity of such a layer. The presence of the two layers within the SEI/PVDF corroborates the bi-modal distribution of Mn^{+} and Li^{2+} revealed by TOF-SIMS (Figure 19). Identifying the origin of the dual-layer formation is beyond the scope of this manuscript. Yet, we offer several potential explanations: (i) surface oxidation of mobile ions at the surface SEI layer, (ii) formation of a PVDF-free SEI layer near the

graphite surface, (iii) the dual-layer nature of the SEI. First, during sample preparation for analysis, the diffusion of Mn and Li to the surface layer and their unintentional oxidation shall result in the formation of the electrically isolative metal oxides. Such oxides will cause stronger scattering of secondary electrons. Second, the permeation of the electrolyte solvent through the PVDF may induce the SEI formation not only within the PVDF, but also in between the PVDF and graphite particles. The PVDF-free SEI layer may exhibit different (slightly darker) SEM contrast. Finally, prior studies of SEI on graphite proposed a compact-stratified layer model, which assumes an SEI composed of two layers. [117] Another commonly accepted model assumes the SEI is composed of a mosaic of microphases, which may also form separate layers. [118]

5.4. Conclusions

In this study, we compared TOF-SIMS, XPS, and FIB/SEM techniques for investigation of the SEI layer formed on the graphite anode. All three techniques were capable of identifying the changes in the overall thickness of the SEI/PVDF layer with cycling. FIB/SEM was found to be the most time consuming technique. However, it allows direct visualization of the layer thickness. In contrast, both TOF-SIMS and XPS rely on the calibration of the surface etching rate by ions using silica thin films. Electrode compositions, however, exhibit various etching rates which are different from each other and that of silica. In addition, the calibration of the sensitivity of TOF-SIMS to the detection of various elements is challenging and specific to bonding. Therefore, exact identification of the chemical composition of the surface layer (in terms of atom % of various elements) becomes impractical. However, the high SIMS analysis speed

combined with the opportunity to construct high-resolution depth profiles of the various elemental compositions over the large sample area is very appealing. In addition, SIMS allows one to clearly detect trace elements, such as Mn and record their depth profiles. XPS uniquely provided overall compositional information of the surface layers. The long detection time required by XPS makes the depth-profile acquisition very time consuming. Therefore, the resolution of depth profiles becomes too low to distinguish fine peaks in the elemental distributions, a feature possible by TOF-SIMS. The sensitivity of XPS was sufficient to detect the presence of Mn, and show its approximate atom % and accumulation at the surface of the graphite. Finally, to fully understand ion beam depth profiling, detailed studies are necessary to understand how the ion beam interacts with binders and SEI components.

Chapter 6. Degradation Analysis of High Power Commercial Cell

6.1. Introduction

Based on the previous analysis reported in Chapter 5, it was determined that, of the three methods, ToF-SIMS was most efficient and reliable method for performing depth profiling of the electrodes. XPS can be used for depth profiling, and did reveal the Mn composition change with depth. However, for this second study of commercial cells, XPS was used to deduce chemical information about the SEI on the anode and cathode of commercial cells.

In addition, this project had an expanded ambition to provide a mechanistic understanding for the phenomenological models of Li-ion battery degradation. A systematic study was performed on the possible degradation mechanisms by which the battery could fail. In terms of XPS analysis, this provides a broad context in which to understand the SEI and its impacts on the battery as a whole. Commercial cells employing NCM positive electrodes and hard carbon negative electrodes were calendar-aged at high temperature (75 °C) to accelerate degradation. Reference electrochemical tests and post-mortem analysis were done to evaluate cell performance due to aging and to examine cell components including electrodes, separator, and electrolyte. Results are presented showing power and capacity fade with aging. Based on this electrochemical and post-mortem analysis, a mechanism for increased cell resistance in a power optimized commercial cell is discussed.

6.2. Experimental Methods

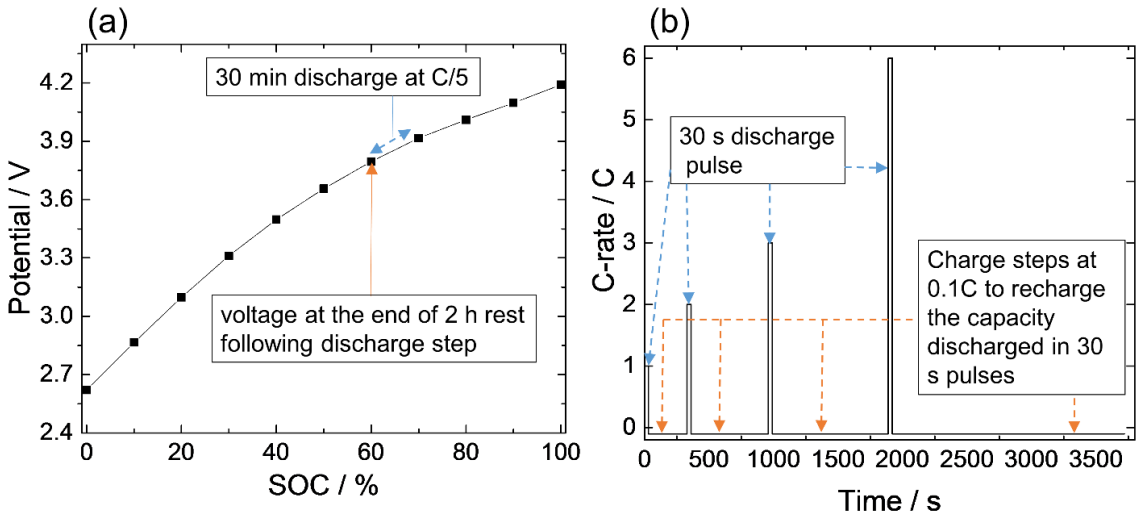

Figure 24. (a) SOC-OCV curve for a fresh cell. Fully charged cell at 4.2 V is at 100 % SOC. 30 min discharges are performed at C/5 followed by a 2 h rest; (b) Current profiles used to measure the cell resistance during discharge. The cell was discharged using 30 s pulse at 50 % SOC. After each discharge step, capacity lost during the discharge step was recharged using 0.1 C current. To measure the charge resistance, 30 s pulse currents at 1C, 2C, 3C, and 6C were used to charge the cell, followed by discharging the capacity increased during charging step.

Commercial lithium-ion prismatic cells (EH4, Blue Energy) with NCM positive electrodes and hard carbon negative electrodes were used in this study. Initially, capacity testing was done by charging and discharging the cell using a constant current of 4.7 A based on the nominal capacity of 4.7 Ah for the cell, as rated by the manufacturer. The upper and lower voltage limits were set at 4.2 V and 2.4 V respectively. These limits follow the manufacturer recommendations for the battery. Based on the cell capacity from initial testing, the state-of-charge (SOC) vs. open-circuit voltage (OCV) curve was determined. This curve is useful to monitor the SOC of the cell based on the cell potential. A SOC of 100 % represents a fully charged cell whereas a SOC of 0 % represents a fully discharged cell. The profile used to derive the SOC-OCV curve for the cells at the beginning of testing is illustrated in Figure 24. A fully charged cell at 4.2 V (100 % SOC)

was discharged using a current of C/5 in 30 min steps. Each discharge step was followed by 2 hour rest period to allow the cell to equilibrate. The steady-state voltage at the end of the rest period was used to build this curve. Each discharge step lowered the SOC of the cell by approximately 10 %. The process continued for 10 discharge and rest steps or until the cell reached the lower voltage limit.

High temperature aging was accomplished by storing the cells at 75 °C. This test was carried out at a vendor's lab, and the cells were received in our lab after aging was completed for the intended duration. The cells were charged to a voltage corresponding to 90 % SOC (from the SOC-OCV curve) and stored in an environmental chamber. The capacity and resistance of the cells were measured every 400 hours during the aging process. These reference tests were performed after cooling the cells to 25 °C and are similar to the HPPC tests proposed by the U. S. DoE [119]. Cell capacity was measured by charging the discharging the cell using a constant current at 1C, based on the capacity from initial cell testing. Resistance measurements were performed on the cells at 50 % SOC. Cells were charged to a voltage corresponding to 50 % SOC by following these steps: discharge the cell at 1C to 2.4 V, rest for 30 minutes, charge at 1C to corresponding voltage at 50 % SOC determined from the SOC-OCV curve, hold the potential until the current drops below 0.05 C and then hold for 30 additional minutes at 50 % SOC before testing. The so called "cell resistance" was measured by charging and discharging the cells at different rates (±1C, 2C, 3C, and 6C) for 30 seconds at 50 % SOC. The profile used to measure the cell resistance during discharge is illustrated in Figure 24. Starting at 50 % SOC, the cell was discharged using pulse currents at 1C, 2C, 3C, and 6C for 30 seconds. After each discharge step, the cell was recharged at 0.1C until the capacity lost

during the discharge step was matched (counting coulombs) to get the cell to the same starting SOC before another discharge pulse. A similar current profile was used to measure the cell resistance during charge. Starting at 50 % SOC, the cell was charged at 1C, 2C, 3C, and 6C for 30 s. After each charge step, cell was discharged at 0.1C until the capacity added to the cell during the charge pulse was matched.

Heat generation may occur in lithium-ion batteries when the cell potential deviates from the equilibrium value. Interfacial kinetics, concentration overpotentials, and ohmic losses can lead to deviation from the equilibrium value and heat generation in batteries. These losses are higher at high rates [120,121]. High internal cell temperature due to heat generation may lead to increased side reactions at the electrode-electrolyte interface, oxygen evolution at the positive electrode, electrolyte evaporation, and melting of the separator membrane. Cell performance degradation and, in worse cases, cell failure and thermal runaway may occur due to excessive heat generation in lithium-ion batteries [120]. As described earlier, the cell used in this study was designed for high power applications; and the 30 s pulse currents at up to 6C for the cell at 25 °C during reference tests should not contribute significantly to cell degradation. Furthermore, since aging for this cell was achieved by soaking the cell at 75 °C, high temperature aging is the primary mode of performance degradation for the cell [120].

Pulse charges and discharges were carried out for the cell at 50 % SOC using 1C, 2C, 3C, and 6C currents for 30 seconds. Resistances for charge and discharge were obtained by using the voltage at 30 seconds from the start of the charge or discharge current and using the slope of the I-V curve. Thus measured resistance is referred to as "cell resistance" and is different from the internal resistance or the ohmic resistance of

the cell. When current is flowing in a battery, the resulting voltage is dependent on the open-circuit potentials of the electrode materials as well as ohmic losses, the charge-transfer overpotentials and concentration overpotentials in the cell. Thus, cell resistance measured by applying current pulses of tens of seconds depends not only on the ohmic losses, but also on the kinetic and mass-transfer polarizations.

Three cells were taken at different stages of aging for analysis: Fresh cell—cell with no aging, as received from the manufacturer; 1600h cell—cell aged for 1600 hours; 3200h cell—cell aged for 3200 hours.

Post-mortem analysis tests were done after discharging the cell completely (discharge to 1 mV) and opening under inert (argon) atmosphere in a glovebox. To prepare electrodes for analysis, they were soaked in dimethyl carbonate (DMC) to remove Li salt and were dried at room temperature inside the glovebox. Postmortem tests included capacity tests of positive and negative electrode half cells, four point probe resistivity measurements, x-ray photoelectron spectroscopy (XPS), time of flight secondary ion mass spectroscopy (TOF-SIMS), and transmission electron microscopy (TEM). In order to estimate the capacity of the half-cells using positive electrode recovered from the full cells, the following procedure was used: (i) constant current charge (0.95 mA—1.5C based on discharge capacity of positive electrode half-cell) until voltage reached 4.2 V, (ii) voltage hold until current dropped below 0.012 mA or total charge time reached 24 hours, (iii) rest period of 10 minutes, (iv) constant current discharge (0.95 mA) until voltage dropped below 2.4 V, (v) rest period of 10 minutes. A similar procedure was used to estimate the capacity of the half-cells using negative electrodes. The cycling procedure used was as follows: (i) constant current discharge

(0.95 mA) until voltage dropped below 5 mV, (ii) voltage hold until current dropped below 0.012 mA or total discharge time reached 24 hours, (iii) rest period of 10 minutes, constant current charge (0.95 mA) until voltage reached 1.5 V, (iv) rest period of 10 minutes. The above steps including the voltage limits and currents used to estimate half-cell capacities were prescribed by the manufacturer. For the four point probe measurements a Signatone (SYS-301-6) with a tip spacing of 1.016mm was used in conjunction with a Keithley 2182A Nanovoltmeter and a Keithley 6224 DC current source using 5s current pulses of -100-100mA in 20mA intervals. For XPS analysis, a Kratos Axis Ultra was used with an Al k-alpha X-ray source and 20 eV pass energy for detailed scans and 200 eV pass energy for survey scans. Points were taken at 0.1 eV intervals for 100 ms and repeated 5 times for detailed scans and 1 time for survey scans. Atomic composition was calculated from the survey scans. A vacuum sealed transfer chamber was used to protect samples from air exposure during sample transfer. The resulting detailed spectrum was analyzed using Avantage software, using combined Shirley-linear backgrounds and Gaussian peaks of the same FWHM for each element energy level. TOF-SIMS depth profiling was done using an IONTOF TOF-SIMS 5-300 in positive ion collection using a 25kV Bi^+ primary and 2kV O_2 sputter gun and 150 x 150 μm collection area. Sputter depth was calibrated vs. the time required to sputter through a 200 nm SiO_2 coated Si wafer to avoid depth discrepancies due to different sputter rates between materials. TEM analysis was performed by a Tecnai G2 F30 (FEI, Netherlands) operated at an accelerating voltage of 300 kV. The electrodes were immersed in DMC under inert gas (Ar) and sonicated to be separated from the current

collector and dispersed in solvent. Electrode powders dispersed in DMC solvent were drop casted on TEM grids for imaging.

6.3. Results and Discussion

6.3.1. Electrochemical Observations of Cell Degradation

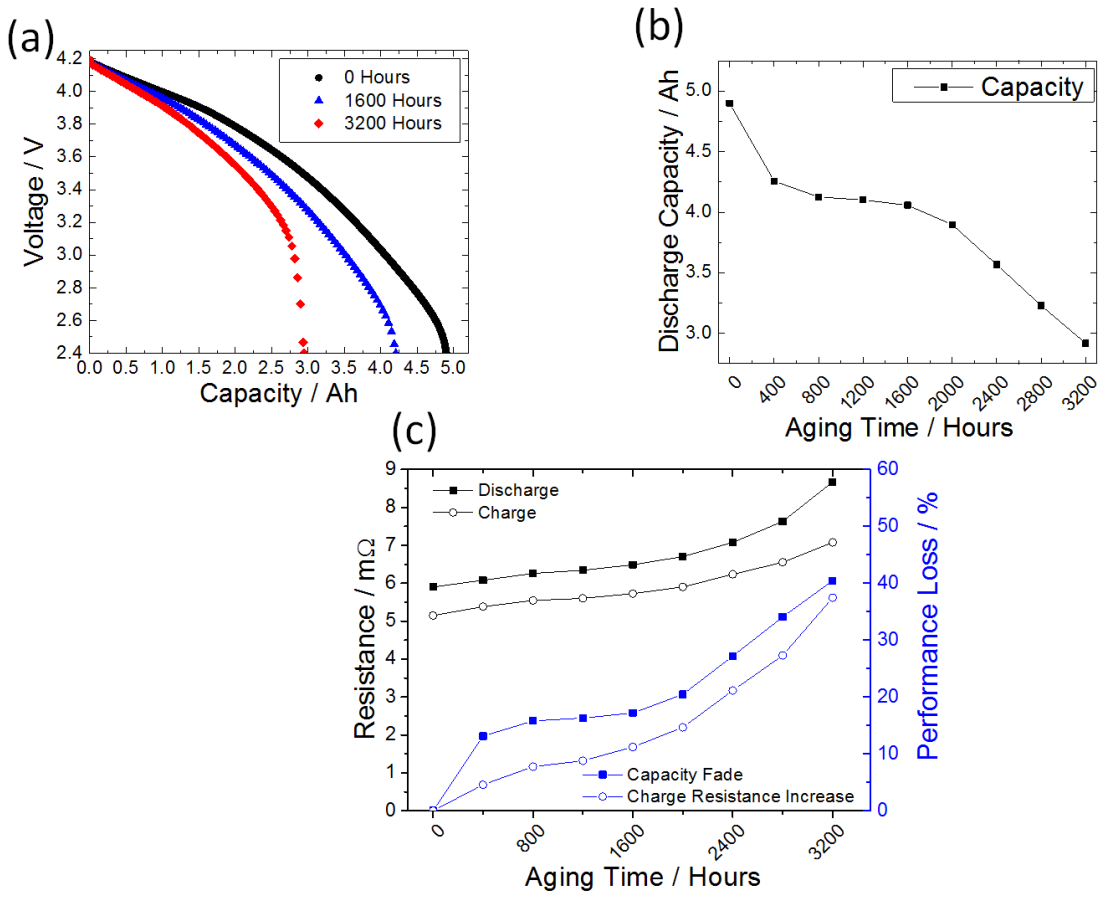

Figure 25. (a) Capacity-voltage profiles during 1C discharge for full cells with no high temperature aging, 1600 hours aging, and 3200 aging; (b) Decrease in cell capacity with aging; (c) Increase in charge and discharge cell resistance with aging (in black) and performance loss from capacity and resistance increase with aging time as a percentage change (in blue).

The discharge capacities of the three cells with different degrees of aging are compared in Figure 25a. The decay in capacity with aging at each reference point of 400 hours is shown in Figure 25b. Compared to the initial discharge capacity of the cell, the cell lost 13% capacity in the first 400 hours, another 4% in the next 1200 hours, and another 23% in the next 1600 hours. There are clearly two stages at the beginning and the end of the aging when most of the discharge capacity loss is seen. Additionally, the shape of the voltage profile did not significantly change after 1600 hours, but shows a precipitous drop between 3 and 2.4 V after 3200 hours (Figure 25a).

Figure 25c shows the degradation of the cell in terms of resistance, in comparison to the capacity fade. The resistance increase does not show the initial jump that the capacity fade does. However, both the capacity fade and the resistance increase accelerate at later stages of aging after 1600 hours. Thus it appears that the later stage of capacity fade and increase in cell resistance are due to related phenomena. Both charge and discharge resistance showed similar trends, although discharge resistance was greater, and accelerated at a faster rate at later stages of aging.

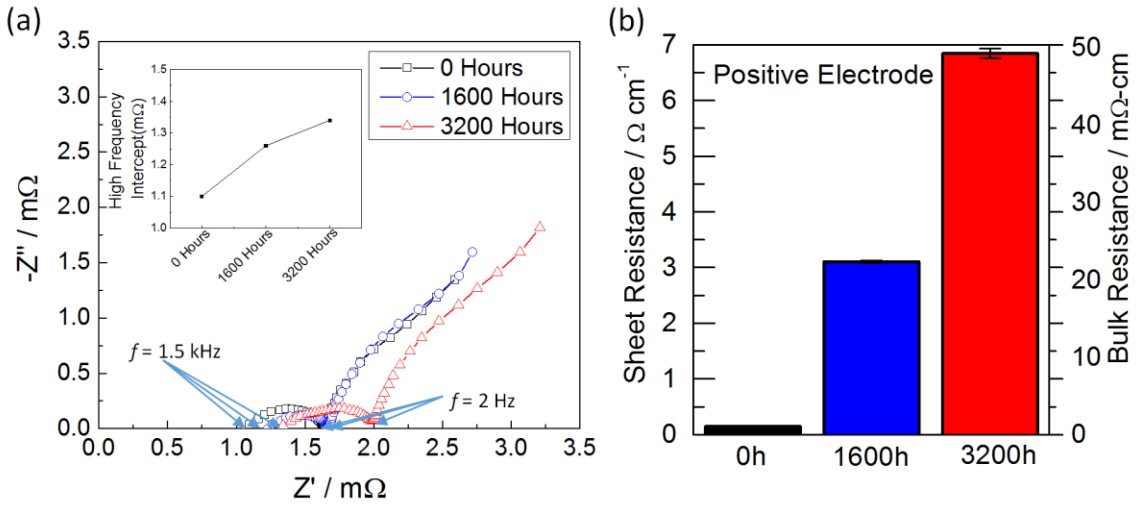

Figure 26. Resistance measurements via (a) EIS spectra of full cell showing increase in high frequency impedance at 4.2 V and (b) four point probe of positive electrode showing increasing electronic resistance.

Electrochemical impedance spectroscopy (EIS) tests were done to quantify different types of impedance contributions to total cell impedance. EIS allows separation of different processes based on their characteristic time constants. A typical result is presented in a Nyquist plot containing semi-circles and inclined lines which represent the time constants associated with the different physical processes. The impedance response of a lithium-ion porous electrode can contain a semi-circle in the high frequency region, which is associated to surface-layer impedance. Semi-circles at medium frequencies are related to charge-transfer impedance. Often, the semi-circles at high frequencies and medium frequencies overlap and are present as a flattened or depressed semi-circle from high to medium frequencies on a Nyquist plot. In addition, the results shown Figure 26 are from full cells, and therefore are a result of processes happening at both the positive and negative electrodes.

The high-frequency intercept in EIS spectra provides the internal resistance of the cell. This impedance is comprised of the solution resistance, electronic resistances in the

electrodes, and all contact resistances including the surface layer films. From comparisons shown in Figure 26, the high frequency intercepts of the cells follow an increasing trend with the extent of degradation. This increase in impedance is highlighted in the inset in Figure 26. It is important to note that although this internal resistance increased with aging, it is much smaller than the cell resistance shown in Figure 25c. During *ex-situ* post-mortem testing of the electrolyte from the cell, the electrolyte conductivity remained essentially unchanged (around 3 % decrease from Fresh to 1600 hours). Thus, the increases in the internal resistance are attributed to changes in the negative and positive electrodes.

On the other hand, the 2 Hz point at the end of the surface-layer and charge-transfer impedances show a slight increase in real impedance (x-axis) after 1600 hours and a large increase after 3200 hours. This indicates that the sum of surface-layer and charge-transfer portions of the cell resistance grew more rapidly at the later stages of aging.

6.3.2. Post Mortem Analysis

Four point probe was performed on anode and cathode electrodes in order to determine the electrical resistance and confirm the results of the full-cell EIS tests. As this test removes the material from the coin cell the effects of contact/internal resistance are minimized. These materials are also tested in a dry state so all ionic conductivity paths are eliminated. These results are shown for the cathode electrode in Figure 26b with the electrical sheet resistance increasing from 0.15 to 6.8 Ω sq-1 or 1 to 49 mΩ-cm for the bulk resistivity. Anode resistance measurements did not show appreciable changes after 3200 h aging and are not reported here.

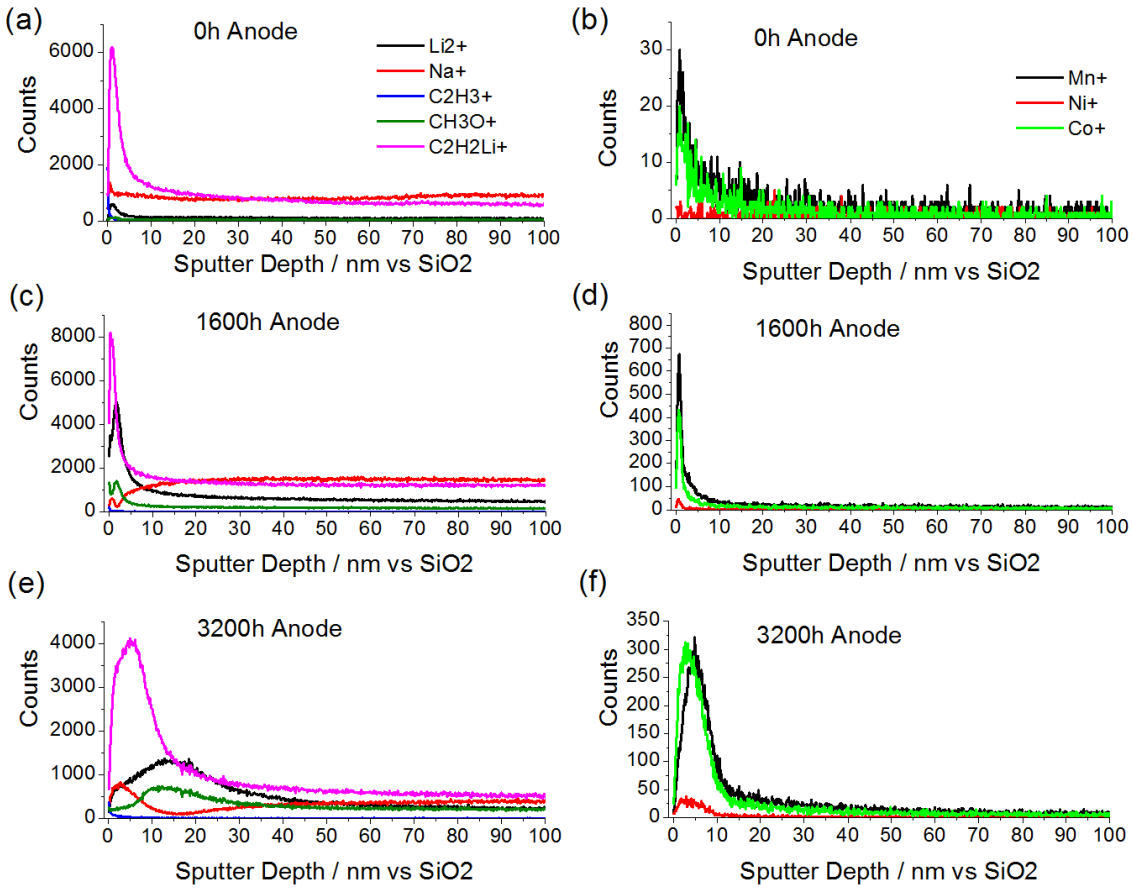

Figure 27. SIMS depth profile showing (a,c,e) left three figures surface layer formation on the negative electrode and (b,d,f) right three figures deposition of Ni, Mn, and Co onto the negative electrode from cathode active material.

Depth profile investigations on the positive and negative electrode surface (Figure 27 and Figure 28) with aging were performed using TOF-SIMS analysis. The sputter rate for depth profile was measured using a SiO_2/Si standard. The ion beam etching/sputtering on the composite porous electrode such as NCM does not remove the electrode material uniformly due to the electrode consisting of individual particles with pores rather than a flat, thin film. This results in broad elemental distributions in SIMS profiles instead of sharp interfaces. Furthermore, different elements have variable TOF-SIMS sensitivity and detection limits. The ionization efficiency in dynamic SIMS depends on the surface composition and structure [46]. Thus, the sputter time taken during SIMS analysis of

composite porous electrodes may be indicative of not only the true sputter depth or electrode thickness but also of longer sputtering period due to an artifact of the sputtering process.

Species of interest for organic and inorganic SEI compounds were selected based on intensity of the peaks and variation with respect to depth and the strongest peak for each fragment series (Ex: $C_2H_3^+$ vs $C_2H_4^+$, and $C_4H_6^+$) was chosen. The species and their respective masses include Li_2^+ (14.03 Da), $C_2H_3^+$ (27.02 Da), CH_3O^+ (31.03 Da), and $C_2H_2Li^+$ (33.03 Da) while the transition metals were also selected Ni^+ (57.93 Da), Mn^+ (54.94 Da), and Co^+ (58.93 Da). Presence of surface species related to the SEI formed on graphite negative electrodes were verified by TOF-SIMS on the negative electrode, and appears to grow particularly rapidly between 1600 and 3200 hours (Figure 27). The FWHM of the $C_2H_2Li^+$ species is 3 nm, 2 nm, and 10 nm for the 0, 1600, and 3200 hour samples. All other species including Mn, Ni, and Co generally follow a similar trend, although the Li_2^+ CH_3O^+ species peaks shift to a deeper sputter depth.

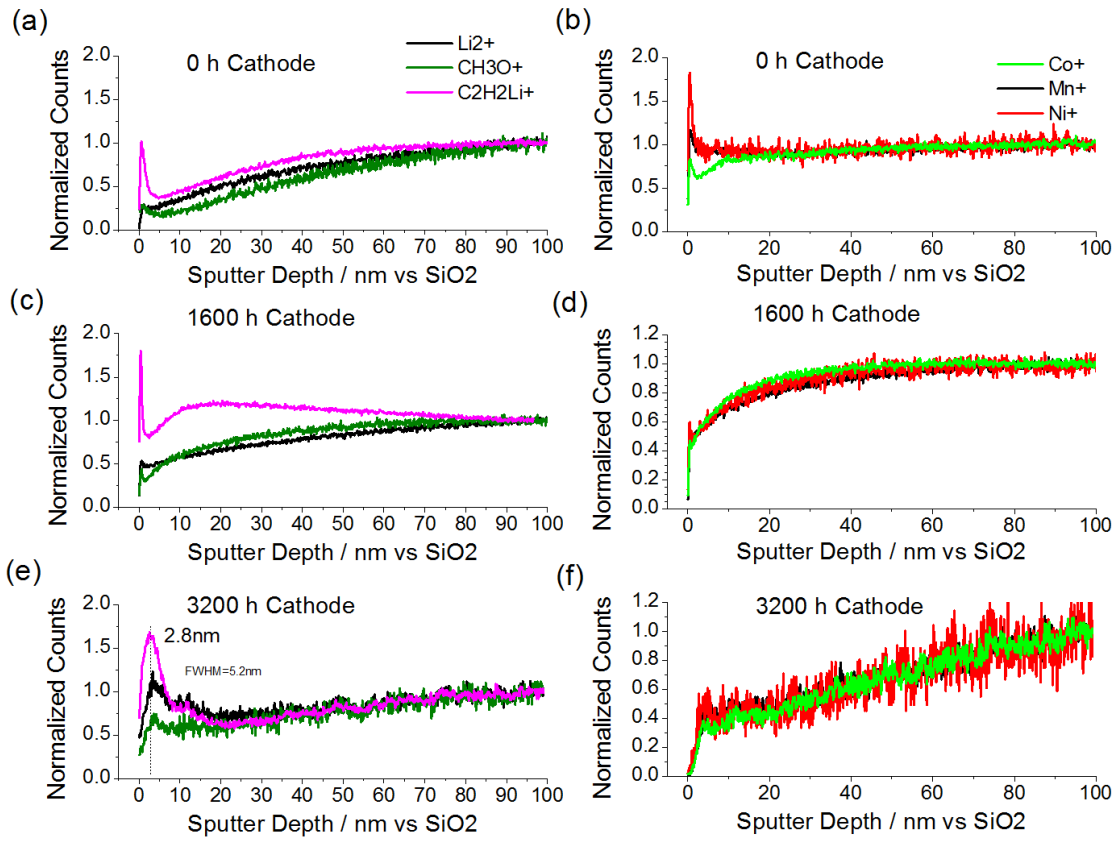

Figure 28. SIMS depth profile showing (a,c,e) left three figures surface layer formation on the positive electrode and (b,d,f) right three figures rate of active material dissolution increases in aged positive electrode. The counts were normalized so that the count at the bulk of the electrode is one.

For the cathode plots (Figure 28) intensities or counts presented in the figures were normalized to one, so that the count at the bulk of the material is one. The was not done for the anode, as all the species faded towards 0 in the negative electrode. Figure 28a,c,e shows the growth of a SEI-like surface layer on the cathode as seen from the increasing FWHM of the $C_2H_2Li^+$ species from 1.5 to 1 nm to 5.2 nm after 0, 1600, and 3200 hours. This cathode surface layer has been observed in different electrode materials in the literature and is known as the solid permeable interface [122]. The thickness of the solid permeable interface on cathodes can increase significantly with increasing temperatures [122]. The high temperature and state of charge in this study likely contributed

significantly to the growth of this layer as the total amount of electrochemical cycling was very low. In Fig. 6 (b), the surface composition of transition metal species constituting the positive electrode is shown. As aging proceeds, these species appear to be further removed from the surface as shown by a gradually increasing depletion layer which eventually flattens into a linear depletion layer after 3200 hours. This process is more substantial than the film formation as evident by the depth/thickness observed (100 nm vs. 5 nm for the cathode surface layers) and is likely due to the increased dissolution and loss of the materials from the cathode. Transition metal dissolution is known to occur in NCM electrodes, and dissolution is exacerbated at high temperatures and high potentials [46,123]. Aging the cell for an extended duration at a potential above 4 V (at 90 % SOC) at 75 °C likely led to the removal of transition metal species from the positive electrode surface and increased dissolution with aging time.

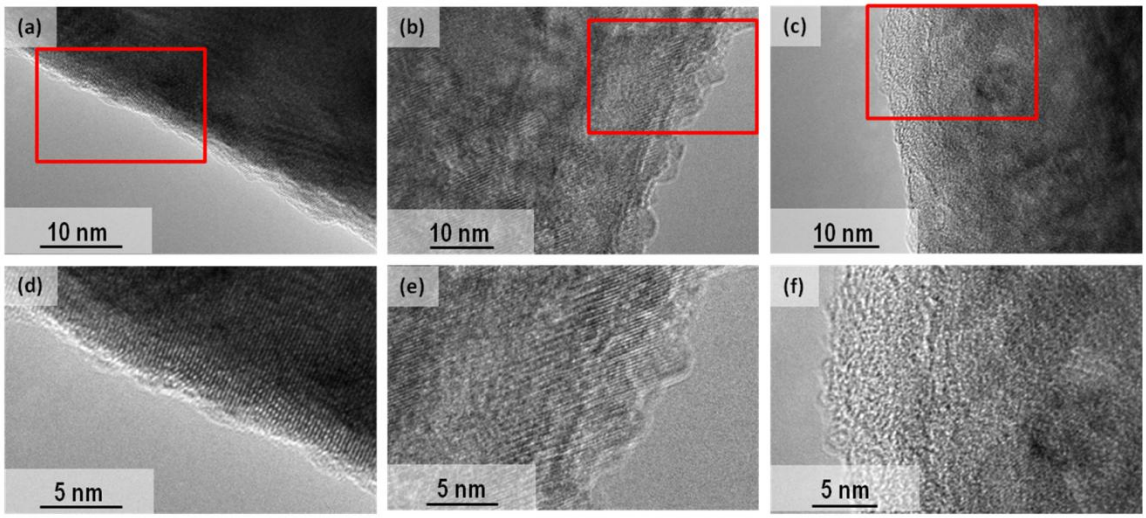

Figure 29. High resolution TEM images of positive electrodes samples recovered from cells after aging (a) 0 Hours, (b) 1600 Hours, and (c) 3200 Hours and their magnified images (d, e, f).

TEM was used to analyze the cathode surfaces and directly observe the surface layer, as differences were not identifiable by FIB/SEM. The cathodes were immersed in

DMC and sonicated to disperse the powders and drop casted onto a grid. For all samples multiple particles were investigated to ensure reproducibility. Fig. 7 shows high resolution TEM images of fresh, 1600 hours and 3200 hours cathode samples. The surface of fresh cathode samples (Figure 29a,d) were very clean and the same crystalline structure is discernible up to the edge of the particle. After 1600 hours of aging however, a lighter shaded amorphous surface layer appears to be beginning to form (Figure 29b,e), while after 3200 hours, the layer becomes distinct (Figure 29c,f). TEM micrographs of other regions of the samples showed the same trend (See Appendix B). As a PVDF binder or other organic layer would most likely be removed by TEM beam damage, this layer is most likely an inorganic amorphous surface layer formed by the degradation of active material and/or electrolyte.

6.3.3. XPS Post Mortem Analysis of the SEI

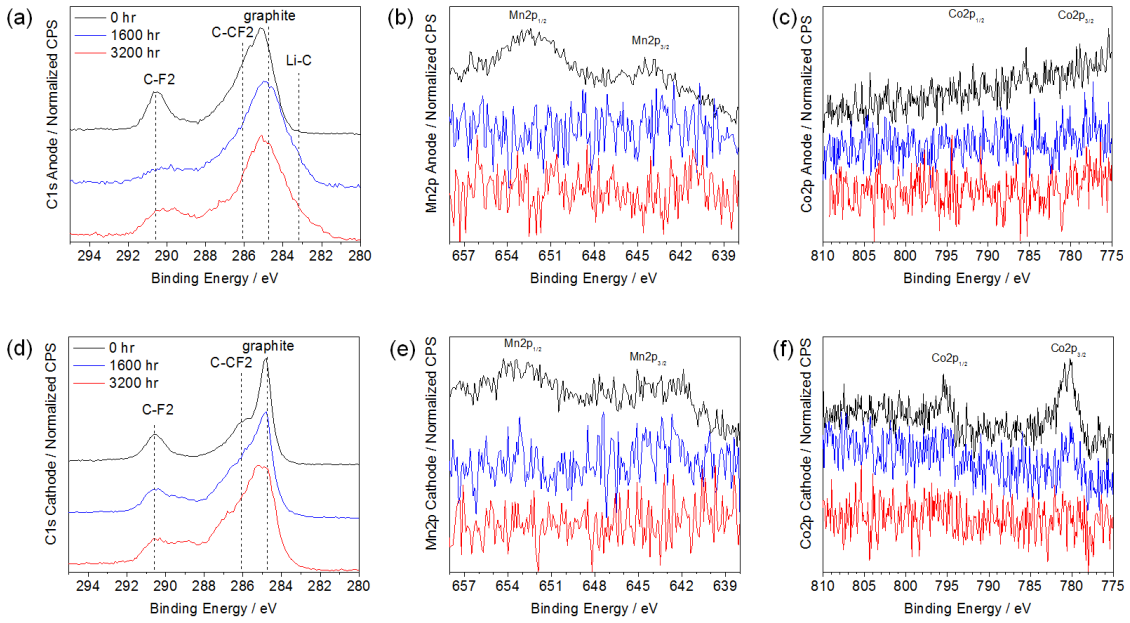

Figure 30. XPS spectra for (a-c) anode and (d-f) cathode recovered from full cells with different aging times denoted by color.

The nature of the surface layers formed on the anode and cathode were further inspected using XPS. Figure 30a,d and Table 1 show the C 1s spectra of anode and cathode recovered from full cells after different stages of aging. The fitted peaks, and fit envelope are shown in comparison to the raw data in Appendix C. Several peaks related to an SEI layer typically formed on carbonaceous anode were identified. The C1s spectra for both electrodes generally show broader and stronger peaks, chemical decomposition in the SEI resulting in more varied chemical states. Based on literature and reference samples, PVDF C-CF_2 and C-F_2 peaks were identified at 286.2 and 290.5 eV respectively and were used to adjust the spectra for charge shifts [97]. Based on the shape of the experimental data obtained, a graphitic sp2 carbon peak was identified at 284.8 eV with FWHM ~ 0.7 eV for the fresh and 1600 hour aged cathode, while the more general sp3 hydrocarbon peak was identified at 285 eV in all electrodes with FWHM the same as the other C 1s peaks. A good fit could not be achieved without this sharper graphitic peak unless many more Gaussian peaks were added. The smaller FWHM is most likely due to a more uniform chemical state in the crystalline graphitic carbon, whereas the peaks from the PVDF and SEI material have wider FWHM due to varied chemical states in the material. Difference in conductivity also most likely affected the FWHM of the peaks as well, as the SEI is electrically resistive. The fresh, 1600 hour, and 3200 hour C1s peaks (other than the graphitic peak) had FWHM of approximately 1.3 eV, 1.9 eV, and 2.1 eV for the anode and 1.2 eV, 1.7 eV, and 1.6 eV for the cathode respectively. The FWHM was allowed to vary within 0.1 eV of the reference peak (C-F_2 or C-C sp3). The graphitic peak in the anode had FWHM of 0.9 eV, but was not necessary to achieve a good fit.

The anode additionally had a peak identified at ~283.3 eV at 1600 and 3200 hr aging assigned to C-Li, which does not normally appear in a fully delithiated anode. Considering the large degree of SEI growth and the lack of a sharp graphitic carbon peak, this material is in the SEI layer. Such a material has never before been reported in the SEI in literature. However, the formation of a C-Li bond is not impossible considering the electrochemical potential. Furthermore, the extremely high aging temperature and 4 month long aging process may have activated a stage of degradation of reaction pathway not normally observed in aging tests.

Table 7. Percent atomic composition of XPS C1s peaks from anodes and cathodes after the formation cycle (fresh), after 1600 hours, and 3200 hours of aging at 75 ºC.

		Anode			Cathode		
Approximate BE (eV)	Name	Fresh	1600 hr	3200 hr	Fresh	1600 hr	3200 hr
283.3	C1s C-Li	-	2.0	5.0	-	-	-
284.8	C1s graphite	1.4*	-	-	9.7	5.0	0
285	C1s C-C sp3	19.0	9.8	19.0	12.1	24.1	20.6
286.2	C1s C-CF_2	8.3	1.7	0.2*	10.8	11.0	4.5
287.3	C1s C-O_2	4.2	2.8	5.4	3.5	4.6	7.4
289	C1s $ROCO_2Li$	1.7	0.9	0.9	1.4	4.1	4.0
290	C1s Li_2CO_3	-	0.2*	4.8	-	-	-
290.5	C1s C-F_2	6.5	1.1	0.2*	8.3	7.4	4.5

Below the detection limit of XPS. See Appendix C.

Additional peaks were also identified and assigned using literature where possible, and are listed in Table 7. With increasing aging, the graphite peak first diminishes and then disappears, followed by a steady decrease in the PVDF C-CF_2 and C-F_2 peaks. This clearly shows the growth of the surface layer on both the anode and cathode. Furthermore, the peak at 289 eV assigned to $ROCO_2Li$ becomes weaker in the anode. This suggests a

changing SEI composition, perhaps with the reduction of $ROCO_2Li$ to Li_2CO_3. The fact that this occurs first on the anode shows that the surface layer is thicker on the anode, as expected.

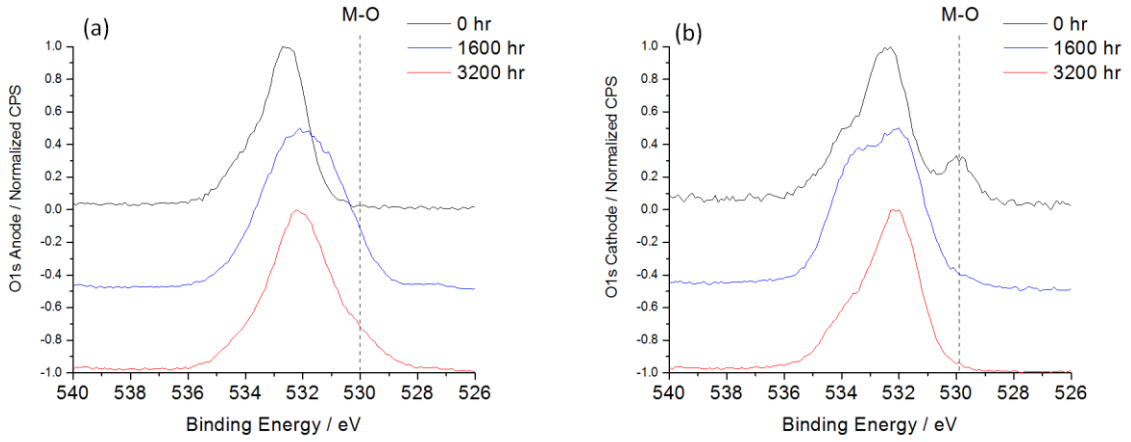

Figure 31. XPS O 1s spectra of the (a) anode and (b) cathode samples at fresh, 1600 hours, and 3200 hours of aging.

The fresh cathode also had a clear O1s M-O peak at 530 eV whereas the 1600 hr and 3200 hour aged samples did not (Figure 31), indicating that the surface layer growth on the cathode is covering the NMC active material. Such a layer may assist in slowing the dissolution of transition metals from the cathode [124]. The anodes also show a Li_2O peak at 530.3 eV for the 1600 hours and 3200 hours samples, a commonly observed SEI component [125], although it can also be formed by air exposure [86].

Figure 30b,c,e,f show the anode and cathode spectra for Mn 2p and Co 2p. Interestingly, although the weakening peak intensity of Mn and Co on the cathode are reasonable considering the growing surface layer, Mn is observed on the anode for only the fresh 0 hour sample. However, Mn and the other transition metals are not observed on the anode after aging. This is most likely due to Mn being covered by a thick layer of SEI.

Mn deposited on the anode is associated with a growth in SEI impedance and capacity fade [126,127].

Finally, it is necessary to address the discrepancy between the ToF-SIMS and XPS results. Whereas XPS showed a gradually growing SEI layer with the anode having a thicker SEI, ToF-SIMS failed to characterize this. This is most likely due to air exposure and beam damage from the O_2 ion beam used to mill the sample. XPS, on the other hand, shows chemical information for relatively pristine electrodes undamaged by experimental conditions (except possibly UHV), and thus is more reliable in this instance. However, XPS was unable to detect Co on the anode surface. Ni was not analyzed in XPS due to overlap of the Ni 2p peaks with Fluorine Auger peaks. The ToF-SIMS and XPS analysis thus complemented each other in providing a more complete analysis of the SEI.

6.3.4. Phenomenological Analysis of Electrochemical Degradation

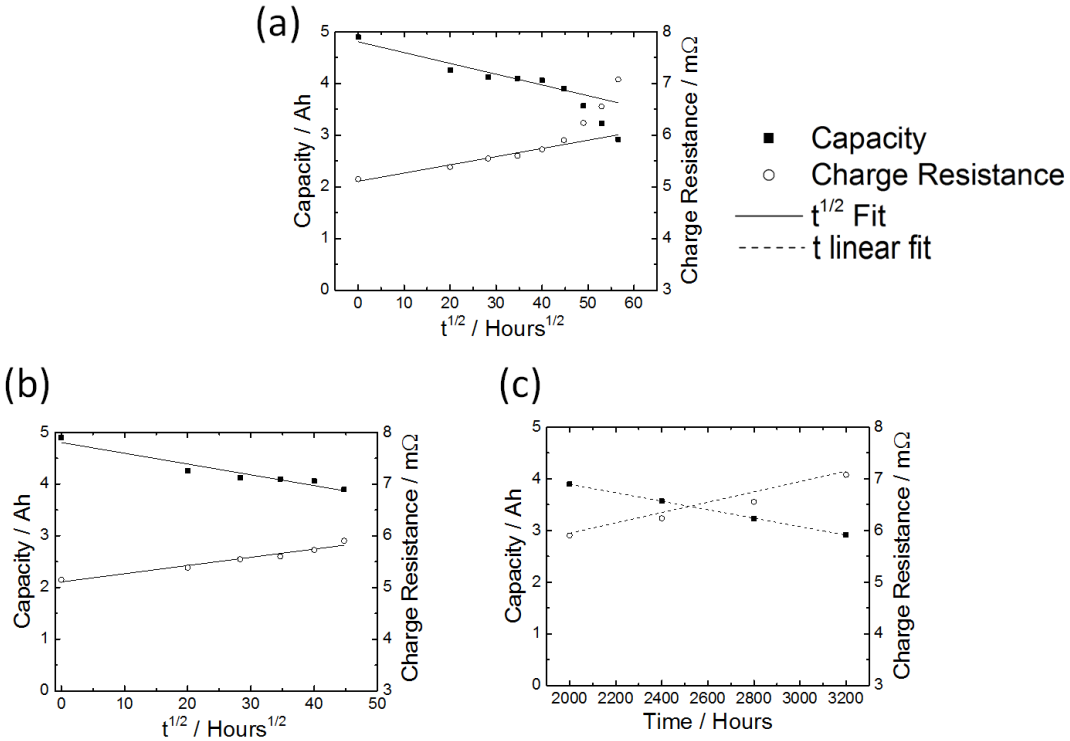

Figure 32. Capacity fade over time can be divided into two regimes: first the capacity fade is dominated by loss of lithium inventory in the SEI in anode; later the capacity fade is dominated by the material loss from cathode. The difference in mechanism is represented by plotting losses as a function of $t^{1/2}$ in the beginning of aging (b) and as a function of t in the latter stages of aging (c).

In order to understand the capacity fade mechanism, charge resistance and capacity of the cell with aging is re-plotted in Fig. 8. In previous reports on capacity fade, mainly SEI layer growth and the corresponding loss of cyclable lithium are implicated in cell degradation with aging and cycling [128-130]. This degradation mode is often described by a parabolic growth of the SEI layer and follows a linear decrease of capacity with the square root of time [131]. In Figure 32a, capacity and resistance are plotted against the square root of aging time. Both capacity and resistance display parabolic decay/growth in the beginning and are consistent with previous degradation studies [130-132]. However, after 2000 hours, both capacity and resistance deviate from the trend, suggesting a different

degradation mechanism. ToF-SIMS and XPS results showed surface layer growth on both the anode and cathode. As SEI layer growth continued in the beginning of aging, more Li was lost irreversibly in the anode and contributed to capacity loss. The storage conditions used in this study (75 °C and 90% SOC) are extremely conducive to solvent reduction/SEI growth on anode. Hence, the degradation through this mechanism is accelerated.

The resistance increase and capacity fade in the later stages of aging follows a linear trend with time. This change in behavior indicates a difference in degradation mechanism compared to the earlier stage where Li loss in the SEI dominated degradation behavior. This varied mechanism may be explained by the material loss from the positive electrode as evidenced by the transition metal depletion shown in the SIMS results. The rate of material loss seems to have been accelerated after 1600 hours. Furthermore, TEM results show that the positive electrode surface loses its crystallinity. This may be explained by the active material loss and formation of a surface layer on the cathode. Active material loss from the positive electrode may also explain the increased internal resistance and diffusional resistance as seen in EIS.

6.4. Conclusions

The sharp decline in the first 400 hours at 75 °C is most likely due to the formation of a surface layer on the anode—the solid electrolyte interphase (SEI). The passivating SEI layer formation leads to irreversible lithium consumption resulting in decreased cell capacity, and is often the dominant mode of degradation in cells [129,130,133]. The high temperature used in this aging study as well as the high state-of-charge at

storage contribute directly to increased degradation and capacity fade [133,134]. After 400 hours, the rate of capacity fade decreases and the cell performances stabilizes. As the SEI layer is formed, the rate of solvent decomposition to form additional layer and subsequent lithium loss decreases. The increased capacity fade after 2000 hours is likely due to a second mechanism or mechanisms along with SEI formation on anode. Previous reports have indicated this sort of two regions for capacity fade [129,135]. Material loss due to transition metal dissolution is an important degradation mechanism in cells containing transition metal oxides in positive electrodes [126,133,136]. The loss mechanism related to this different slope after 2000 hours may be related to material loss from the positive electrodes.

In this study, cell resistance increase and capacity fade occurring in commercial prismatic cells were studied using electrochemical and post-mortem analysis. Accelerated calendar aging was achieved by storing cells at a high temperature of 75 °C. Cell resistance and capacity was mainly influenced by the limitations occurring in the negative electrode due to SEI layer growth in the beginning stages of aging. Loss of cyclable lithium in the SEI layer contributed to increased cell resistance and capacity fade. In later stages of aging, changes occurring in the positive electrode became the dominant mode of degradation. Active material dissolution and surface layer formation of cathode contributed to an increased rate of cell performance degradation with aging. It may be possible to limit capacity and power fade in these types of cells by addressing the mode by which degradation proceeds: namely SEI layer growth and cathode active material degradation. It may be possible to limit the solvent reduction and SEI growth on the negative electrode by adding some SEI-forming additives in the electrolyte solution [137].

Furthermore, mechanisms of performance degradation due to active material dissolution and surface layer formation on NCM positive electrodes need further investigation to understand how this occurs and delay the accelerated decline in power and capacity.

Chapter 7. XPS of Fluorinated Sulfonimide SEI for Li-S

7.1. Introduction

S is a high capacity cathode material, particularly in terms of specific capacity. However, S is also incompatible with standard electrolytes due to the reactivity of Li_xS polysulfide compounds with carbonates [138,139]. Polysulfides are very soluble in many organic electrolytes. Also, most S cathodes are in their unlithiated state, and are generally constructed with a Li metal anode [4]. Metallic Li has not been commercialized in any large scale rechargeable battery due to Li dendrite growth in standard Li electrolyte. Thus a new electrolyte appears to be the most sensible next step in developing S cathodes.

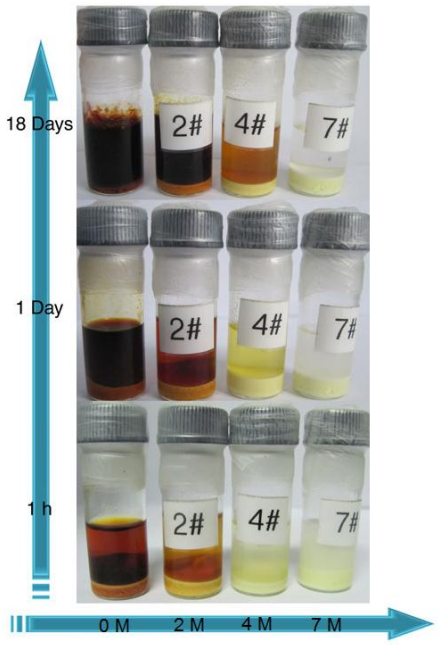

Figure 33. Color changes over time with 4 different concentrations of LiTFSI in DIOX/DME with Li_2S_8 [140].

Lithium bis(trifluoromethane)sulfonimide (LiTFSI) in 1,3-dioxolane / 1,2-dimethoxyethane (DIOX/DME) has become a standard electrolyte for Li-S batteries in recent years [141,142]. LiTFSI is a well studied and favored salt, and the combination has a

relatively low boiling point, but has low viscosity and good Li^+ transport. Also, high concentration electrolyte has shown to decrease the solubility of polysulfides in the electrolyte and thereby improving the cycle life of Li-S cells (Figure 33). LiFSI has a similar structure but has a higher Li^+ conductivity, very close to that of $LiPF_6$ [143]. The results were very encouraging, showing high cycle stability for Li-S cells. This chapter is dedicated to the XPS analysis of the SEI films formed by these salt/solvent combinations in order to better understand how LiFSI improves the cycle stability of Li-S cells.

7.2. Experimental Methods

XPS analysis was done using the Thermo K-Alpha (Al K_α source). The samples were transferred from a an Ar glove box atmosphere in a vacuum sealed sample transfer chamber to prevent any air exosure. Analysis was performed on Avantage software using mixed linear-Shirley "smart" backgrounds and Gaussian peaks. S2p peaks were fitted with doublets of 2p3/2 and 2p1/2 with peak separation of 1-1.2 eV, peak height of 2/1 ratio, and identical FWHM. Other experimental details on preparation and analysis are available elsewhere [90].

7.3. Results and Discussion

5M LiFSI in DIOX/DME was shown to be superior to 5M LiTFSI in DIOX/DME in preventing polysulfide dissolution at 60 °C based on visual observation, and constant current cycling at 60 °C (Figure 34) showed higher capacity. On the other hand, LiFSI in only DME showed lower capacity than in DIOX/DME, but higher cycle stability. 3M LiFSI in DME showed even better cycle stability, although again, at the expense of

capacity. CV scans at 2mV/s between 1.5-3 V at 60 °C for LiFSI in DME showed two reduction peaks at ~1.6 V and ~2.2 V, whereas the same scans at 25 °C or with LiTFSI in DIOX/DME did not show any reduction peaks.

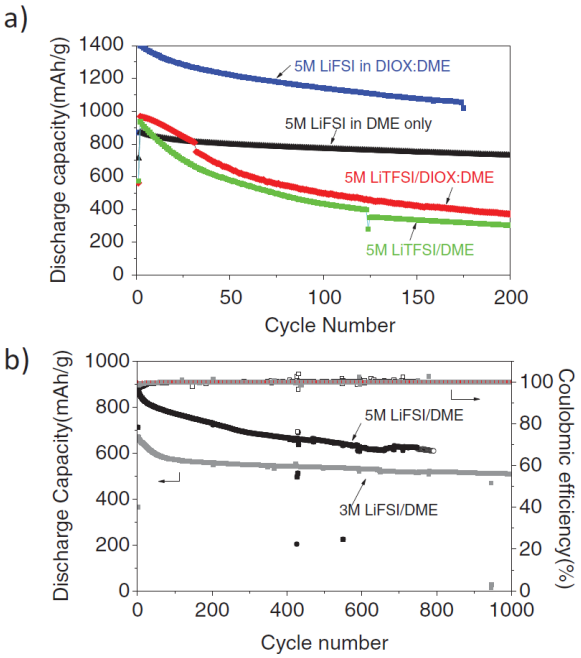

Figure 34. Constant current cycling at C/5 at 60 °C between 1.2-3V (a) comparing LiTFSI and LiFSI in DIOX:DME (1:1 by vol) or just DME and (b) different concentrations of LiFSI in DME [144].

Based on this evidence, it was conjectured that LiFSI decomposes to create an SEI on the sulfur cathodes through a reductive process which then prevents any further polysulfide dissolution. The incredible cycle stability for C/5 cycling for up to 1000 cycles at 60 °C indicates an extremely effective barrier against polysulfide dissolution. On the other hand, the lower initial capacity seems to suggest that some of the sulfur is lost initially before the SEI is formed. Furthermore, the cycling is more stable in pure DME solvent rather than the DIOX/DME combination, indicating that the process may be linked to an interaction between DME and LiFSI.

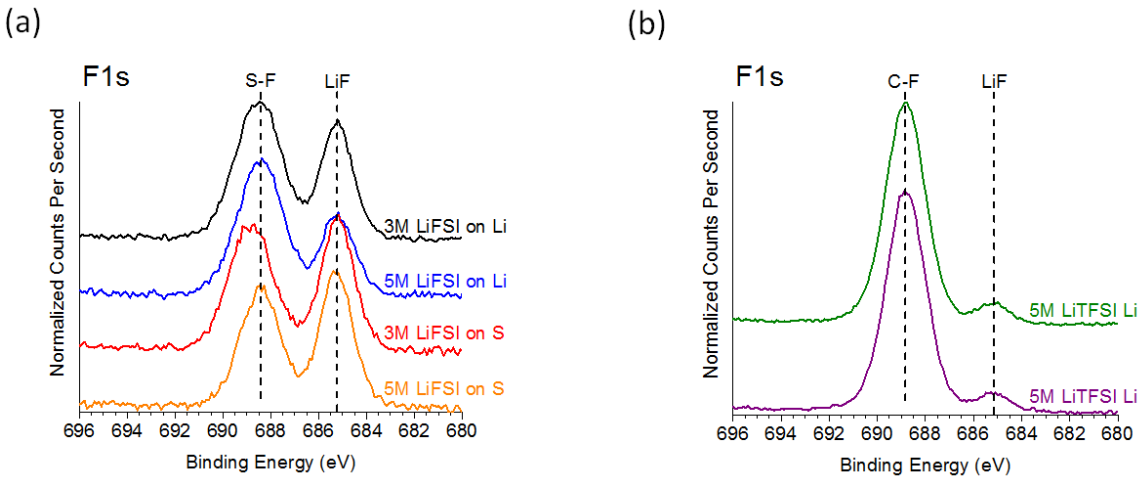

Figure 35. XPS scans of F1s spectra on the Li anode and S cathode surfaces, after cycling at different concentrations of (a) LiFSI and (b) LiTFSI.

Table 8. Atomic compositions of F1s spectra on Li anode and S cathode surfaces for after cycling in different concentrations of (a) LiFSI and (b) LiTFSI.

(a)

Atomic Composition		
	F1s S-F	F1s LiF
Approx. F1s BE	688.5 eV	685.2 eV
3M LiFSI on Li	4.5 %	2.8 %
5M LiFSI on Li	4.6 %	2.3 %
3M LiFSI on S	3.8 %	3.4 %
5M LiFSI on S	3.5 %	3.6 %

(b)

Atomic Composition		
	F1s C-F	F1s LiF
Approx. F1s BE	688.8 eV	685.2 eV
5M LiTFSI on Li	12.6 %	1.1 %
5M LiTFSI on S	15.3 %	1.3 %

XPS was thus used to characterize the SEI layer formed by this decomposition process. The spectra for all the samples were corrected for charge shifting by aligning the LiF peak at 685.2 eV. Figure 35 shows the F1s spectra of the cycled electrodes and atomic composition of the peaks are shown in Table 8. Despite LiFSI having a lower F content, it decomposed more readily to form LiF, as evidenced by the high LiF composition and low S-F composition. Higher LiFSI content also increased the amount of LiF formed. Relatively speaking, S cathodes had more LiF and less S-F than Li anodes, suggesting that more LiFSI decomposition occurred on the cathodes. LiTFSI meanwhile, showed similar compositions on both anode and cathode.

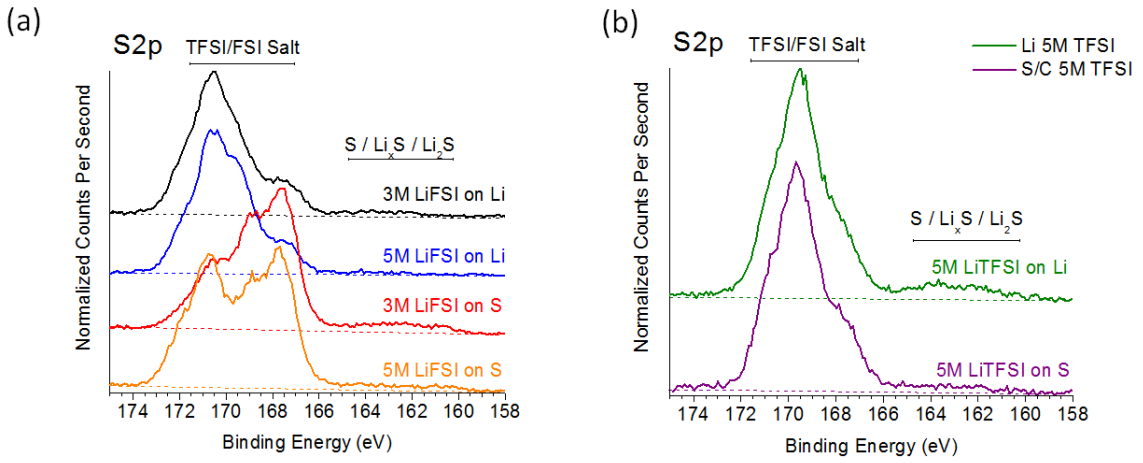

Figure 36. XPS scans of S2p spectra on the Li anode and S cathode surfaces, after cycling at different concentrations of (a) LiFSI and (b) LiTFSI.

Table 9. Atomic compositions of S2p spectra on Li anode and S cathode surfaces for after cycling in different concentrations of (a) LiFSI and (b) LiTFSI.

(a)

Atomic Composition			
	S2p FSI	S2p A	S2p B
$S2p_{3/2}$ BE	170.7 eV	169.3 eV	167.4 eV
3M LiFSI on Li	5.3 %	3.3 %	1.8 %
5M LiFSI on Li	4.9 %	5.8 %	1.9 %
3M LiFSI on S	2.7 %	2.9 %	9.8 %
5M LiFSI on S	6.1 %	2.1 %	7.9 %

(b)

Atomic Composition		
	S2p TFSI	S2p C
$S2p_{3/2}$ BE	169.5 eV	167.7 eV
5M LiTFSI on Li	7.7 %	2.6 %
5M LiTFSI on S	6.3 %	2.4 %

The S2p scans (Figure 36) show very weak $S/Li_xS/Li_2S$ peaks, indicating the effectiveness of the high concentration electrolytes in preventing polysulfide dissolution. Qualitatively, it appears as though the quantities of these compounds is in the order of 3M LiFSI > 5M LiFSI > 5M LiTFSI on the S cathodes, and 5M LiTFSI > 3M LiFSI ≈ 5M LIFSI on the Li anodes. This suggests that LiFSI passivates polysulfide reduction at the anode better than LiTFSI. However, given the extremely small signal to noise ratio, true quantitative analysis is not reliable. The detailed fits for the S2p spectra are available in Figure 87 of Appendix E.

The S2p TFSI/FSI salt peaks are informative of the decomposition, especially in conjunction to the N1s peaks. Table 9 shows the atomic compositions of the chemical

states identified. At minimum, 3 doublets were necessary to fit the LiFSI S2p spectra, while the LiTFSI S2p spectra only required 2. Based on reference samples (Table 4), the highest BE peaks were identified to be that of the undecomposed salts, while the chemical states for the decomposed salts were arbitrarily labeled A, B, and C. 5M solutions showed higher compositions of salt on the S cathodes, while there was no significant difference on the Li side. While LiTFSI showed similar quantities of decomposed salt on both the anode and cathode, LiFSI had more decomposed salt on the cathode, in agreement with the F1s spectra. Furthermore, the S cathodes had higher compositions of B, while the Li anode had higher compositions of A. The S cathode cycled in 5M LiFSI also has an inordinately high LiFSI S composition compared to the F1s spectrum.

The N1s spectra are shown in Figure 37, and the atomic compositions in Table 10. The peak at 400.2 eV was assigned to LiFSI because the F1s and S2p peaks were shifted in the positive BE direction by 0.6 and 0.5 eV respectively, despite charge shift correction using LiF. Again, two decomposition products were observed for LiFSI, while only one was observed for LiTFSI.

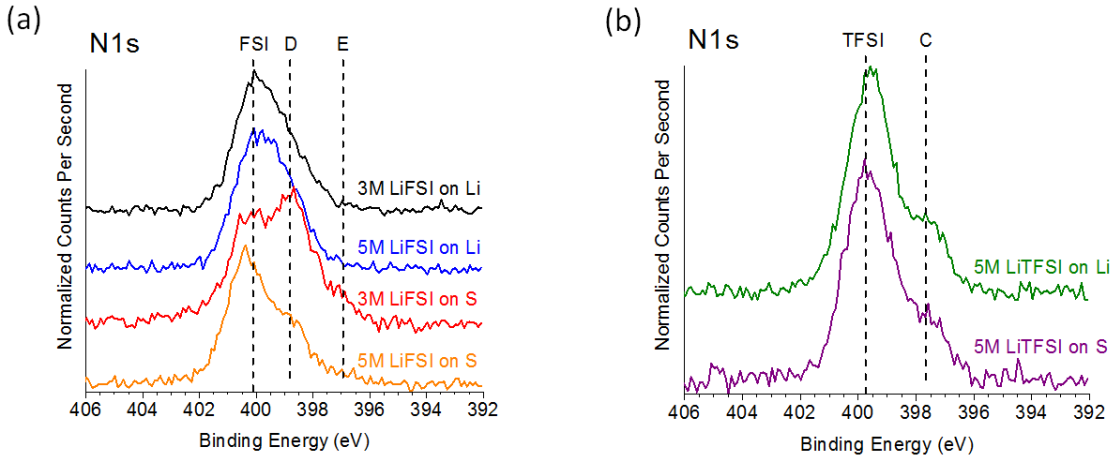

Figure 37. XPS scans of N1s spectra on the Li anode and S cathode surfaces, after cycling at different concentrations of (a) LiFSI and (b) LiTFSI.

Table 10. Atomic compositions of N1s spectra on Li anode and S cathode surfaces for after cycling in different concentrations of (a) LiFSI and (b) LiTFSI.

(a)

Atomic Composition			
	FSI	D	E
N1s BE	400.2 eV	398.8 eV	396.9 eV
3M LiFSI on Li	2.4 %	1.1 %	
5M LiFSI on Li	2.8 %	1.6 %	
3M LiFSI on S	2.3 %	2.6 %	0.6 %
5M LiFSI on S	3.4 %	1.4 %	0.3 %

(b)

Atomic Composition		
	TFSI	C
N1s BE	399.6 eV	397.7 eV
5M LiTFSI on Li	3.4 %	1.0 %
5M LiTFSI on S	3.2 %	1.0 %

The composition of the LiTFSI decomposition product was similar for on the Li and S, just as in the F1s and S2p spectra. This indicates a simple decomposition mechanism resulting in LiF and another compound. Thus this peak was labeled C, as the chemical state is most likely strongly associated with the chemical state observed in the S2p spectrum.

On the other hand, the relative compositions of the LiFSI decomposition products did not follow the trend observed in the S2p spectra, indicating a more complicated decomposition mechanism. The E peak, although very weak, only appeared in the S cathodes. As with the S2p spectra, this indicates a difference in the decomposition products on the Li anode and the S cathode. Also, the 3M LiFSI on S has more of

decomposition product D compared to LiFSI, while 5M LiFSI on S has more LiFSI compared to its decomposition products. This also agrees with the S2p spectra, indicating that for the S cathode cycled in 5M LiFSI, the N and S 'FSI' chemical state compositions are higher than the F 'FSI' chemical state composition. Also, in both cases, the BE appears to be shifting in the negative direction, indicating greater electron density in the N and S of the decomposition products.

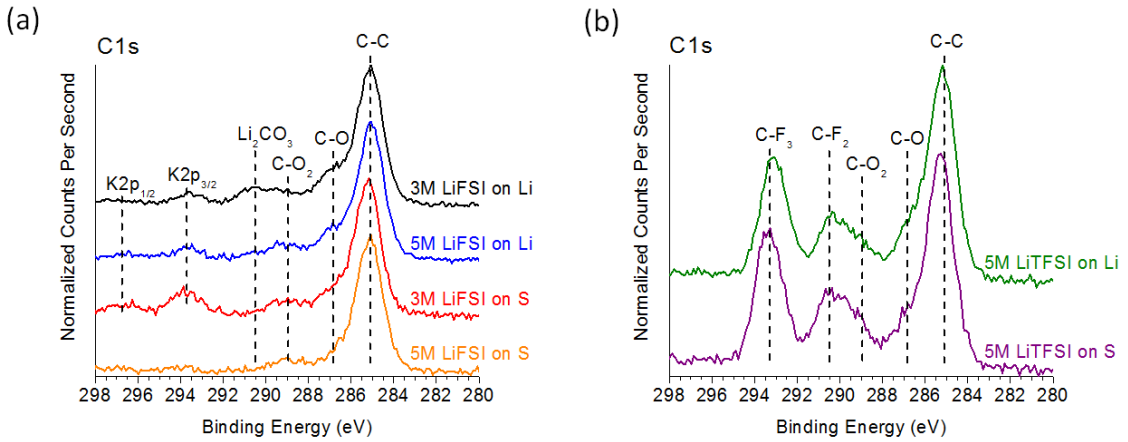

Figure 38. XPS scans of C1s spectra on the Li anode and S cathode surfaces, after cycling at different concentrations of (a) LiFSI and (b) LiTFSI.

Table 11. Atomic compositions of C1s spectra on Li anode and S cathode surfaces for after cycling in different concentrations of (a) LiFSI and (b) LiTFSI.

(a)

Atomic Composition				
	C1s Li_2CO_3	C1s $C-O_2$	C1s C-O	C1s C-C
C1s BE	290.5 eV	289.1 eV	286.9 eV	285.1 eV
3F-Li	0.9 %	0.8 %	2.2 %	8.6 %
5F-Li		1.0 %	1.9 %	8.3 %
3F-S		1.0 %	1.5 %	8.0 %
5F-S		1.0 %	1.3 %	9.5 %

(b)

Atomic Composition					
	C1s $C-F_3$	C1s $C-F_2$	C1s $C-O_2$	C1s C-O	C1s C-C
C1s BE	293.1 eV	290.4 eV	289 eV	286.8 eV	285.1 eV
5T-Li	4.5 %	2.3 %	1.3 %	1.7 %	7.9 %
5T-S	5.2 %	2.7 %	1.8 %	1.6 %	8.2 %

Finally, the C1s spectra and compositions are shown in Figure 38 and Table 11. The peak assignments are based on what types of compounds were expected to be seen. The peak at 286.9 eV was assigned C-O as DME decomposition products with ether linkages are expected to have a peak in this region. The $C-F_3$ chemical state is known

from the reference sample, but C-F_2 at 290.4 eV is conjectured from PVDF and the assumption that such a chemical state will remain after LiTFSI decomposes to form LiF. Of all the LiFSI cycled samples, only the Li anode from the 3M LiFSI electrolyte shows a peak at 290.5 eV. Thus, it is assumed that this is due to extensive reduction of organic SEI components by Li, producing Li_2CO_3.

For all samples, the dominant C1s peak was the hydrocarbon C-C peak at 285.1 eV. This suggests the decomposition of DME (the only hydrocarbon available for the Li side) which involves the removal of O.

7.4. Conclusions

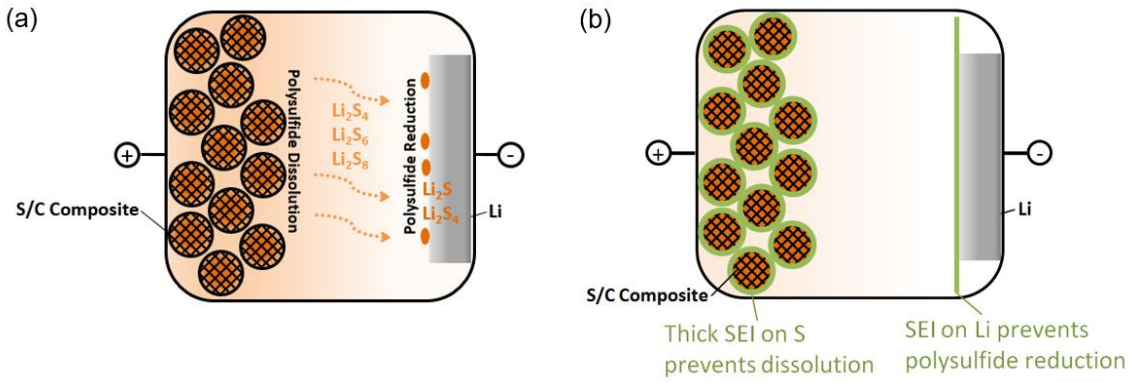

Figure 39. Schematic representation of (a) polysulfide dissolution from cathode and reduction on anode and (b) inhibition of the process by LiFSI/DME decomposed SEI layer.

Based on XPS analysis, the decomposition of DME appears to form hydrocarbon organic material and C-O_2 / C-O_3 groups. LiTFSI decomposes to form LiF, but the rate of this reaction is very slow, even at 60 °C. LiFSI, on the other hand, decomposes to form 2 distinct chemical states of N and two distinct chemical states of S. LiFSI passivated polysulfide reduction on the Li anode better than LiTFSI, which agrees with the more homogeneous Li plating/deplating observed electrochemically and via SEM [90,145]. The

greater extent of decomposition on the cathode also resulted in a thick SEI which mitigated the dissolution of polysulfides. To understand the decomposition mechanism and the molecular structure of the products which so effectively prevent polysulfide dissolution while allowing Li transport, however, further studies are necessary. FTIR and Raman are effective means by which functional groups can be identified, and NMR can identify neighboring atoms. Mass spectroscopy could also be useful by identifying ion fragments of the decomposition products. All these analysis methods would complement the information gathered by XPS, and would help to further understand how LiFSI passivates the S and Li electrodes.

Chapter 8. Introduction to Phosphorus Anodes

8.1. Allotropes of Phosphorus

Table 12. Allotropes of Phosphorus [146]

Phosphorus Phase	Crystal System	Space Group	Density (g/cm^3)	Electrical Resistivity (Ohm-cm)	Volume Expansion to Li_3P
γ-White	Unknown				*
β-White	Triclinic	P -1			*
α-White [147]	Cubic	I -4 3 m	1.828	10^{11}	214%
Amorphous Red [148,149]	N/A	N/A	2.16	10^{14}	253%
Hittorf's (Violet) [150]	Monoclinic	P 2/c	2.34		274%
Orthorhombic Black [151]	Orthorhombic	C m c a	2.69	~0.7	315%
Rhombohedral Black	Trigonal	R 3 m			*
Simple Cubic Black	Cubic	P m 3 m			*
Simple Hexagonal	Hexagonal	P 6/m m m			*
Li_3P	Hexagonal	P 6_3/m m c	1.43		N/A

* Not stable in room temperature and atmospheric pressure.

Phosphorus exists in a variety of allotropes (see Table 12) which can largely be classified into white, red, or black phosphorus. White phosphorus, which has the lowest density, exists as tetragonal molecules of P_4, has a very low melting point (44 °C) and boiling point (280 °C), and is soluble in many nonpolar solvents [146]. However, white phosphorus reacts with water or moisture to produce phosphine gas, and has an appreciable vapor pressure even at low temperatures. Phosphine is a dangerous

neurotoxin which is toxic at ppm levels, and thus white phosphorus is avoided in industry and academia.

Red phosphorus is made of chains of phosphorus atoms, and is stable in air. White phosphorus is converted to red phosphorus when heated above 250 °C, and in contrast to white phosphorus, red phosphorus only begins to vaporize appreciably above 400 °C [152]. At 600 °C red phosphorus sublimates at atmospheric pressure and melts at high pressure (in an inert gas) [153]. Red phosphorus also has multiple crystalline allotropes which are not well understood. Monoclinic Hittorf's phosphorus is one such allotrope which has been studied due to its early discovery [154]. Other crystallized forms of red phosphorus are also often called Hittorf's phosphorus.

Orthorhombic black phosphorus also sublimates at 600 °C and is insoluble in organic solvents. Without the use of a catalyst, it is very difficult to produce, requires extremely high pressures (Figure 40). However, it has a layered structure, and these layers can be exfoliated similar to graphene. This, combined with its tunable direct bandgap (depending on the number of layers) has brought renewed interest in black phosphorus for electronic applications in recent years [155,156]. Although black phosphorus is technically the most thermodynamically stable form of phosphorus, its surface unfortunately reacts with humidity and oxygen. For bulk black phosphorus, this appears not to be an issue, but exfoliated black phosphorus has been reported to decompose in a matter of days [157]. The other allotropes of black phosphorus are only stable at extremely high pressures (Figure 2), with hexagonal black phosphorus only forming at >100 GPa [158].

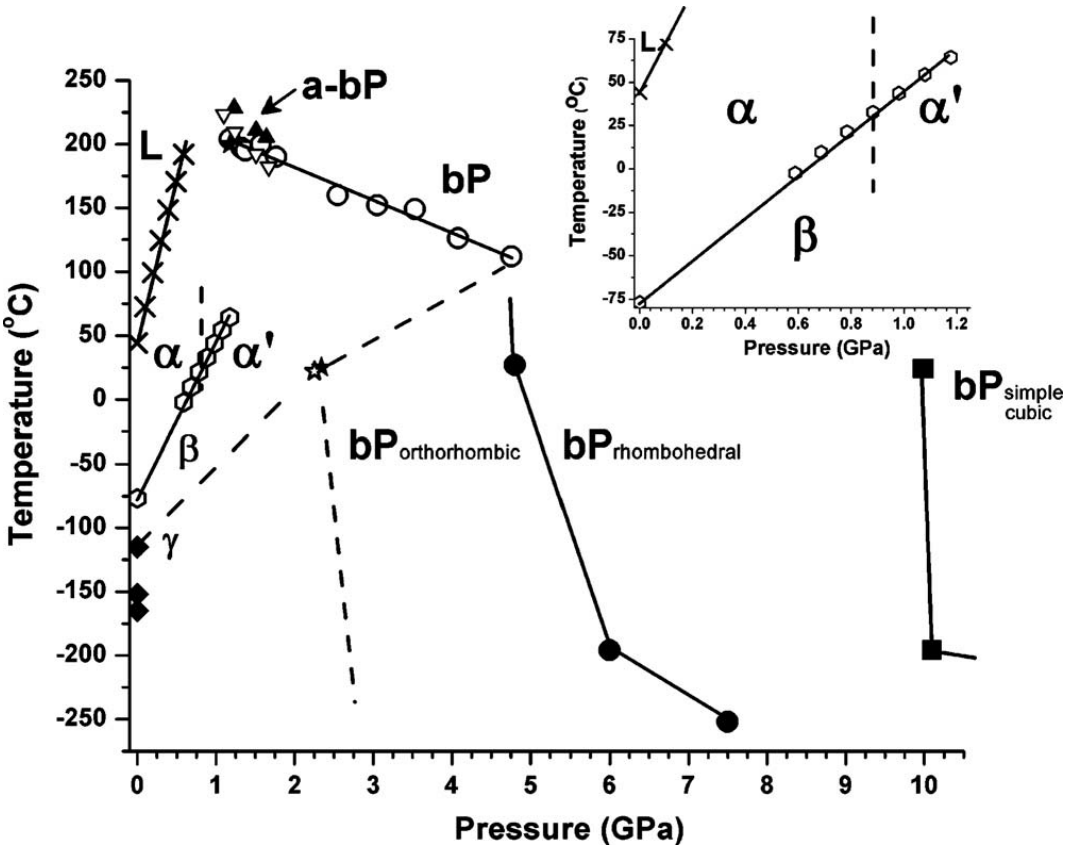

Figure 40. Phase diagram of white and black phosphorus phases [159].

Elemental phosphorus is produced from phosphate ore by heating the ore with a reducing agent, thus forming white phosphorus [153]. This vapor is then deposited in water, and is converted to the more inert red phosphorus by heating to a temperature of 250 °C. Black phosphorus can be produced from white phosphorus vapor by the use of a AuSn or Bi catalyst [160,161]. Ball milling has also been shown to convert amorphous red phosphorus to orthorhombic black phosphorus [162].

8.2. Phosphorus as a Li-ion Anode

Phosphorus is an interesting and relatively unexplored material as a Li-ion battery anode. Its theoretical volumetric capacity is similar to that of Si, and its theoretical

specific capacity is also higher than any element other than Si and Li. Furthermore, it is also earth abundant (Figure 1) [4,5]. Also, the electrochemical reaction between P and Li occurs at a much higher potential relative to Li (0.6 ~ 1.2 V) than Si (0.05 ~ 0.5 V) or C (0.05 ~ 0.25 V). Although this implies that the overall energy density of the battery will be reduced, it also comes with some advantages. An aluminum current collector can be used instead of copper to reduce the cost since aluminum begins lithiation ~ 0.27 V. Also, a phosphorus anode can be operated without bringing the potential close to 0 V, thereby eliminating the low temperature hazard of dendrite formation.

Considering the synthesis routes available, none of the allotropes of phosphorus appear to be prohibitively expensive at a fundamental level. However, comparisons can be made from their physical properties. Black phosphorus is thought to have good Li transport [163,164], and Li_3P has been shown to have good Li transport experimentally (10^{-3} S/cm) [165], although this may or may not be relevant depending on the intermediate phases formed in the electrochemical lithiation and delithiation of phosphorus. Black phosphorus is also by far the most electrically conductive of the three allotropes, and may be the most kinetically favorable. However, black phosphorus has the highest density of the three allotropes, meaning that it undergoes the greatest volume expansion. Whereas α-white phosphorus theoretically only expands to 214% of the original volume, orthorhombic black phosphorus expands to 315%. Thus SEI growth and particle fracturing may be exacerbated in the case of black phosphorus, nullifying its intrinsic kinetic advantages.

Unfortunately, phosphorus and lithium phosphides are bad electrical conductors for an electrode material, and therefore require a nanoscale conductive matrix. Li_3P and the white allotrope of phosphorus are also known to also be extremely dangerous as they

form phosphine gas when exposed to moisture. This is especially problematic for consumer applications, as phosphine gas is a neurotoxin, dangerous at ppm levels. Even so, the advantages and unique characteristics of phosphorus make it an interesting material to investigate as a Li-ion battery anode.

In the past, several studies have investigated the construction of P-C composites for Li-ion battery anodes. Initial studies hypothesized that black phosphorus was a good anode material due to its layered structure [162]. Researchers imagined that an intercalation mechanism could possibly occur to allow for good Li transport within the material [166]. However, more recent studies suggest that in some cases, the reversibility might have been due to phosphorus' reaction with the copper current collector, and that black phosphorus should not normally have significant reversible capacity [167]. In contrast to this suggestion, phosphorus ball milled with carbon has been experimentally shown to have extremely high reversible capacity up to 100 cycles [168]. Park et al. showed that black phosphorus could be made by ball milling red phosphorous for extended periods of time [169]. One study by Qian et al. showed particularly high capacity, rate capability, and stability of ball-milled (with carbon) phosphorus for 100 cycles with the capacity of 1750 mAh/g of phosphorus at a current density of up to 4000 mA/g [168]. The good rate capability of this material suggests that the phosphorus and carbon become closely intermeshed after extended periods of ball milling. The Raman spectrum of the material shows a slight shift in the D-band of the carbon material, which was also observed for phosphorus deposited on a porous carbon material via vapor deposition [170]. This may suggest close bonding between the phosphorus and carbon atoms at the edge plane, resulting in excellent electrical contact. A more recent study by Sun et al. utilizing Raman,

XPS, and ab initio DFT simulation suggests that, in the case of ball milling, this bonding may occur between the edge planes of graphite and black phosphorus [171]. Raman spectra of ball milled samples showed a new broad peak in the 600-800 cm^{-1} range which appears when phosphorus is ball milled with graphite, but not when it is ball milled with C60 or carbon black (which have no edge planes accessible at the surface of the carbon particles). Similar trends were found through XPS, although the data is inconclusive due to significant peak overlap. Also, the phosphorus ball milled with graphite was found to have a higher first cycle coulombic efficiency (CE) than phosphorus ball milled with carbon black, C60, or graphene oxide. However, these results could easily be due to the better conductive matrix offered by graphite compared to the other carbons and some deviations of the electrode properties (such as different porosity on the electrode level, different strength, uniformity, etc.).

Interestingly, good reversibility could also be achieved for a Na-ion battery by merely grinding red phosphorus powder with carbon nanotubes by hand for 1 hour [172]. This suggests that good reversibility of phosphorus can be achieved if a nanoscale conductive matrix can be created. Indeed, the ball milled carbon studies also utilize 30 wt% or more carbon to improve the conductivity. However, there are still relatively few studies, and many details associated with the fabrication, operation, and failure modes of the electrode have yet to be studied or understood. Furthermore, the stability of these electrodes have been generally inferior compared to silicon electrodes, despite their higher operative voltage with respect to lithium. The impact of the binder and the details of the interactions between phosphorous and various electrolyte components have not been studied yet.

In constructing a Li-ion battery anode with phosphorus, its reactivity must first be kept in mind. Red phosphorus and black phosphorus are considered stable phases in ambient conditions, but will immediately begin to react, and completely decompose in the span of several days [156,173,174]. Thus slurry casting must be done in a water deprived or oxygen deprived environment in an organic solvent. Chemical bonding can also be expected between phosphorus and many of the battery components, as phosphorus was even observed to react with the copper current collector [167]. This suggests that phosphorus may be able to form strong interfacial bonds with the other components (binder, conductive additive, current collector) of the electrode, which should be beneficial so long as it can be limited to the surfaces.

Overall, it is unclear which allotrope of phosphorus might offer the best combination of stability, capacity and rate performance, and if its reactivity could potentially cause issues or advantages when P is used in the Li-ion battery anodes. Therefore the overall purpose of this study is to gain better fundamental understanding of the complex processing-structure-property relationships of phosphorus containing anodes for Li ion batteries and thus contribute to the development of better performing phosphorus anodes.

Chapter 9. P-C Composite via Ball Milling

9.1. Introduction

Ball milling is a useful industrial too for mixing solids and decreasing particle size. Mechanical alloying can also occur, as discussed in Section 3.1. Unfortunately, the particle size inevitably has a large spread, and after a while the rate of particle fracturing and particle agglomeration equilibrates, and results in no further particle size reduction.

For phosphorus, ball milling provides a very simple method for creating a nanocomposite. By repeating the process of fracturing and agglomeration, ball milling can create particles of well intermixed phosphorus and carbon phases. The high pressure also converts the phosphorus to the black phosphorus phase. Combined these two effects have resulted in the most of the best performing phosphorus anodes to date. In this chapter, the mechanism and parameters of ball milling are explored in order to synthesize a well intermeshed P-C composite.

9.2. Methods

Ball milling was performed via either the Across International PQ-N04 Planetary Ball Mill (~350 rpm) or the Mixer Mill 8000M (1100 rpm) in 80 ml jars. 3/8" 440C stainless steel balls were used, and the mass ratio between the grinding media (ball milling balls) and the powder was kept at 20:1 to ensure sufficiently high energy impacts for conversion of phosphorus to the black phosphorus allotrope. The ball milling time and

total quantity of power was varied. The resulting powder was analyzed via LEO 1530 FE-SEM and Oxford Instruments EDS, Panalytical Alpha-1 XRD, and Hitachi HF2000 TEM.

For electrochemical testing, phosphorus was ball milled with Pure Black (~200 nm spherical carbon black), Ausbury Graphite (16 nm spherical carbon black, Asbury Carbon), or CNT (< 8 nm outer diameter, 10-30 μm length, COOH activated, from cheaptubes.com). The powder was then mixed in a slurry with 10 % pure black and 10% polyacrylic acid by weight and cast on a copper electrode. The electrodes were then cycled in 2016 cells in half cell configuration again Li counter electrodes with 1M $LiPF_6$ in EC:DEC:DMC 1:1:1 by vol. electrolyte. Galvanostatic cycling was performed on an Arbin Instruments BT-2000, and the c-rate was calculated based on 2596 mAh/g-P theoretical maximum capacity.

9.3. Results and Discussion

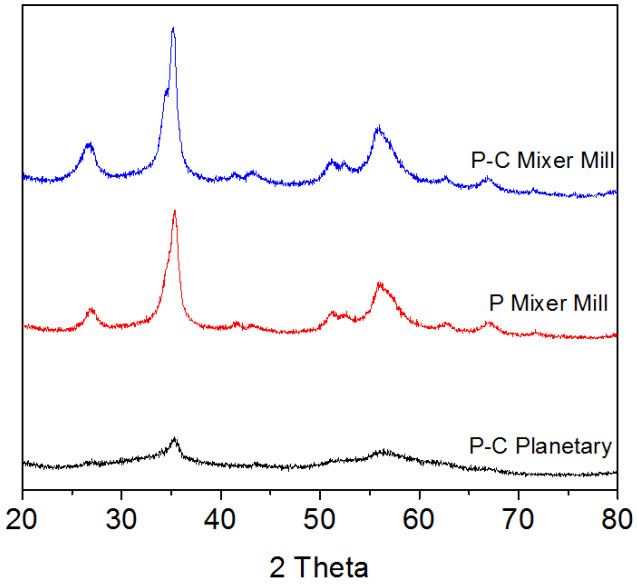

Figure 41. XRD spectra of (black) P-C ball milled in a planetary ball mill in a 7-1.5 weight ratio for 56 hours, (red) phosphorus ball milled in a mixer mill for 1 hr, and (blue) P-C ball milled in mixer mill in a 7-3 weight ratio for 1 hour. Pure black was used as carbon in P-C.

Figure 41 shows the XRD spectra of ball milled commercially available red phosphorus powder with or without pure black (carbon black powder). The Mixer Mill clearly converts the phosphorus material to black phosphorus more effectively. This is most likely due to the higher energy impacts of the Mixer Mill. Whereas the Planetary Ball Mill rotates the jar along one axis, the Mixer Mill is of a type of ball mill also called a "shaker mill". The jar is moved in a figure eight motion at a very high rpm, simultaneously mixing the powder and causing high energy impacts as the ball gets thrown from one end to another. After 1 hr of milling, the Mixer Mill powder has strong XRD peaks corresponding to the black phosphorus phase, whereas the Planetary Mill only shows weak peaks after 56 hours.

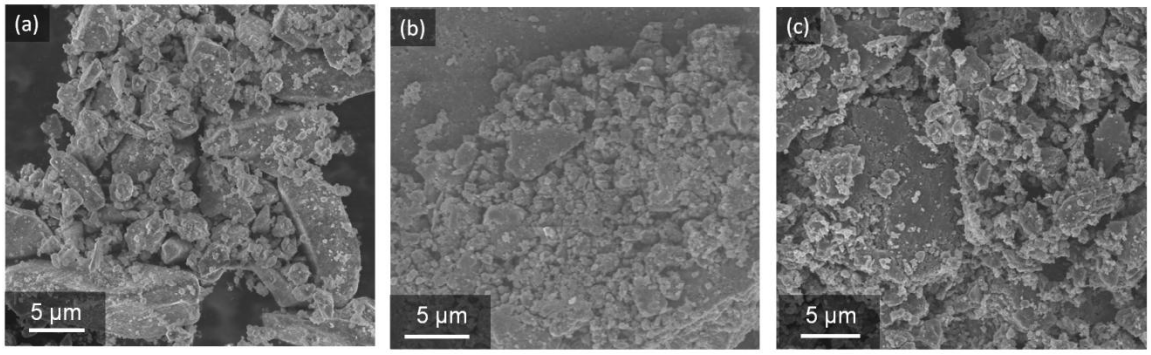

Figure 42. (a) Red phosphorus, (b) black phosphorus made by ball milling red phosphorus for 1 hour in mixer mill, and (c) P-C ball milled in mixer mill in a 6-4 weight ratio for 1 hour.

Figure 42 shows SEM images of phosphorus before and after ball milling, as well as a sample where phosphorus was ball milled with carbon. Whether carbon was added or not, the particles appear to be of a similar size visually to the red phosphorus. However, on closer inspection, it is evident that the larger particles are in fact agglomerates of smaller particles (Figure 42c, left side). This agrees with the established understanding of the mechanism of the ball milling process.

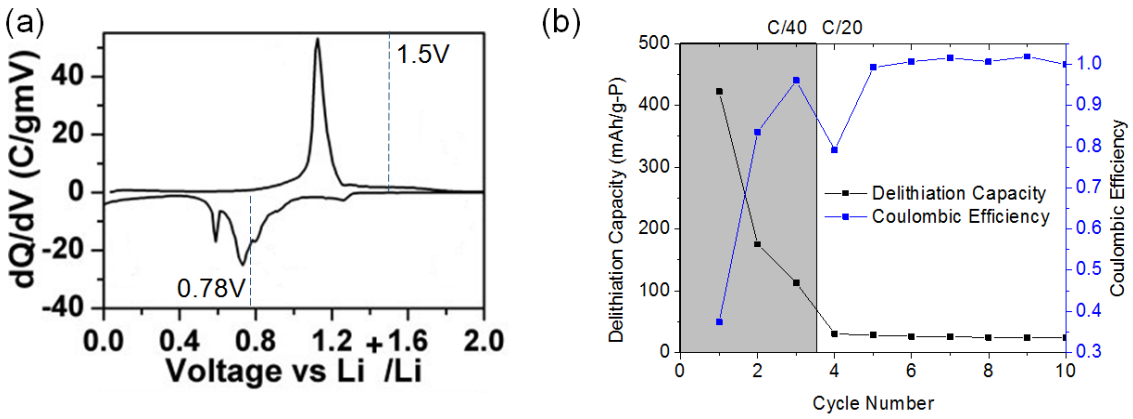

Figure 43. (a) Differential capacity plot from literature [162] showing utilized voltage range and (b) low rate galvanostatic cycling of P-C composite of 8-2 weight ratio ball milled in mixer mill for 1 hour.

Ball milling was then used to ball mill phosphorus-carbon (P-C) composites for electrodes. However, this proved to be a non-trivial problem, most likely due to the low

electrical conductivity of phosphorus. Figure 43 shows the electrochemical stability of a P-C composite of 8:2 P:C weight ratio cast in an electrode and cycled at 0.78-1.5V. Sohn et al. [162] used this severe voltage limit to limit the volume change in the electrode and thereby achieve electrochemical cycle stability at a C/5 rate. However, although an initial C/40 rate was used, the delithiation capacity of the electrode degrades precipitously during the first few cycles.

In order to achieve better cycling, longer ball milling times were attempted. As the P-C composite is ball milled, particles are repeatedly broken apart and agglomerated, gradually decreasing the size of the phosphorus and carbon domains within the composite particles. In essence the particles become better mixed solid mixtures, wherein smaller phosphorus domains present lower electrical resistance. The carbon composition of the phosphorus was also increased in order to further improve the conductivity of the particles.

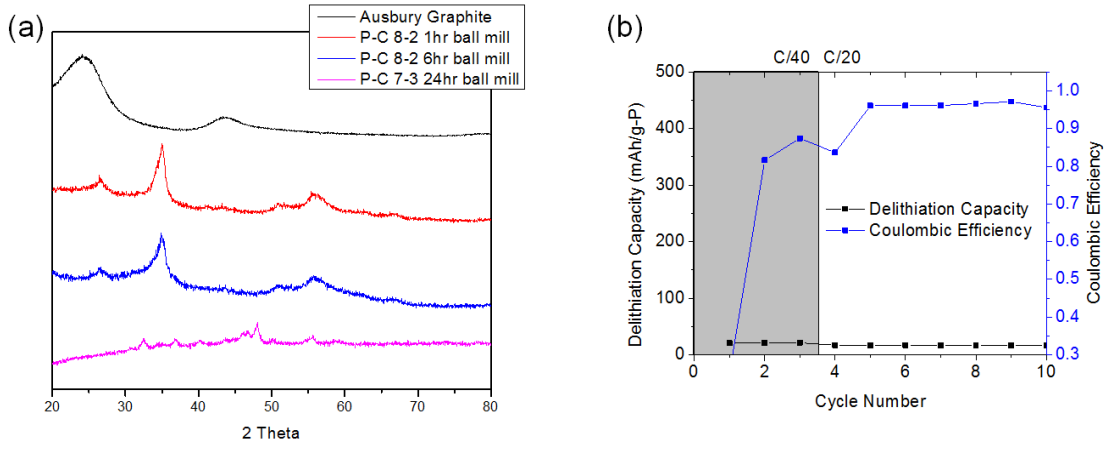

Figure 44. (a) XRD spectra of Ausbury Graphite (carbon black) and P-C composites of various weight ratios ball milled for varying lengths of time in mixer mill. (b) Galvanostatic cycling of P-C (8-2) 6 hour ball milled powder.

Figure 44a shows the XRD analysis of the result of this ball milling experiment. If the phosphorus domains become small enough, the Rietveld effect should cause the phosphorus peaks to become wider. Indeed, the P-C composite ball milled for 6 hours appears to have wider peaks than the P-C composite ball milled for 1 hour. However, the capacity of the electrode surprisingly decreased to an extremely low capacity as a result of the extended ball milling. Furthermore, ball milling the composite for 24 hours resulted in a completely different XRD spectrum.

(a)

Element	Weight %
C	47 %
O	5 %
P	48 %

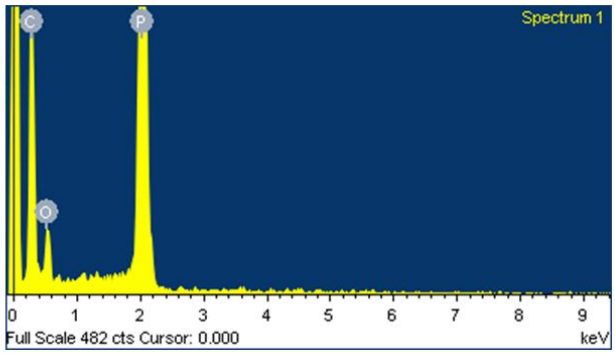

(b)

Element	Weight %
C	3 %
O	< 1 %
P	8 %
Cr	9 %
Fe	51 %
Ni	15 %

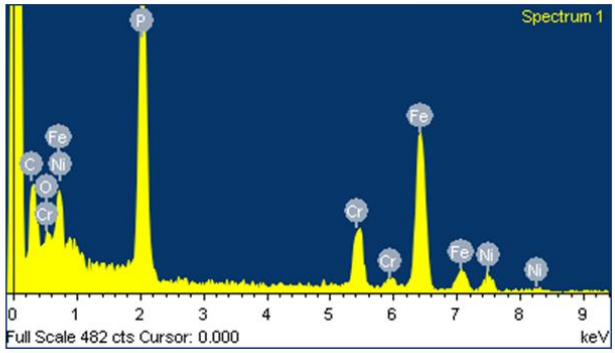

Figure 45. EDS spectra for P-C 7-3 weight ratio composites ball milled for (a) 1 hour and (b) 24 hours with 10 x 3/8" ball milling balls.

Figure 45 shows the EDS spectra of the P-C composites ball milled for 1 hour and 24 hours. Clearly, after 24 hours, the composite is mostly Cr, Fe, and Ni, most likely from the ball milling balls and jar, although the XRD spectrum of this powder only shows

very weak peaks. The large number of ball milling balls appears to have caused excessive impacts between the grinding media which shaved off bits of stainless steel, while also generating heat from friction and possibly causing a reaction with the phosphorus. This could have caused the extremely low capacity for the 6hr ball milled powder shown in Figure 44b. In order to decrease the impacts between ball milling balls, the number of ball milling balls was limited to 3, and the experiments were repeated.

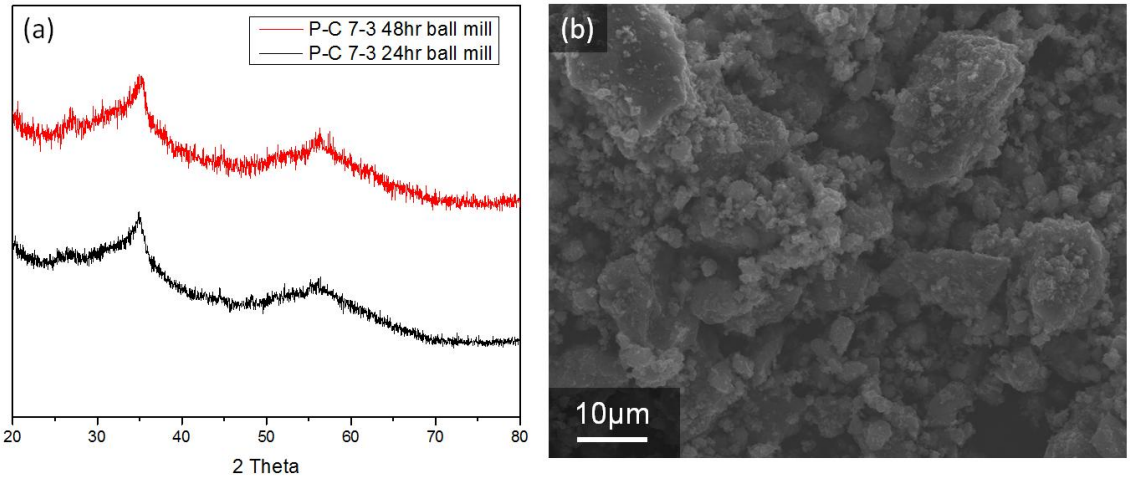

Element	Weight %
C	80.81
O	3.96
Mg	0.06
P	15.12
Fe	0.06

Figure 46. (a) XRD spectra of P-C composites ball milled in mixer mill for extended periods, and (b) SEM image and (c) EDS of the 24 hour balled powder.

Figure 46a shows the XRD spectra of P-C composites ball milled for 24 and 48 hours, showing that the powder is still black phosphorus. Decreasing the number of ball milling balls inside the jars appears to have decreased the heat generation rate sufficiently

to allow the phosphorus to be ground over extended periods of time without causing a reaction with the ball milling media. The EDS in Figure 46c shows trace amounts of Fe however, and thus this may be the optimal ball milling time for this particular loading of ball milling balls and P-C powder. Longer ball milling times may remove more stainless steel from the ball milling balls and jar again.

Most importantly, these black phosphorus powders ball milled for extended periods of time exhibited dramatically higher capacity and cycle life than the previous cells. The data from the electrochemical cycling is presented in the following chapters, where the impacts of the other battery electrode components are investigated.

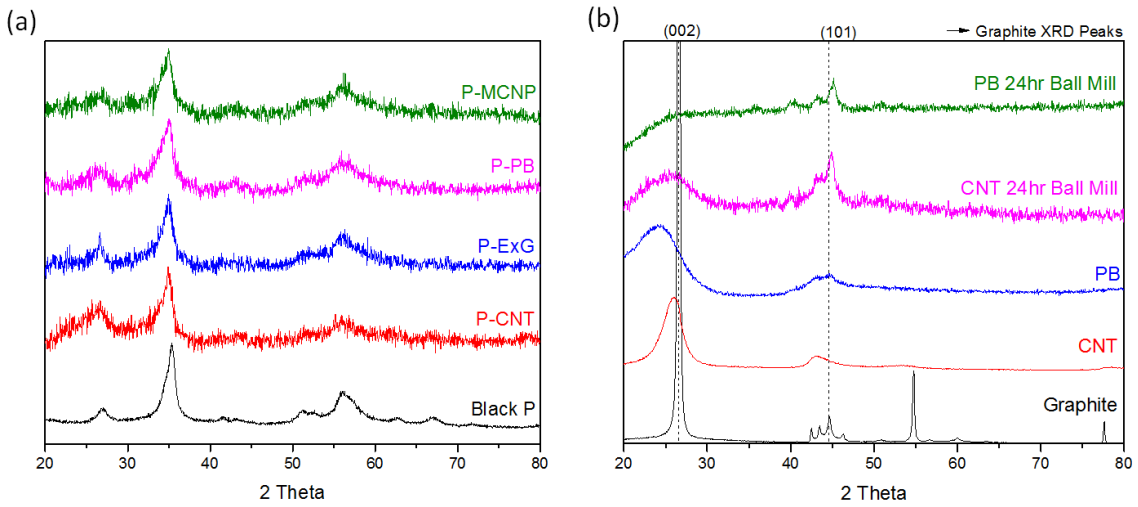

Figure 47. (a) P-C composites ball milled in 7-3 weight ratios with different carbons for 24 hours and a black phosphorus powder ball milled without carbon for 1 hour. (b) XRD spectra of PB and CNTs before and after 24 hours of ball milling, and the XRD spectrum of graphite.

To further understand the mechanism of the optimized ball milling process, phosphorus was ball milled with different types of carbon. Figure 47a shows the XRD spectra of the P-C composite powders with different carbons. In every spectrum, the

black phosphorus peaks dominate, and no clear difference is observable. Thus to study the differences, some of the carbons were ball milled separately, without any phosphorus.

Figure 47b shows the XRD spectra of carbon black and multi-walled carbon nanotubes before and after 24 hours of ball milling. After 24 hours, both powders have virtually the same XRD spectrum suggesting a similar microstructure. Furthermore, this spectrum appears to be very similar to that of graphite, athough several peaks appear to be missing.

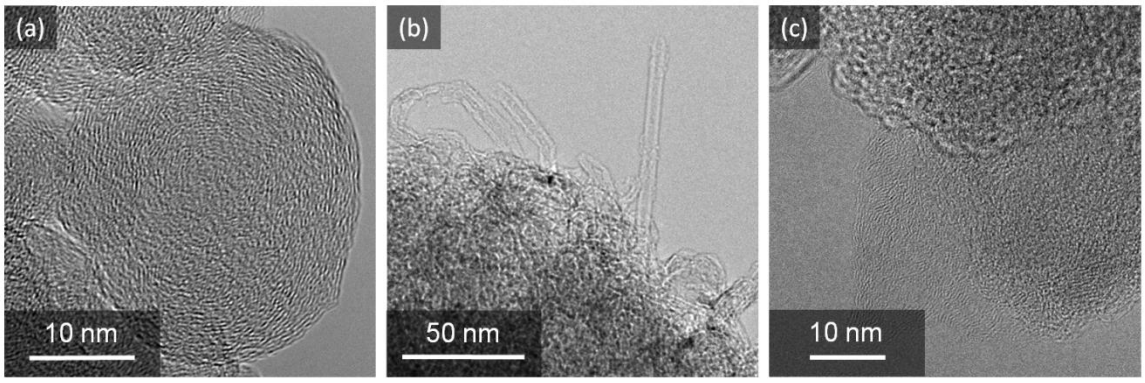

Figure 48. TEM micrographs of (a) carbon black (asbury carbon) (b) CNT and (c) CNT after 24 hour ball mill.

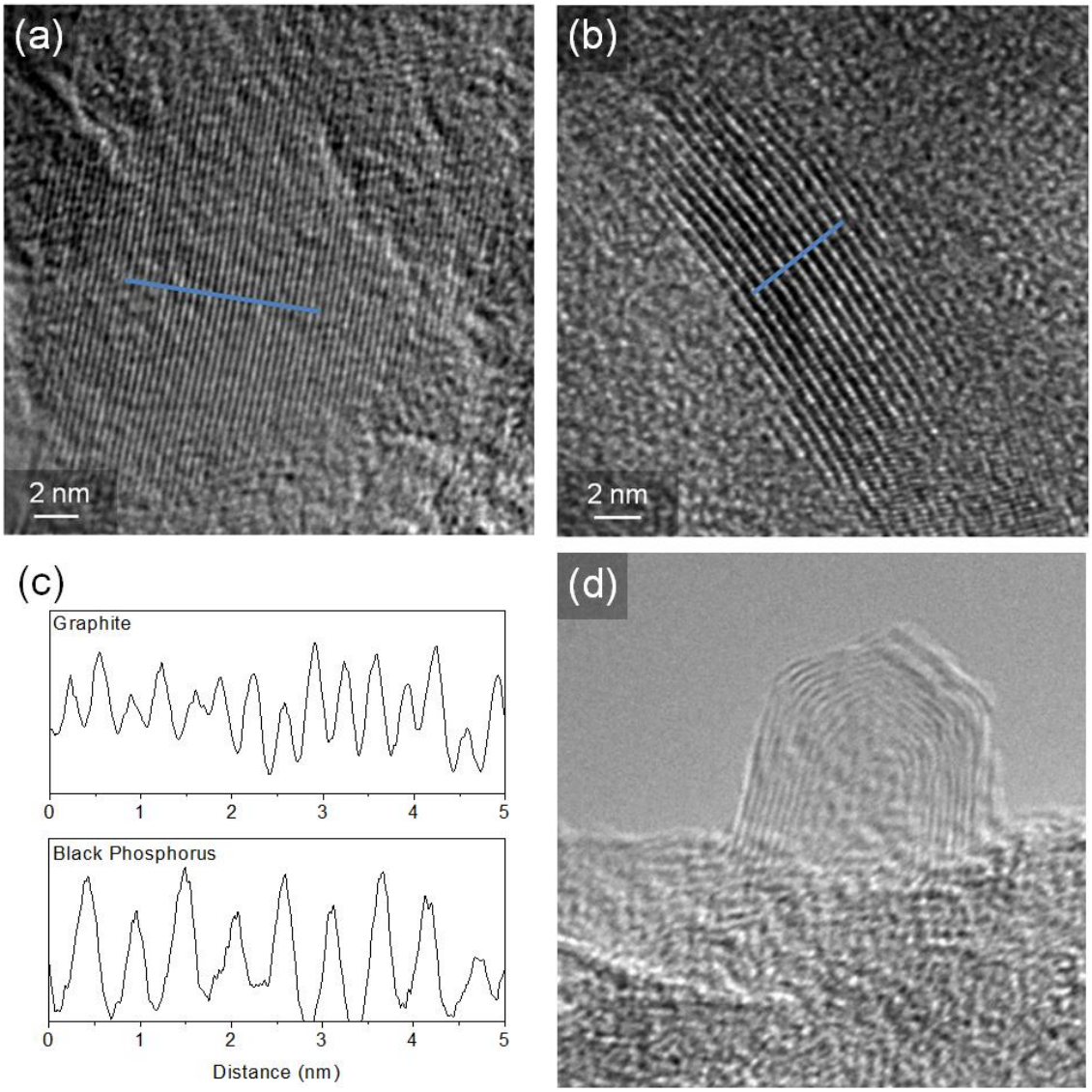

Figure 49. TEM micrographs of 24 hour ball milled P-C with CNT showing regions of (a) graphite (b) orthorhombic black phosphorus and (d) CNT, as well as (c) profiles of the graphite and phosphorus regions identifying the different layer spacings.

Figure 48 shows TEM micrographs of the carbon black and carbon nanotubes, as well as the carbon nanotubes after ball milling for 24 hours. After ball milling, the carbon nanotubes appear to have an amorphous structure, and no nanotubes are visible. Figure 11 shows TEM micrographs of a carbon nanotube P-C composite with CNT. Figure 49a-

b show 2 regions with layered structures, for which the layer spacing was measured via the profile shown in Figure 49c. The region in Figure 49a was found to have a layer spacing of ~0.34 nm and the region in Figure 49b was shown to have a layer spacing of ~0.54 nm. Thus they were respectively identified to be graphite and black phosphorus layers, showing that the ball milling not only forms black phosphorus regions, but also collapses the carbon nanotubes to form graphite regions. This agrees with the XRD spectra shown in Figure 47b which is similar to that of graphite powder. However as seen in Figure 49d, some small amounts of carbon nanotubes were still observed, suggesting that not all of the carbon nanotubes are converted to amorphous and graphitic carbon after 24 h of ball milling.

Figure 50 and Table 13 show the EDS analysis results of a ball milled P-C composite powder. The red phosphorus and carbon nanotubes were loaded into the ball milling jar at a 7-3 ratio, and the the EDS shows that after the ball milling, the P-C ratio is still approximately the same.

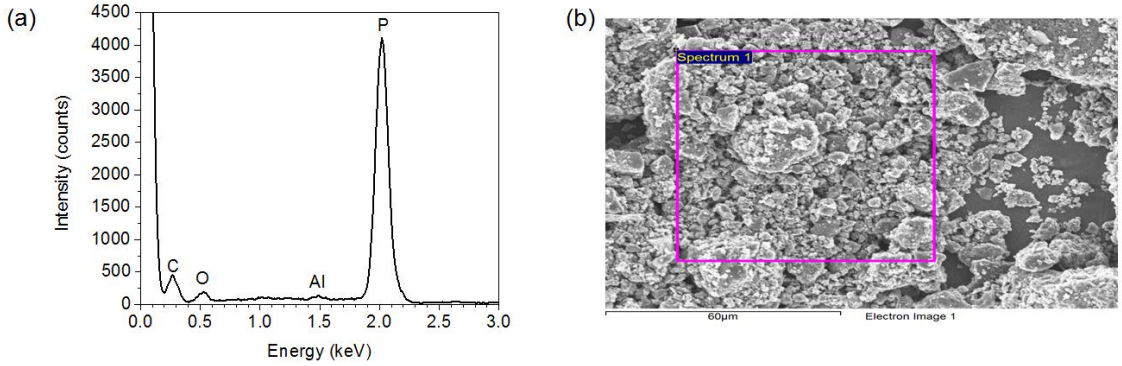

Figure 50. EDS (a) spectrum and (b) analysis area of P-C composite powder of P and carbon nanotubes, ball milled for 24 hour at a 7-3 weight ratio.

Table 13. Quantification of EDS results show in Figure 50.

Element	Weight%	Atomic%
C K	26.76	46.68
O K	5.92	7.75
Al K	0.50	0.39
P K	66.81	45.18

Chapter 10. Phosphorous Anodes Design & Composition

10.1. Methods

10.1.1. Electrode Construction

To understand how current collector, electrolyte, binder, and carbon choices translate to electrode performance, a series of electrodes were cast with ball milled P-C composites. Phosphorus was first ball milled with 30% wt. smaller diameter CNTs (inner diameter 2-5 nm, outer diameter <8nm, length 10-30 μm, 3.8% COOH functionalized) for 24 hour in a stainless steel 80 ml jar with 3 x 3/8 inch 440C stainless steel balls in Ar. The ball to powder mass ratio was 20:1 and a SPEX 8000M mixer mill was used. Next, the powder was mixed in NMP with a polymer binder and carbon conductive additive. The polymer binder was 10 wt.% of either PVDF (280 kDa) or PAA (450 kDa) unless otherwise specified. The carbon conductive additive was 10 wt.% of conductive additives ExG (Timcal SFG6, d90 of 6.5 μm), PB, or CNTs (inner diameter 5-10 nm, outer diameter 20-30 nm, length 10-30 μm, 1.2% COOH functionalized). The mixtures were stirred for over 5 h and sonicated for 10 min before being cast on an Al foil. As PVDF did not adhere well to the Al current collector, an under-layer of PAA and CNTs was cast before the electrode to provide a more meaningful comparison between PVDF and PAA. The PAA:CNT weight ratio was 1:1, and the under-layer slurry was stirred and sonicated for the same length of time as the electrode slurry. Once the under-layer was casted, the NMP was dried immediately via application of a vacuum for 15 min at room temperature. The electrode slurry was then casted on top of the under-layer and also dried immediately under vacuum at room temperature (also for 15 min). Further drying was then performed

in vacuum (~1 mbar) at 70 °C, 120 °C, and 150 °C. The under-layer mass loading was ~0.1 mg/cm^2 and the electrode mass loading was ~1.0 mg/cm^2. All electrode construction steps were performed in an Ar filled glove box with < 20 ppm O_2 and < 0.1 ppm H_2O.

10.1.2. Mechanical Characterization

In a previous study, our group investigated the mechanical properties of PAA and PVDF in air and in DEC [11]. However, battery electrolytes are almost always a combination of linear and cyclic carbonates, and the mechanical properties of the binders have not been measured in cyclic carbonates. To understand how the binders perform in cyclic carbonates, they were first dissolved in NMP and drop cast onto Si wafers. The wafers were cleaned using ethanol and acetone, and then plasma for 20 minutes to remove any organic materials. The deposited solutions were dried immediately in vacuum (~1 mbar) and a set temperature of 70 °C, 120 °C, or 150 °C for 6 hours, resulting in films of 10-30 μm in thickness. The films were then transferred to a Hysitron Triboindenter immediately for measurement of the reduced modulus and hardness. A wide diameter fluid probe with a cono-spherical diamond tip of 20 μm diameter was used, and an empirical area function was used based on a polycarbonate reference for indentation depths of 100 - 700 nm. A wide probe tip was preferred to similar measurements *via* a fully immersed AFM probe, as this reduced the effect of nanoscale surface roughness. For measurements with organic electrolyte solvents, PC and FEC were chosen for convenience, as they are widely utilized electrolyte solvents that are liquids at room temperature and have low vapor pressures. The film's mechanical properties were first measured in air before several drops of the solvent were added to the film. The film was then allowed to swell with solvent for 15 minutes before the

mechanical properties were measured again through the drop of solvent. The percentage change in properties were calculated by comparing the measurements on the same sample before and after the solvent was added. Hardness and modulus were calculated from the data using a polycarbonate reference sample, from which an empirical area function was found on the same day that the measurements were taken [62].

10.1.3. Chemical Characterization

High resolution transmission electron microscopy (TEM) was performed using a Tecnai F30 (FEI, Netherlands) to confirm the microstructure of the ball milled powder and x-ray diffraction (XRD) was performed using a X'Pert Pro Alpha-1 to confirm the microstructure of the casted electrode. Scanning electron microscopy (SEM) was performed on a LEO 1530 FESEM to visualize the morphology of the electrodes. X-ray photoelectron spectroscopy (XPS) was performed to investigate bonding between P and functional groups using a Thermo K Alpha with an Al K alpha monochromatic X-ray source. Ten scans were performed for each spectrum with a dwell time of 50 ms and pass energy of 50 eV. A vacuum sealed air sensitive sample transfer chamber was used to prevent air exposure before XPS analysis. Fourier transform infrared spectroscopy (FTIR) was performed in an attenuated total reflection (ATR) mode using a Thermo Scientific Nicolet iS50, to observe changes in the structure of the binders (PAA, in particular). TGA was performed using a TA Instruments Q600. The electrode was scraped off the Al current collector in air for analysis, and the experiment was performed with 5 °C/min. ramp rate and N_2 atmosphere.

10.1.4. Electrochemical Characterization

Electrochemical characterization was performed in 2032 coin cells in a half-cell configuration with a Li counter electrode. The electrodes were calendared at 3 tons prior to cell construction in order to improve adhesion. A 1M solution of $LiPF_6$ in fluoroethylene carbonate / ethyl methyl carbonate (FEC/EMC) (3:7 by vol.) was used as electrolyte unless otherwise specified. An Arbin Instruments BT-2000 was used for constant current electrochemical cycling. Data points were taken every 5 mV in order to produce differential capacity plots. After 200 cycles at 500 mA/g (i.e. 900 mA/g-P) rate, the electrodes were put in a 60 °C heated chamber and cycled electrochemically again at a constant current to evaluate whether the degradation was due to ionic or electronic causes. EIS was collected for electrodes after charge discharge cycling in potentiostatic mode from 10^6 - 10^{-2} Hz using a Gamry Instruments Reference 600.

10.2. Results and Discussion: Influence of the Current Collector

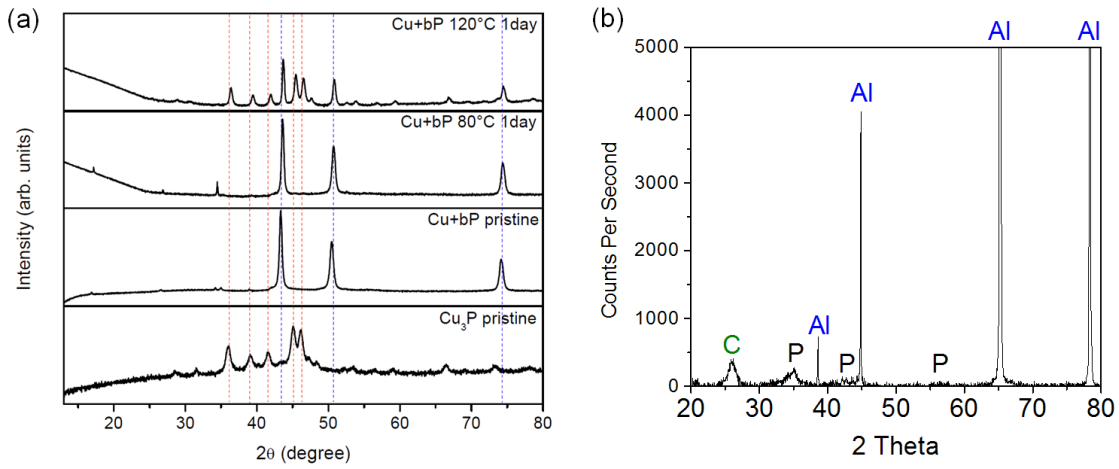

Figure 51. (a) XRD spectra of copper and ball milled black phosphorus powders mixed and heated to different temperatures from literature [167], and (b) XRD spectrum of P-C/PAA/ExG electrode heated to 150 °C for 12 hours.

Phosphorus presents interesting possibilities as an anode material because of its high potential of lithiation. As stated earlier, this allows the use of Al current collector in a phosphorus anode. Al has a lower cost per conductivity than Cu, thus reducing the cost of the overall battery [175]. However, Winter et al. showed in a previous study that a copper current collector can react with black phosphorus to form Cu_3P at merely 120 °C (Figure 51a). Thus in constructing a phosphrous anode, it is critical to show that the electrode does not react with the current collector. Figure 51b shows an XRD spectrum of a phosphorus electrode dried at 150 °C, clearly showing a black phosphorus phase and Al. Black phosphorus appears not to react significantly with the Al current collector, and thus all results presented hereafter are deduced to be of black phosphorus.

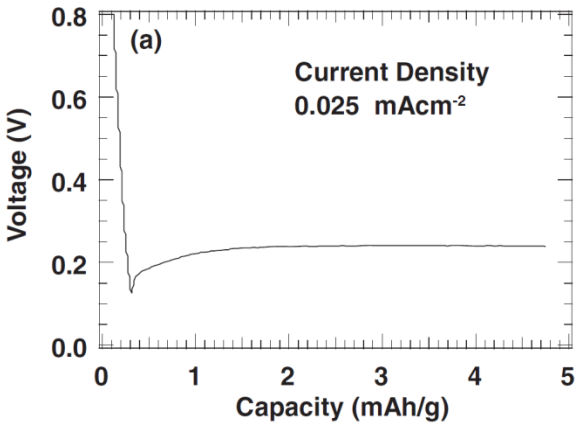

Figure 52. Constant current lithiation voltage profile of an aluminum [176].

Unlike copper, aluminum can be lithiated however, and thus the potential range is slightly more limited than when a copper current collector is used. Al lithiation requires an initial dip in potential as the native oxide is lithiated, after which the potential stabilizes at just below 0.3 V as the Al itself is lithiated (Figure 52). The potential of the anode must be kept above 0.3 V in order to prevent Al lithiation, as Al is easily pulverized by electrochemical lithiation [177]. Conveniently, this potential range also

minimizes the contribution of carbon to the total electrode capacity (see Appendix C), allowing a more phosphorus focused analysis of electrochemical performance.

10.3. Results & Discussion: Impact of Electrolyte

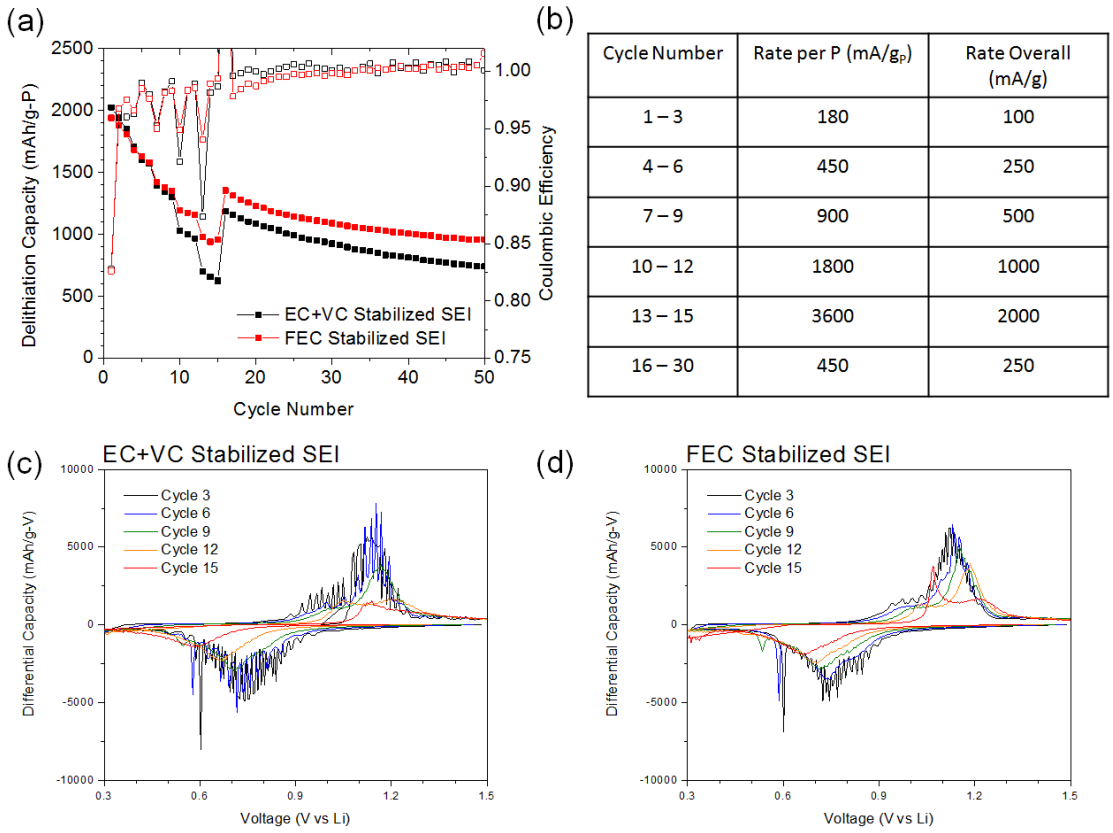

Cycle Number	Rate per P (mA/g_P)	Rate Overall (mA/g)
1 – 3	180	100
4 – 6	450	250
7 – 9	900	500
10 – 12	1800	1000
13 – 15	3600	2000
16 – 30	450	250

Figure 53. (a) Galvanostatic rate test of P-C/PAA/PB electrodes, (b) the rates used, and (c-d) differential capacity plots of the third cycle at each rate.

Electrolyte choice is critical for a conversion electrode to achieve stable cycling. Conversion electrodes generally undergo extreme volume change, and therefore require additives in order to stabilized the SEI. VC and FEC are both additives which have been found to improve the cycle stability of alloying anodes [178]. Figure 53 compares the performance of the two SEI stabilizers. The FEC stabilized electrolyte was 3/7 FEC/EMC by vol. and the VC stabilized electrolyte used EC/DEC/DMC 1/1/1 by vol. with 8 wt. %

VC added afterwards. The FEC stabilized electrolyte has better cycle stability and rate capability than the VC stabilized electrolyte. The difference in polarization is especially clear when comparing the differential capacity plots for 1000mA/g and 2000 mA/g (Figure 53 c-d). Thus the FEC stabilized electrolyte is used hereon.

10.4. Results and Discussion: Impact of Conductive Carbon and Polymer Binder

An electrode slurry is generally a mixture of the active material, a carbon conductive additive, and polymer binder. This is the mixture which is casted on the electrode, and it is this composite material which must maintain mechanical integrity to keep the battery electrode functional. That is, the electrode must have sufficient electrical transport from the active materials to the current collector, while also having sufficient pore volume for the electrolyte to transport the Li away from the active materials. Mechanical fracturing can cause a loss of electrical contact, while SEI growth within the pores can cause prohibitively high ionic resistance. In either case, the cell loses capacity due to the loss of active material. Thus in a conversion anode, binders and carbons must be carefully combined in an electrode to maintain both transport pathways open while withstanding the large volume change. Phosphorus is no exception to this rule, as discussed previously, and it also adds an extra layer of complexity due to its reactivity. Phosphorus could react with polymer binders, and is known to react with water and air.

Previous studies have found CMC, PAA, and alginate to all have good mechanical properties in DEC electrolyte, and thus improve the cycle stability of Si anodes [15,106]. However, CMC and alginate are soluble only in aqueous solution, and the

carboxyl group is likely to react with phosphorus. This reaction could beneficial in forming a good interface between the phosphorus and binder, but could cause issues if the reaction proceeds beyond just a surface layer.

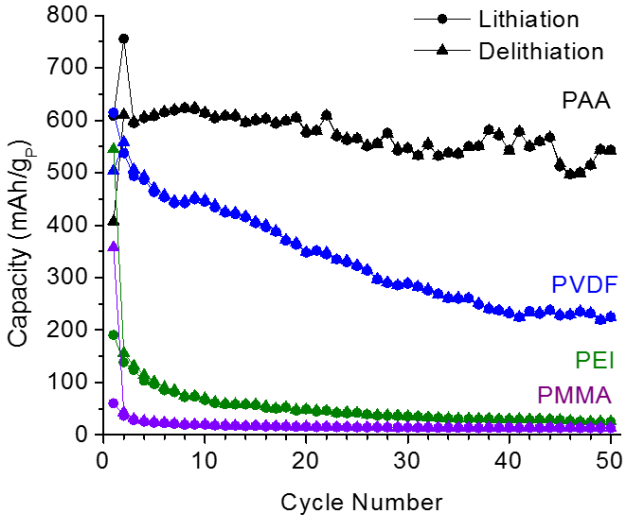

Figure 54. P-C electrodes with PB carbon conductive additive and various binders, cycled with VC stabilized electrolyte at 130mA/g-P rate (C/20) in the 0.78-1.50V range.

As an initial attempt, an array of binders were tested by mixing them in slurries with phosphorus and pure black conductive additive in NMP solvent. Figure 40 shows the cycle stability of P-C/PB electrodes made with PVDF, PAA, PEI, and PMMA binder materials. PVDF is the standard binder material used in commercial batteries, and PAA is a binder known to perform well in conversion anodes, while also being conveniently soluble in NMP. PEI is a polymer which has not received much attention as a binder material, but is interesting due to its fire retardant properties. PMMA is of interest due to its common use for its good mechanical properties as “acrylic glass” in applications such as extremely large windows. The cycle stability of the electrodes were in the order of PAA, PVDF, PEI, and PMMA in order of decreasing stability. PEI and PMMA only had

minimal reversible capacity despite the strict voltage limit and low current rate. Thus further studies focused on PVDF and PAA binders.

In order to better understand how PVDF and PAA perform as binder materials, they were tested in parallel, while varying the drying temperature. Higher temperature may cause a stronger reaction between P-O, while a lower temperature may mitigate it. High drying temperature can additionally cause a polymer binder to crystallize and shrink. This could affect the binder's mechanical properties, while also possibly changing the morphology of the battery. In particular, PVDF is known to swell in DEC electrolyte, and thus crystallizing PVDF should significantly improve its mechanical properties in electrolyte solvent.

However, the mechanical strength of a composite electrode also depends on the carbon which is used. Commercial batteries use a combination of ExG and PB as the conductive additives in batteries, but CNTs have received increasing attention in recent years due to its good mechanical properties and decreasing cost. First, PVDF and PAA are studied in combination with ExG and CNTs, as these particles are of similar dimensions. PB will be compared later.

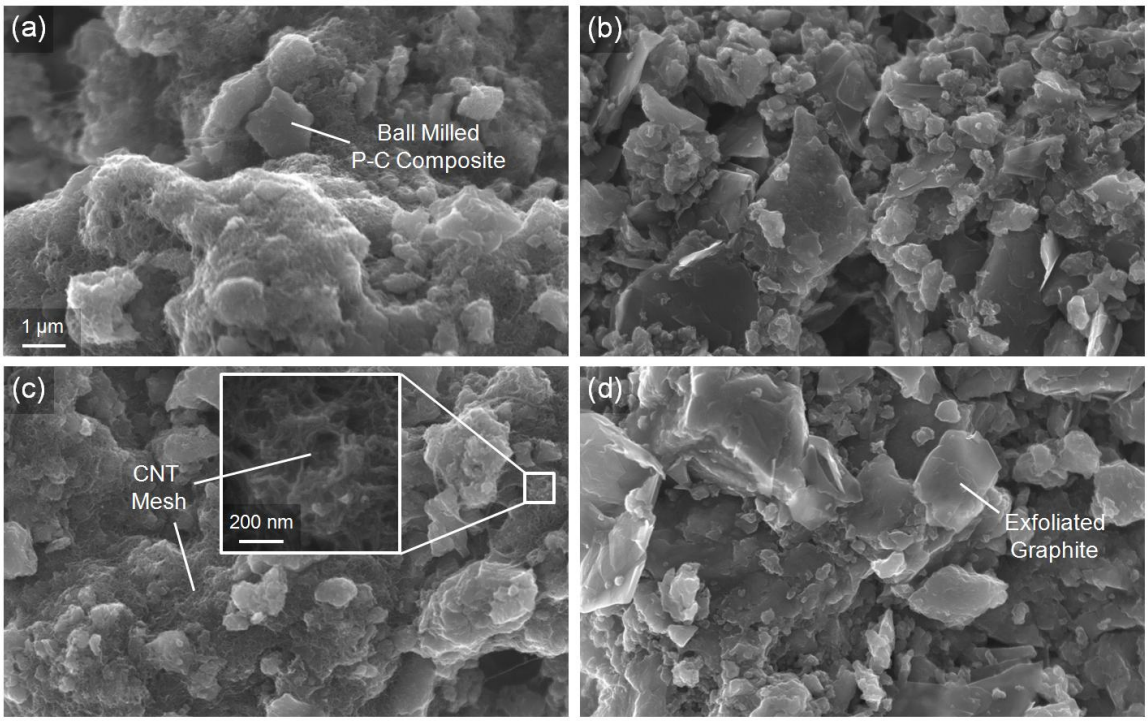

Figure 55. Higher magnification SEM images of fresh P-C electrodes with binder/carbon combinations (a) PVDF/CNT, (b) PVDF/ExG, (c) PAA/CNT, and (d) PAA/ExG.

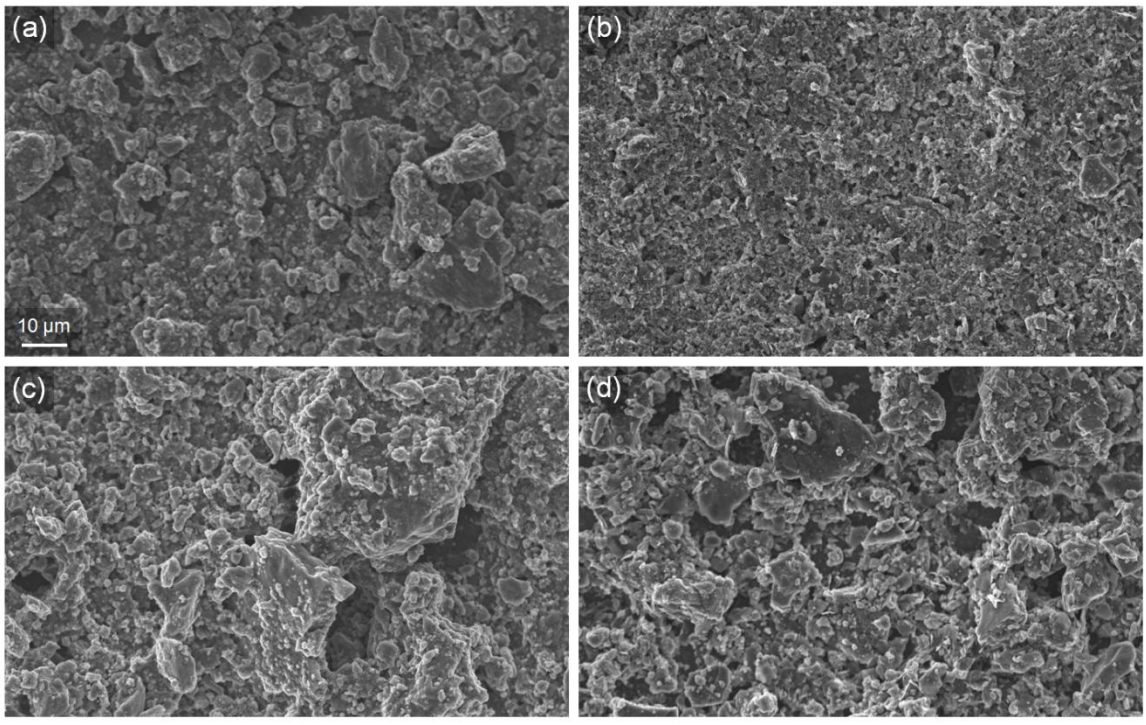

Figure 56. Lower magnification SEM images of fresh P-C electrodes with binder/carbon (a) PVDF/CNT, (b) PVDF/ExG, (c) PAA/CNT, and (d) PAA/ExG.

Figure 55 and show SEM micrographs revealing morphology of the produced composite electrodes. The amorphous looking P-C composite particles, 1-dimensional CNTs, and plate like ExG are all visible in the electrodes. CNTs appear to form a random flexible mesh throughout the electrode, which may assist with maintaining mechanical stability of the electrodes. We also see that the ball milled P-C composite particles have a rather broad size distribution (0.05-50 μm) (Figure 56). This is rather undesirable since large particles may crack or delaminate from the electrodes due to internal stresses created by Li insertion/extraction induced volume changes. The surface roughness is high in all the electrodes (~5-10 μm). This should lead to local non-uniformities in the anode capacity loadings and is harmful for full cell design due to the lack of local anode-to-cathode balance. The negative impact of such loading variations in half cells is significantly smaller because the Li counter electrode maintains a constant potential and has a significant excess of Li capacity, thus preventing Li plating during charging. Since mechanical stresses within the electrodes comprising volume-changing particles are higher for thicker electrodes, locally higher mass loadings may also induce faster fading in half cells. However, since such roughness was similar in all electrodes it was acceptable for our comparative studies.

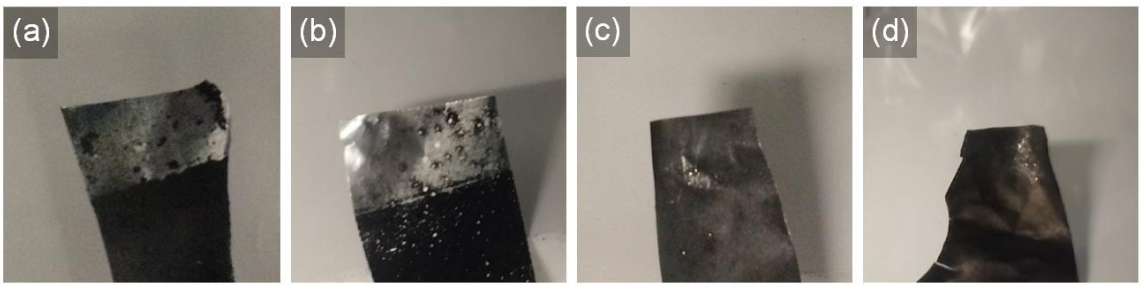

Figure 57. Peel test for electrodes with binder/carbon combinations of (a) PVDF/ExG, (b) PVDF/CNT, (c) PAA/ExG, and (d) PAA/CNT.

Unfortunately, the PVDF-based electrodes did not have sufficient adhesion to the Al foil current collectors according to our peel tests (Figure 57), and this had a direct consequence on electrode performance. In order to make a more meaningful comparison in terms of electrochemical cycle life, a PAA/CNT under-layer was casted between the Al foil and the P-C electrode. This creates a flexible and electrically conductive layer which absorbs the strain between the rigid Al foil and the expanding P active material. In addition, this under-layer increases the contact area between the current collector and the electrode, which additionally improves electrode adhesion. The use of the under-layer offers a clear advantage compared with adding more PAA binder because ionically and electrically resistive PAA increases the electrode resistance and reduces power capability of the cells.

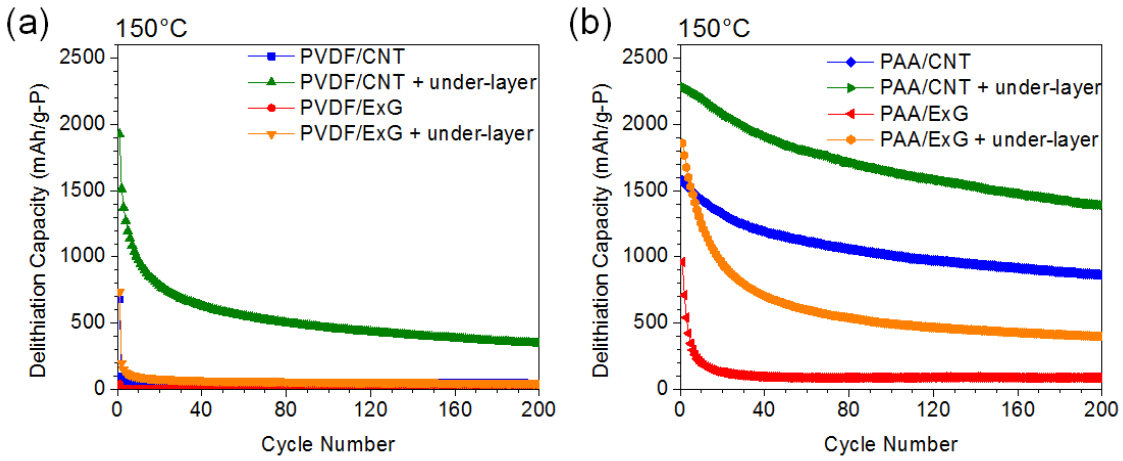

Figure 58. Galvanostatic cycling of P-C composite anodes with various binder/carbon combinations (a) with or (b) without PAA/CNT under-layers, dried at 150 °C and cycled at 900 mA/g-P.

Figure 58a shows the cycle stability of PVDF electrodes with and without PAA/CNT under-layers. Both the PVDF/CNT and PVDF/ExG show improved stability with the under-layer, although the PVDF/ExG still exhibits rapid capacity fading from

the first cycle. This is most likely due to PVDF being both soft (when exposed to the electrolyte and swollen) and chemically inert, and thus being unable to form strong chemical bonds with the current collector, conductive additive, or active material. Without CNT reinforcement, PVDF binder fails to keep the composite electrode held together on its own due to the volume changes in the P-C composite. This issue is mitigated in the case where CNTs are involved, as the CNT mixed with the PVDF significantly enhance mechanical properties of the composite and form multiple electrical contact points with the P-C composite particles, as well as higher surface area for bonding between the binder and CNT. In addition, the use of CNTs in the electrode helps to form stronger bonds with the PAA/CNT under-layer for improved adhesion to the current collector. Furthermore, these benefits are not limited to the PVDF based electrodes, as can be seen from Figure 3b. All further results shown below used the PAA/CNT under-layer, in order to make a more meaningful comparison.

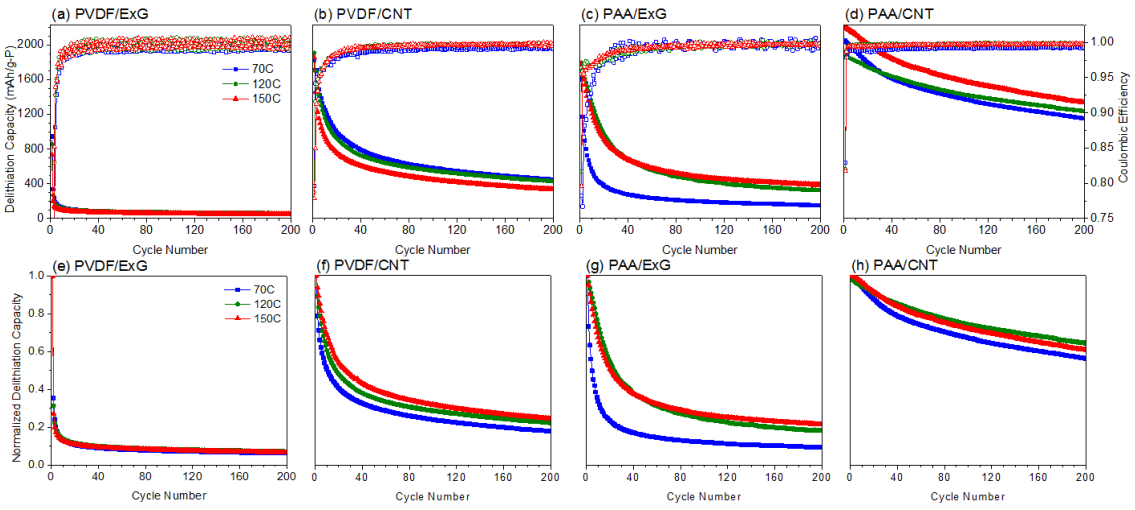

Figure 59. Galvanostatic cycling of P-C composite anodes with various binder/carbon combinations with PAA/CNT under-layers, dried at various temperatures and cycled at 900 mA/g-P.

Figure 59 compares electrochemical cycle stability of these electrodes with either PVDF or PAA binders and CNT or ExG additives when dried at different temperatures. The first cycle capacity of the electrodes dried at different temperatures varied only by ±2-13%. Such small variations at different drying temperatures may realistically be due to the sample-to-sample variations as well as errors in accurately measuring the mass of the electrodes (particularly when hand-casted electrodes and small coin cell electrodes are used). Therefore, normalized capacity cycle life plots are shown below the absolute capacity plots in order to correct for possible mass measurement errors.

Table 14. Surface area of carbon powders used in electrode assembly.

	Surface Area (m^2/g)
P-C Composite	20 (BET)
CNT (20-30nm OD)	55
ExG	17 (BET)
PB	44 (BET)

Several trends could be observed: CNTs as conductive additives and PAA as a binder both have apparent advantages in terms of cycle stability in every combination. When the Li storage capacities are normalized, the effect of temperature becomes apparent. With a PVDF binder, higher drying temperature has a marginal benefit to the cycle capacity (Figure 59e-f). This may be due to the higher degree of crystallization and enhanced mechanical properties of annealed PVDF, as some researchers observed in Si and other anodes [179,180]. Interestingly, for PAA, the cycle stability improved when drying temperature was increased from 70 to 120 °C, but further increase in temperature to 150 °C did not have a significant impact (Figure 59g-h). The negative impact of further increase in the drying temperature might potentially be related either to the unfavorable

changes in bonding between the PAA and the P-C composite particles or the binder shrinkage and the associated increase in stresses within the electrode. We hypothesize (and will later discuss in more detail) that the observed improvements upon heating from 70 to 120 °C may be related to the better extraction of the polar NMP solvent and thus better PAA mechanical properties. ExG has a much lower surface area for bonding (Table 14) with PAA as well as fewer points of electrical contact, and thus is much more strongly affected by the mechanical properties of PAA. Thus PAA/ExG electrodes show lower coulombic efficiency (CE) for the first 20 cycles when dried at 70 °C, and exhibits significantly inferior cycle stability. In contrast, PAA/CNT electrodes are not affected as strongly due to the electrical contacts and better bonding.

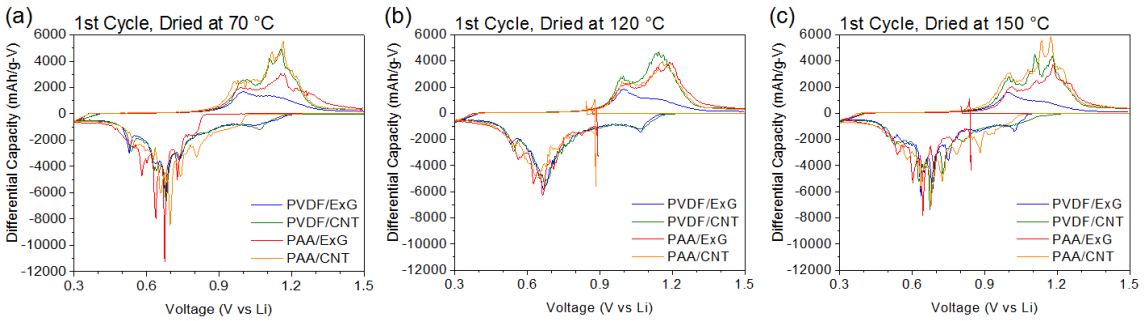

Figure 60. Differential capacity plots of the first cycle of the electrodes constructed with PAA/CNT under-layers and various binder/carbon combinations, cycled at 900 mA/g-P, and dried at (a) 70 °C, (b) 120 °C, and (c) 150 °C.

Figure 60. Differential capacity plots of the first cycle of the electrodes constructed with PAA/CNT under-layers and various binder/carbon combinations, cycled at 900 mA/g-P, and dried at (a) 70 °C, (b) 120 °C, and (c) 150 °C. shows the differential capacity plots of the first cycle of each cell, showing the solid electrolyte interphase (SEI) formation potential, and the potentials at which the lithiation and delithiation mechanisms occur. In every case, electrodes with PVDF show an earlier onset of SEI growth (~ 1.1 V)

compared to PAA (≤ 1 V), as PVDF is permeable to the electrolyte [11] and thus induces less resistance to electrochemical processes. PAA/CNT electrodes generally had a higher SEI onset potential compared to PAA/ExG electrodes. Meanwhile, the anodic delithiation scans look similar in all cases except for PVDF/ExG, where the peak at 1.16 V is weaker than the peak at 1 V. The PVDF/ExG combination appears to be unable to maintain electrical contact with the phosphorus particles as they contract during the first reaction at 1 V, resulting in low first cycle CE (30-40%). The PAA/ExG electrode dried at 70 °C has a trend which is intermediate of the CNT electrodes and the PVDF/ExG electrode, with first cycle CE of 77%. The first cycle CE is 78-80% for PVDF/CNT and PAA/ExG (dried at 120 or 150 °C), and 82-83% for PAA/CNT. This is due to the PAA and/or CNTs providing mechanical support to keep the electrode electrically connected.

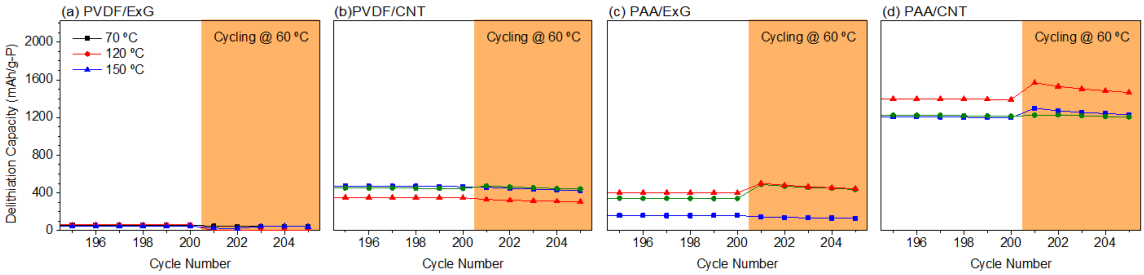

Figure 61. Capacities of electrodes constructed with PAA/CNT under-layers and various binder/carbon combinations, degraded by cycling for 200 cycles at room temperature, then cycled at 60 °C for 5 cycles, both at 900 mA/g-P.

Cycling degraded cells at an elevated temperature should accelerate ionic transport without significantly effecting electrical transport, and thus help to differentiate electrical and ionic degradation mechanisms [181,182]. Figure 61 shows how none of the cells recovered any significant portion of their capacity when cycled afterwards at 60 ºC. This points to the loss of electrical contact between particles, whether via volume change from lithiation/delithiation of P and/or from large SEI growth that induces electrical

isolation of the active material. In any case the degradation of the electrodes is mostly electrical, and therefore directly linked to electrode mechanical integrity.

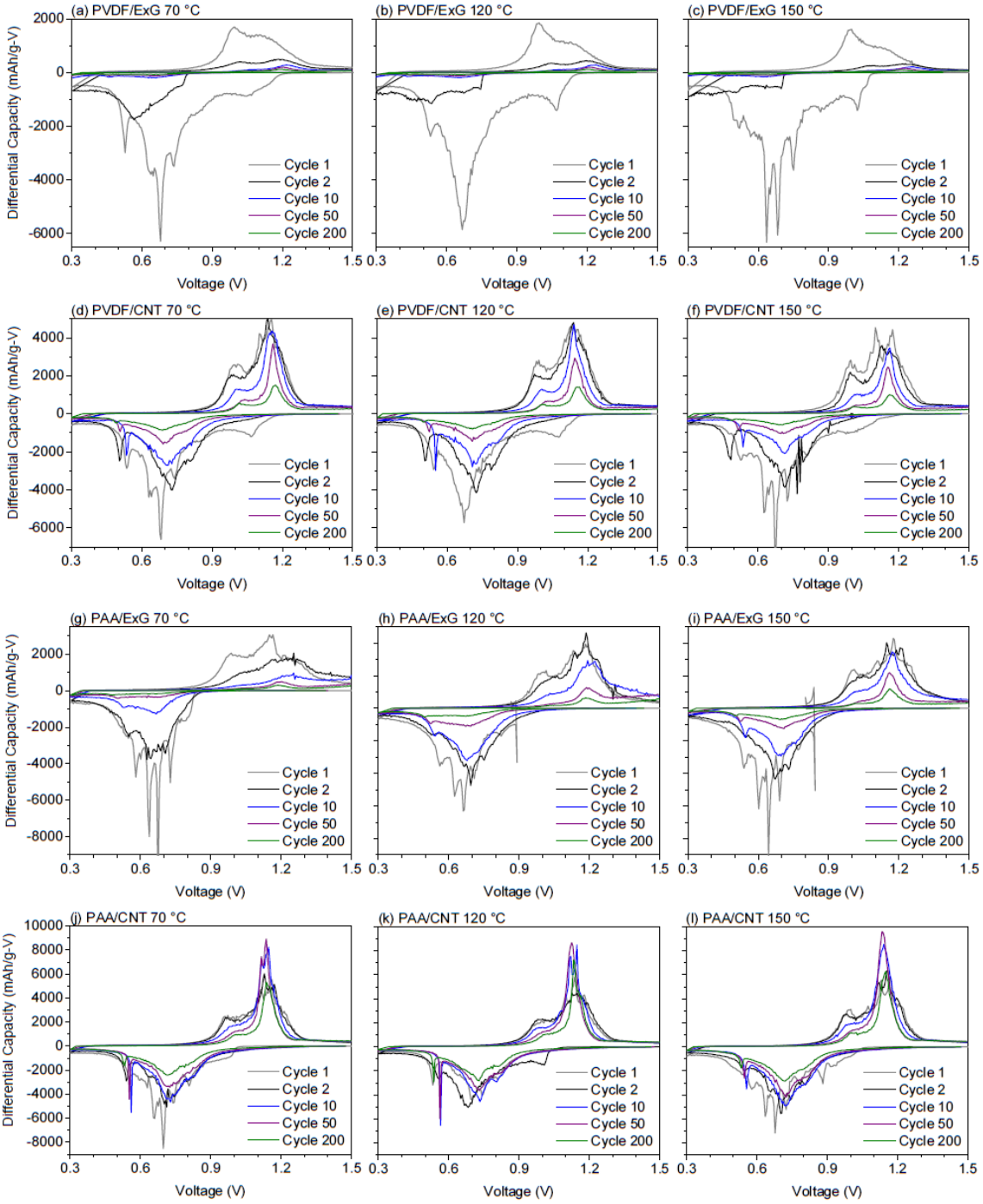

Figure 62. Differential capacity plots showing the electrochemical characteristics of PVDF (a-f) and PAA (g-l) electrodes with underlayers.

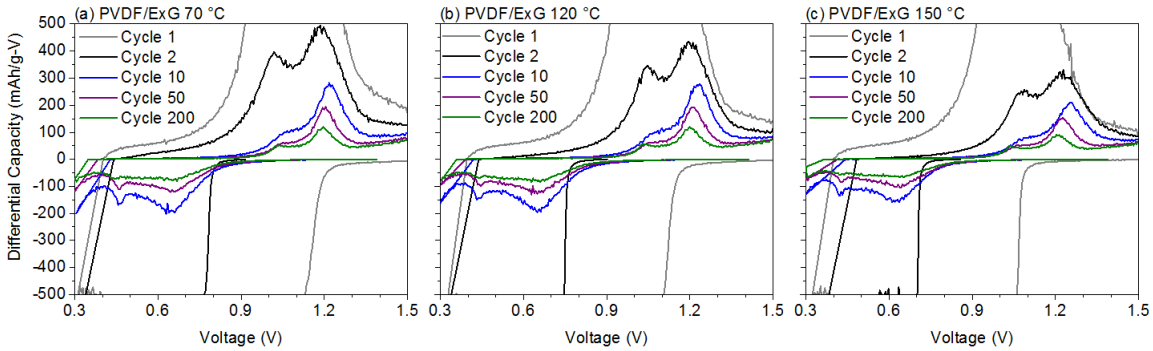

Figure 63. Enlarged view of differential capacity plots for electrodes with PVDF/ExG binder/carbon combination dried at (a) 70 °C, (b) 120 °C, and (c) 150 °C.

Figure 62 and Figure 63 show the differential capacity plots of the electrodes as they degrade during room temperature cycling. In each case, the width of the electrochemical lithiation/delithiation peaks do not become wider or shift to higher overpotential, indicating that the electrodes do not fail due to SEI resistance to Li transport. Instead, the electrodes with PVDF show a tail at the ends of the lithiation (0.3-0.4 V) and delithiation (1.4-1.5 V) which become stronger with degradation with respect to the main lithiation/delithiation peaks at ~0.6/~1.2V respectively. This can be explained by phosphorus particles which have lost many electrical contacts, and have high electrical resistance between the current collector. For these particles, the rate of reaction is severely limited by the transport of electrons, and therefore an extremely high overpotential is required to drive the lithiation/delithiation reactions. Overall, the differential capacity plots also suggest that the degradation is electronic rather than ionic.

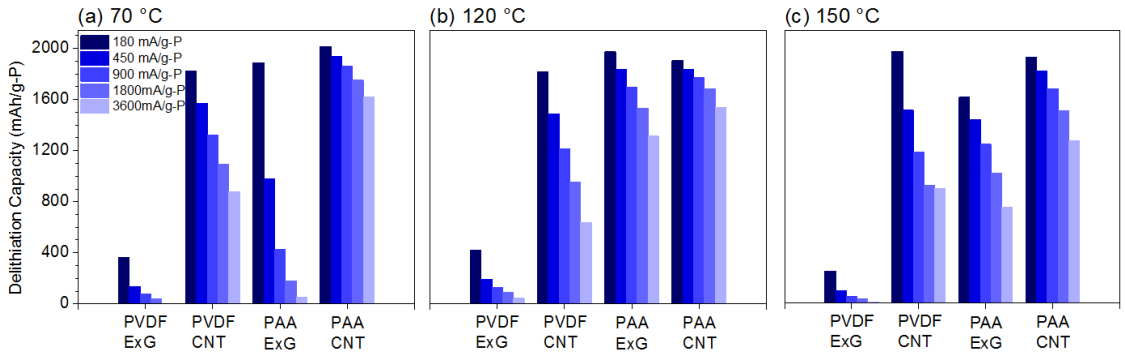

Figure 64. Summary of rate capabilities of electrodes with PAA/CNT under-layers with various binder/carbon combinations and dried at (a) 70 °C, (b) 120 °C, and (c) 150 °C.

Rate tests were also performed on the cells to compare how the electrodes fared under different rates. Figure 64 shows the results of these rate tests in redacted form for easier comparison. Overall, the rate capabilities of all electrodes correlate well with the results from the cycle stability tests and are affected by electrodes' stability. Both CNTs and PAA enhance the rate performance. Since PVDF-based electrodes degrade mechanically, the reduced capacity at higher current densities is affected by such a degradation. CNTs enhance both mechanical stability and electrical connectivity within the electrode and thus may have both indirect (via cycle stability) and direct impacts on better rate performance. Overall, higher drying temperature decreased the rate capability of the electrodes. This may suggest that heating decreases the electronic/ionic pathways within the electrodes. 120 °C dried electrodes perform noticeably better than the 150 °C dried electrodes (compare Figure 64b and c), even when the cycle stability was similar (e.g., with PAA/CNT electrodes). This may suggest that higher temperature drying at 150 °C either reduces the number of electronic pathways within the electrodes (e.g., due to shrinking) or reduces ionic conductivity (e.g., due to reduced swelling in electrolyte).

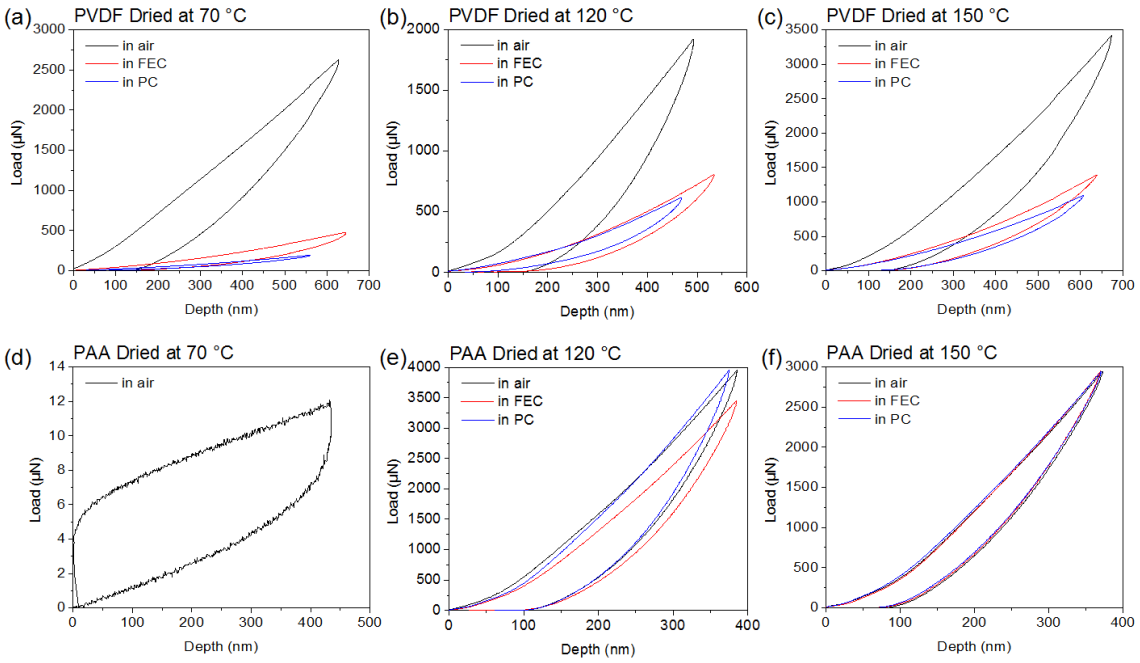

Figure 65. Indentation mechanical property measurements in air and in FEC or PC solution for polymer films of PVDF (a-c) and PAA (d-f) dried at (a,d) 70 °C, (b,e) 120 °C, and (c,f) 150 °C.

Figure 65 shows representative indentation mechanical property measurements for PAA and PVDF films. For PAA, films dried at 70 °C had extremely low mechanical properties, too low to be measured with the available setup. This was most likely due to NMP not being fully removed at that low temperature, as the same issue did not occur when water was used (Figure 68). However, when the films were dried to 120 °C or 150 °C, they exhibited good mechanical properties similar to that which has been reported previously [11,14]. These properties did not change when the films were immersed in FEC or PC solvent. PVDF, on the other hand, had significantly reduced mechanical properties in FEC and PC, especially in the case of the film dried at 70 °C. The mechanical properties of PVDF also appear to be slightly better in FEC compared to PC, and the effect is not as drastic as previously reported for DEC [11,15].

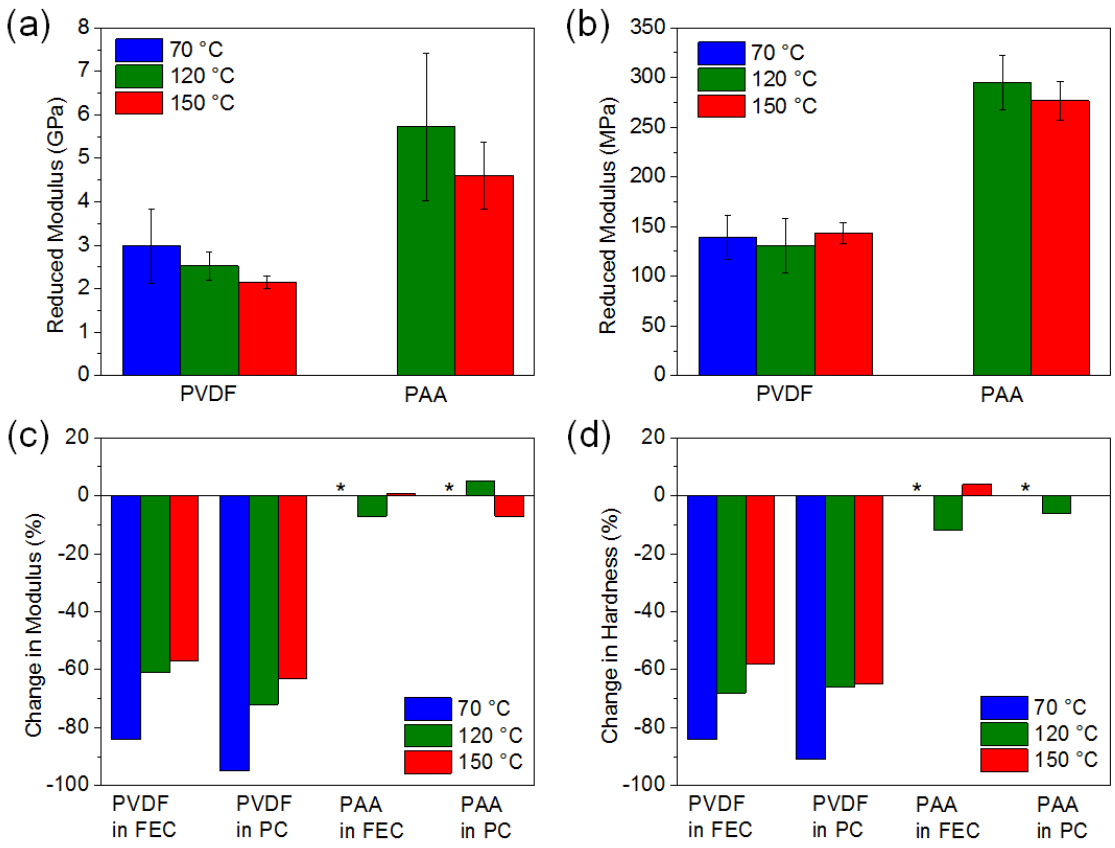

Figure 66. Summary of the (a) reduced modulus and (b) hardness of PVDF and PAA cast from NMP, and the changes in these mechanical properties when in solvent (c-d). *Measurements were not taken in FEC or PC for PAA dried at 70 °C .

Drying the polymers above the glass transition temperature should allow the films to anneal, filling in pores that form during drying (see Figure 90). This should improve the measured mechanical properties of the polymer films. A quantitative summary of the mechanical property measurements is shown in Figure 66. The error bars shown show the 95% confidence intervals calculated using a t-distribution. The results show that PAA has higher modulus and hardness than PVDF, but that no significant difference could be observed as a result of changing the drying temperature due to the large spread in data. PVDF does have higher modulus and hardness in FEC and PC solvents when dried at

higher temperature, most likely due to crystallization. This correlates with the small increase in cycle stability observed for PVDF/CNT electrodes (Figure 59f).

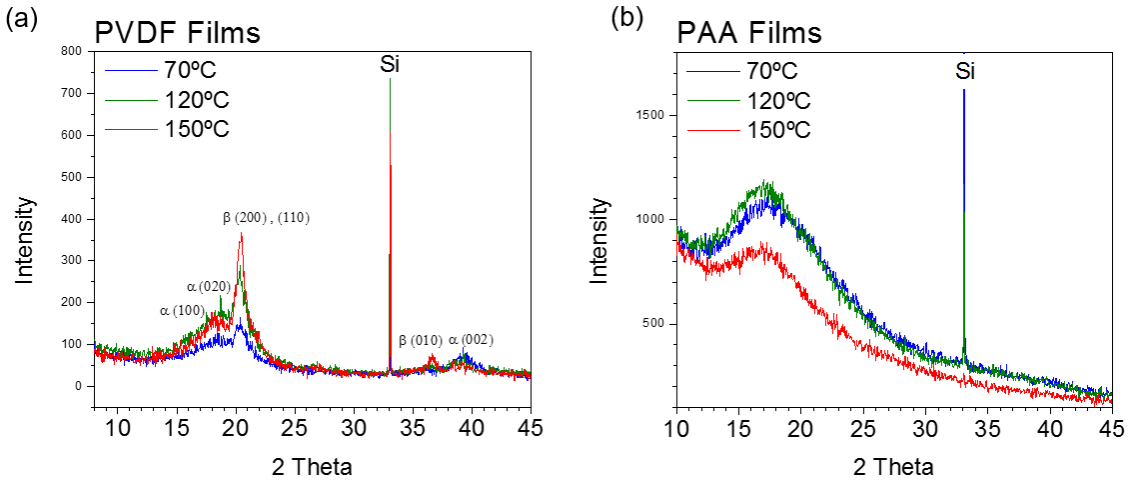

Figure 67. XRD spectra of (a) PVDF and (b) PAA films casted on Si wafers and dried at different drying temperatures.

XRD spectra shown in Figure 67 indicate increasing crystallinity with higher drying temperature for PVDF. Between 70 and 120 °C, the intensity of the α and β phase peaks both increase, and between the 120 and 150 °C the intensity of the β phase peaks increase. The result is a decrease in swelling (as observed in Figure 67) and an increase in density (the densities of amorphous, α, and β phase PVDF are 1.68, 1.98, and ~2.03 g/cm^3 respectively). PAA, on the other hand, does not show any difference in crystallinity, and only exhibits a broad amorphous peak at 2θ of ~17°. Thus the change in mechanical properties and electrochemical cycling stability observed between 70 and 120 °C drying temperature is most likely not due to crystallization of the polymer.

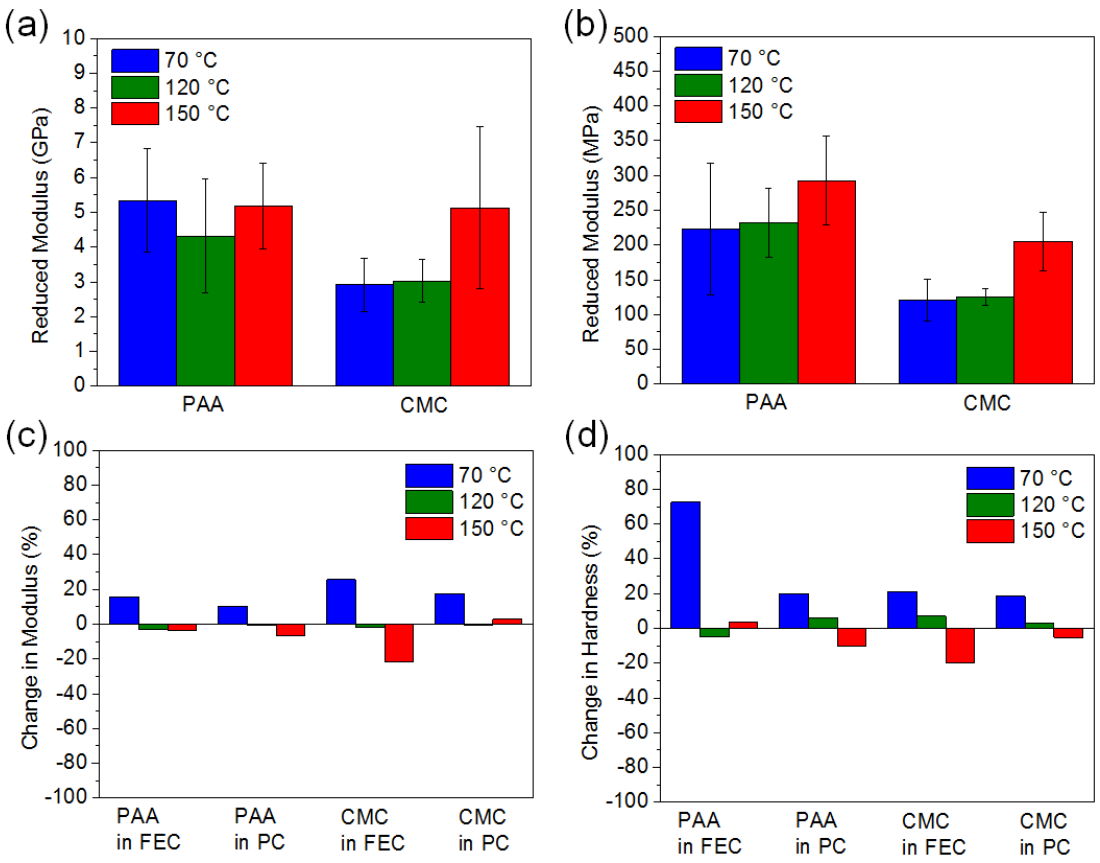

Figure 68. Summary of the (a) reduced modulus and (b) hardness of PAA and CMC cast from water, and the changes in these mechanical properties when in solvent (c-d).

Figure 68 is an interesting contrast to Figure 66 in that mechanical properties are actually observed to improve in FEC and PC solvent for films dried at 70 °C. On the other hand, films dried at 150 °C tend to have a slight decrease in mechanical properties. We hypothesize that these differences are also caused by the incomplete removal of solvent when the film was cast. The 70 °C most likely still has water in the film, which is leeched out by the FEC or PC solvent drop, increasing its mechanical properties. For the 150 °C, the opposite occurs, as the films are completely dry. In particular, CMC appears to slightly swell in the presence of FEC.

While hardness and modulus results explain some of the differences in cycle stability, the effectiveness of a polymer binder may not be determined by the mechanical properties alone [13,183,184]. For example, if the binder does not have good adhesion with the current collector, the carbon conductive additive, and the active material, its mechanical properties may become largely irrelevant if volume-changing materials are used. As mentioned earlier, PVDF is unable to adhere to the current collector (Figure 57), and may also have similar problems forming good interfaces with other components of the electrode as well. PAA, on the other hand, is often used as an adhesive as the carboxyl group is able to chemically bind to many surfaces. To investigate how the chemical bonding of the polymer changes with drying temperature, X-ray photoelectron spectroscopy (XPS) and Fourier Transform Infrared Spectroscopy (FTIR) were used.

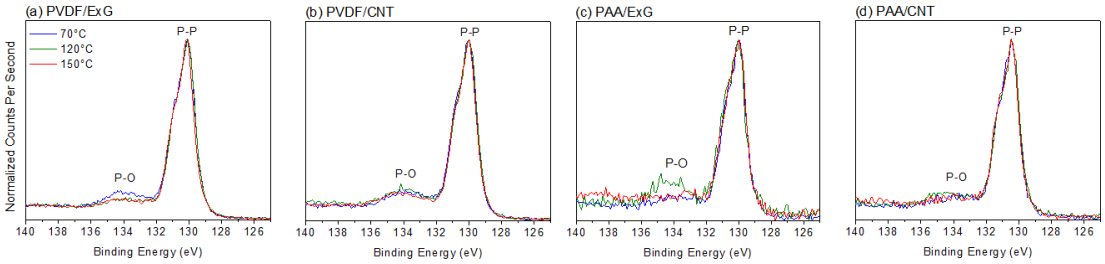

Figure 69. XPS P2p spectra of P-C composite electrodes casted with various binder/carbon combinations and dried at 70 °C, 120 °C, or 150 °C.

Figure 69 shows the P_{2p} spectra for the freshly constructed electrodes. Contrary to our expectations [185], XPS did not show significant P-O bond formation for PAA electrodes, despite the presence of acidic carboxyl groups. This may be due to the surface sensitivity of XPS. Lab scale XPS equipment uses an Al K alpha x-ray source, meaning that escaping electrons only have ~1kV kinetic energy. Thus only the top few nm of the material is observable, and much of the interface between PAA and phosphorus may not

be visible in XPS. Although P-O bonds were observed in certain cases, this was not correlated to any particular binder, conductive additive, or temperature combination, and, we conclude, were most likely due to uncontrolled air exposure (e.g. due to small leaks) and impurities vaporized inside the heated chamber during drying.

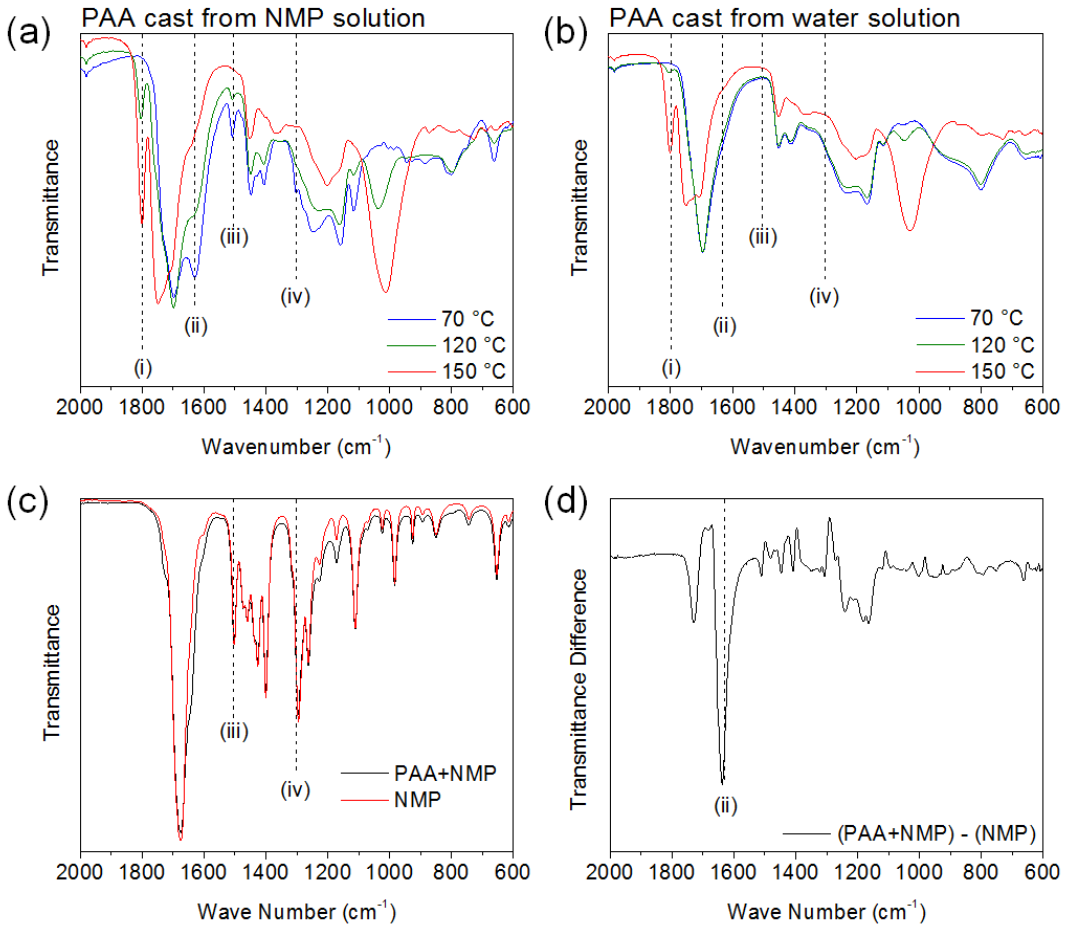

Figure 70. FTIR spectra of PAA films cast from (a) NMP and (b) water solutions, (c) NMP and a 10 wt. % solution of PAA in NMP, and (d) the difference between the two spectra in (c).

Figure 70 shows the FTIR spectra observed for PAA films casted and dried at different temperatures from different solvents. While the FTIR analysis was attempted on the full electrodes, meaningful and repeatable results could not be obtained due to low binder composition, the presence of infrared absorbing carbon, and overlap of the main

C=O stretch peak with the graphitic C=C stretch (Figure 71). However, FTIR spectra of pure PAA films clearly show two significant processes which occur due to increased drying temperature. Firstly, peak (i) at 1800 cm^{-1} is the C=O asymmetric stretching vibration from anhydride bridges formed between carboxyl groups, and peak (ii) at 1630 cm^{-1} is the C=O stretching vibration of the carboxyl groups which have not undergone the condensation reaction to form anhydride [186-188]. The anhydride peak predictably becomes stronger at higher drying temperatures while the free carboxyl group peak becomes weaker. Peaks (iii) at 1500 cm^{-1} and (iv) at 1295 cm^{-1} are characteristic of NMP, as seen in Figure 11c. Surprisingly, these peaks are present in the dried electrodes, and only completely disappear for the film dried at 150 °C. Meanwhile, PAA cast from water solution does not exhibit any peaks at the corresponding wavelengths. PAA cast from water and dried at 70 °C and 120 °C also have the major C=O vibration peak at 1700 cm^{-1} instead of 1630 cm^{-1}. We hypothesize that the lower frequency of the C=O vibration for PAA cast from NMP is due to the weakening of the bond due to H^+ dissociation. NMP is a better cation acceptor than water [189], whereas PAA contains an acidic carboxyl group. This strong interaction between NMP and PAA, combined with the higher boiling point of NMP most likely make NMP difficult to evaporate from a solution with PAA.

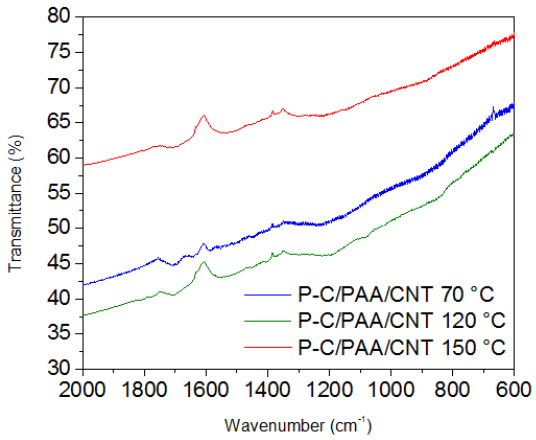

Figure 71. FTIR spectra of P-C/PAA/CNT electrodes dried at various temperatures and collected in transmission mode.

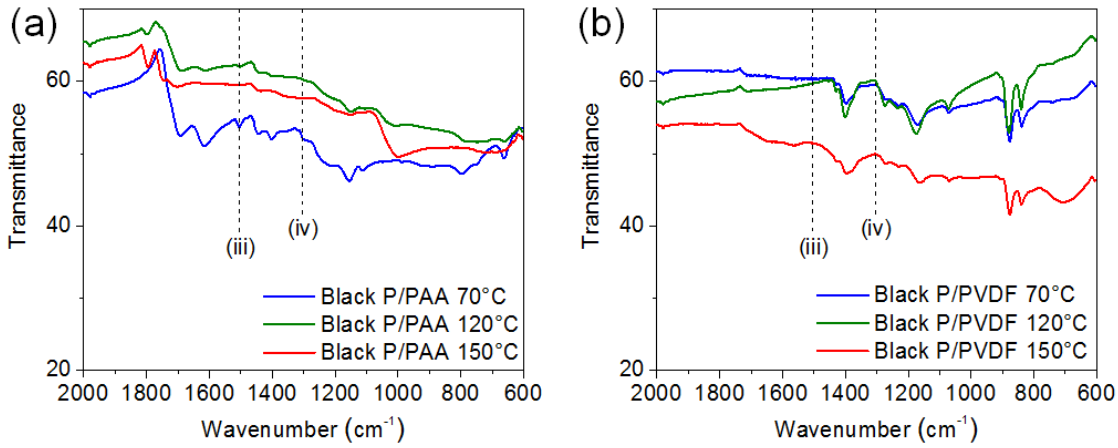

Figure 72. FTIR spectra for model electrodes constructed with ball milled black phosphorus and (a) PAA or (b) PVDF binder, dried at various temperatures.

Figure 72 shows the FTIR spectra for model electrodes constructed without carbon. Commercial red phosphorus was ball milled for 1 hour to form ball milled black phosphorus, and cast with the polymer binders without any carbon conductive additives. While the peaks are very weak, peak (iii) and (iv) are clearly present for Black P/PAA dried at 70 °C. The same is not true for any of the other spectra with PAA or PVDF. Thus these trends explain the anomalously low mechanical properties measured for PAA films

dried at 70 °C. The PAA was most likely a gel of NMP and PAA, and thus had much lower mechanical properties than the fully dried PAA. Similarly, the abrupt improvement in cycle performance for PAA/ExG electrodes when the drying temperature was increased from 70 °C to 120 °C can be explained by this increase in mechanical properties.

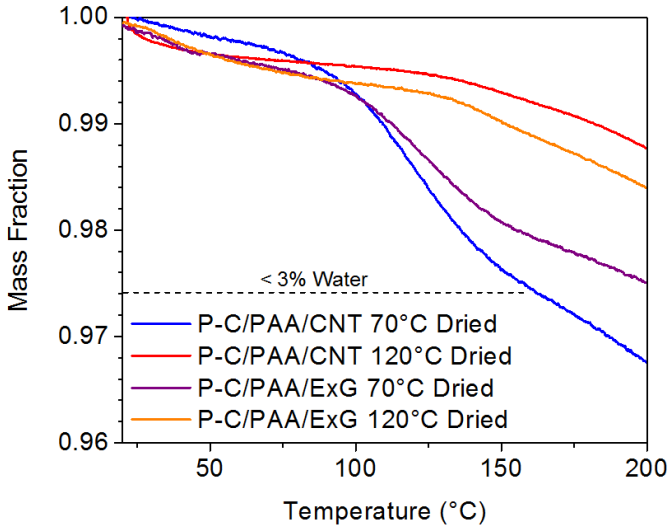

Figure 73. Thermogravimetric analysis of P-C electrodes with PAA binder and cast in NMP inside a Ar glove box atmosphere.

Here we should note that an alternative explanation of the difference in performance is that higher drying temperature simply removes water. It is common knowledge that water is detrimental to a Li-ion battery because it can react with $LiPF_6$ to produce HF, which can in turn be detrimental to the SEI. HF degradation of the SEI can harm a half cell by increasing the electrochemical impedance to Li transport, or by pushing particles apart and causing the loss of electrical contact. The effect of trace levels of NMP on the stability of the SEI is unknown, but could also be detrimental. Increasing impedance is not the mechanism of degradation observed in this study, as discussed

earlier (Figure 59 - Figure 63). TGA analysis also shows that the amount of water present is no more than ~3% at most (Figure 73). This puts the water content to be at most ~1000 ppm per mass of the electrolyte. At this level, water has been experimentally shown to have no detrimental effect on cycle stability with the proper electrolyte additives [190]. Therefore, we conclude that higher water and NMP content may have caused the SEI layer to become thicker, and further exacerbated the issue of volume expansion. This would have compounded the issue of PAA having inferior mechanical properties when dried at 70 °C, resulting in worse cycle stability for the PAA/ExG electrode. However, the same effect was not observed in PAA/CNT electrodes due to the mechanical stability and electrical contacts offered by the CNT mesh.

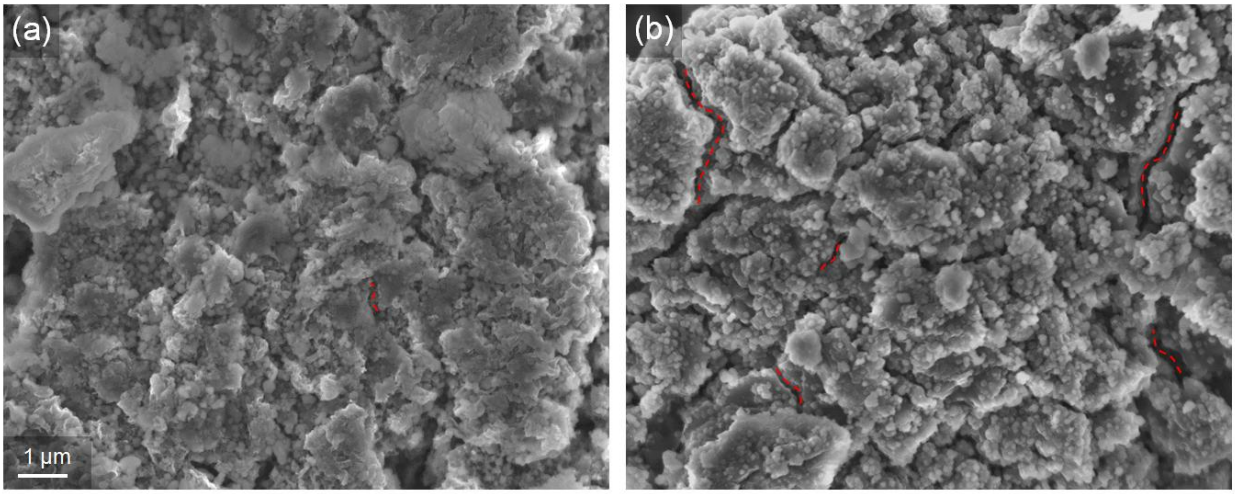

Figure 74. Representative post mortem SEM images, from P-C electrodes with binder/carbon combinations of (a) PAA/CNT and (b) PAA/ExG, and dried at 150 °C, both with PAA/CNT under-layers and after 200 cycles. Red dotted lines highlight areas in which neighboring particles have fitting contours.

Finally, Figure 74 shows representative post mortem images of the electrodes with PAA/CNT and PAA/ExG binder/carbon combinations. Unsurpringly, both show significant SEI growth. For the PAA/CNT electrode in particular, SEI growth has made

particles difficult to discern in most areas. This is reasonable considering the CNT meshes seen in the fresh electrodes (Figure 55). However, for the PAA/ExG electrode, the particles are discernible, and the contours of many of the identifiable particles appear to match their neighbors.

We hypothesize three possible ways in which these shapes may have formed. First, these matching contour lines could be due to SEI growth filling all the gaps between the particles, which then separate when the particles shrink during delithiation. Second, they may also have been caused by repeated expansion/contractions in confined spaces resulting in a change in particle morphology [191]. Finally, matching contours may simply be due to particle fracturing [192]. In areas which neighboring contours match but there does not appear to be thick SEI growth, the first mechanism is unlikely. These have been highlighted with red dotted lines. As can be seen from the shape of the dotted lines, these cracks appear to have bends and turns which are unlikely to be caused by the second mechanism. Thus we believe that the observed matching contour lines are in fact fractured particles.

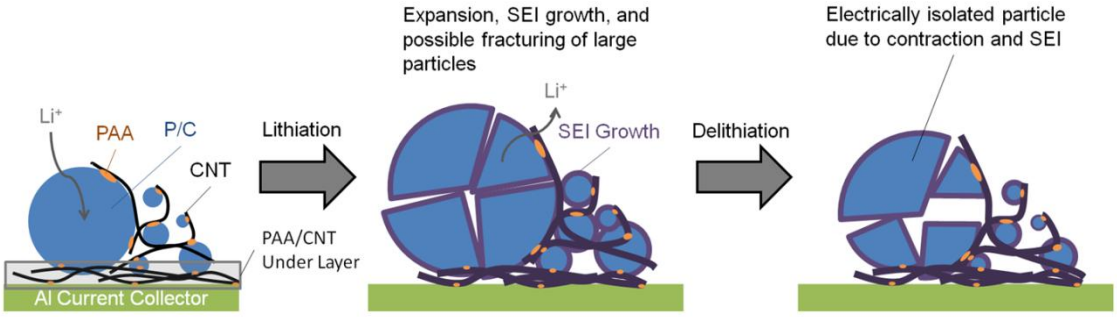

Figure 75. Proposed degradation mechanism of PAA/CNT electrodes with PAA/CNT under-layers.

Based on the discussed above observations, we propose the following mechanism of mechanical degradation of the best performing ball milled P-C electrode shown in Figure 75. The PAA/CNT under-layer greatly improved adhesion to the current collector, while the CNT additive in the electrode create a flexible conductive network, in which the P-C composite particles become embedded. Strong adhesion of the PAA binder to all particles and the current collector and its good mechanical properties (even when immersed in electrolyte) helps to maintain robust electrical contacts between the individual P-C composite particles, CNTs, and the current collector. However, large P-C composite particles initially present in the electrode (Figure 56) may pulverize into smaller pieces with electrochemical charge discharge. While individual black phosphorus flakes have been shown not to pulverize into smaller particles via in situ TEM [193], the carbon matrix itself may still fracture. The resulting pulverized particles may not have good electrical contact, and become electrochemically inactive. The thick SEI growth on the electrodes (Figure 74) exacerbates this process by coating all electrically conductive material with an electrically insulating layer. As a result the electrode slowly fails due to the irrecoverable loss of active material.

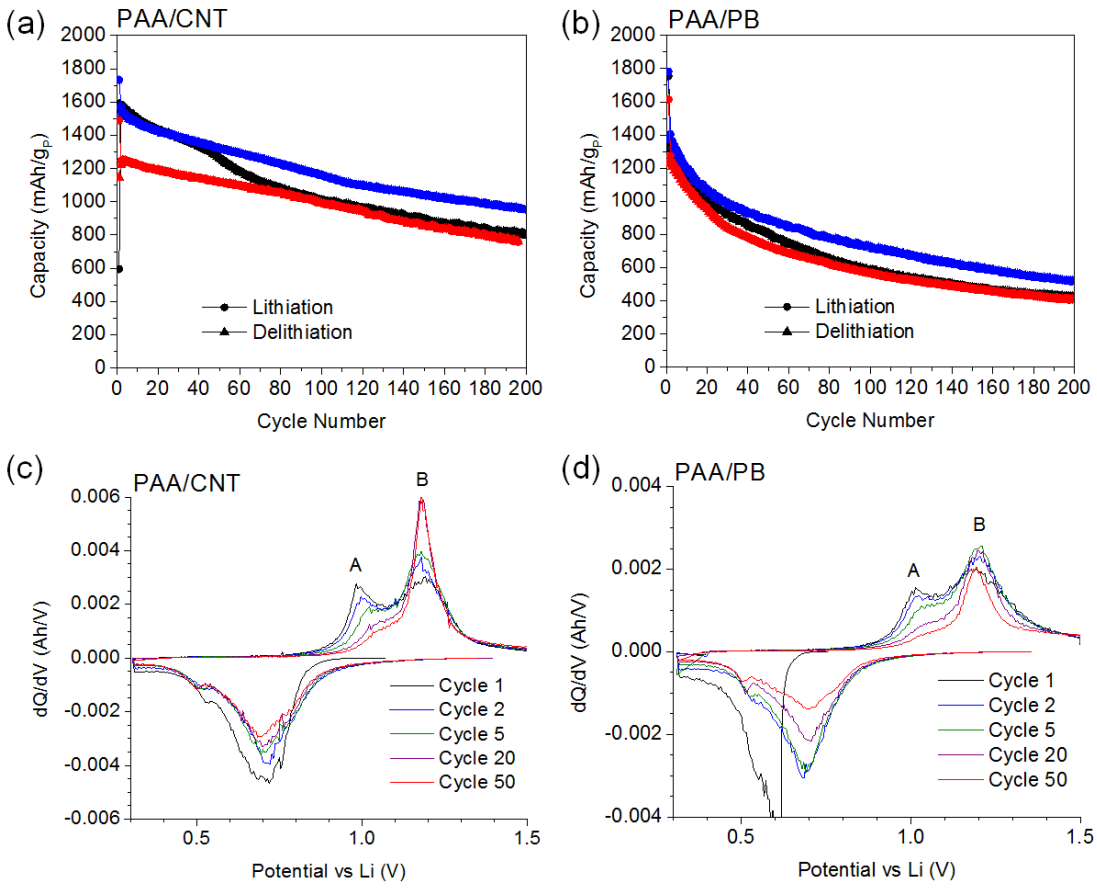

Figure 76. 1800mA/g-P cycling of P-C electrodes with binder/carbon combinations of (a) PAA/CNT and (b) PAA/PB and (c-d) their respective differential capacity plots.

Figure 76a-b show the cycle life of P-C composite electrodes constructed with CNT or PB carbon conductive additives and dried at 120 °C. Multiple cells are shown to account for cell to cell variations due to experimental error. Whereas PAA/CNT electrodes had ~60% of their initial capacity after 200 cycles (Figure 76a), the PAA/PB electrodes only had ~30% of their initial capacity after 200 cycles (Figure 76b). This most likely due to CNT adding additional mechanical integrity to the electrode, as discussed previously.

Figure 76c-d show the differential capacity plots at different cycle numbers, showing the electrochemical degradation of the electrodes. There are no significant shifts in peak positions, with perhaps the exception of the delithiation peak A. For both CNT and PB, delithiation peak A became weaker and/or shifts to greater polarization with degradation while peak B becomes stronger. This is counterintuitive and is rather unfortunate from the perspective of cell voltage. Phosphorus requires a larger overpotential compared to materials such as graphite and Si, and it appears that there is a mechanism by which the overpotential becomes larger with cycling. This phenomenon is investigated discussed further in the mechanism chapter of this thesis.

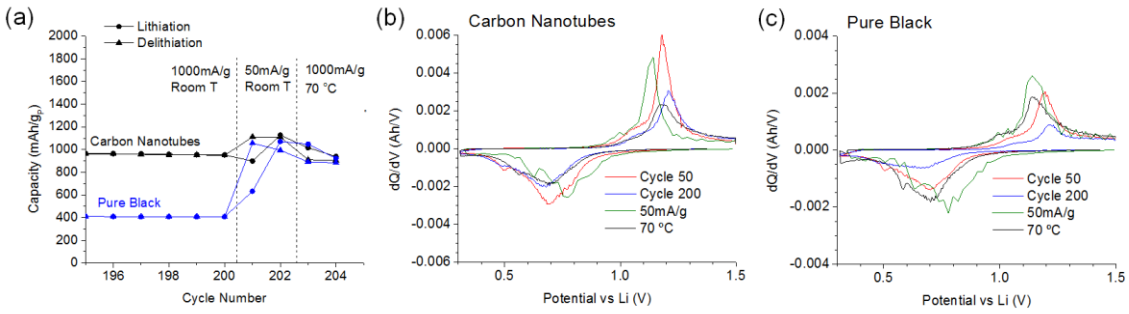

Figure 77. (a) Low rate and high temperature cycling after the electrodes have been degraded by 200 cycles of 1000 mA/g (1800mA/g-P) cycling at room temperature and differential capacity plots of (b) PAA/CNT and (c) PAA/PB electrodes.

To further understand the degradation mechanism, the cells were cycled at low rate and high temperature after the 200 cycles of room temperature galvanostatic cycling. The results show that the PB electrodes have greater ionic resistance compared to the CNT electrodes. While the PB electrode has degraded and has much lower capacity than the CNT electrode at room temperature, when the cycle rate is reduce to a lower rate or the temperature is raised to 70 °C, the capacity and polarization of the two electrodes are virtually the same. This may have to do with the entanglement of CNTs in the electrode.

1 dimensional CNTs most likely do not pack as densely as spherical PB particles. Thus the CNT electrode most likely has greater pore volume and thus better ionic transport than the PB electrode. Whereas ExG flakes were large and thus suffered from mechanical stability issues due to low surface area for PAA binding, the PB particles have high surface area for PAA binding Table 14. However, the high packing density of PB particles results in the electrodes being clogged by the SEI and thus the electrodes degrade ionically. While CNTs are certainly beneficial to the construction of P-C composite anodes, it is important that the CNTs are well dispersed. Just as CNTs become entangled in the electrode, CNTs in powder form also tend to be entangled, and are difficult to disperse well into solvent.

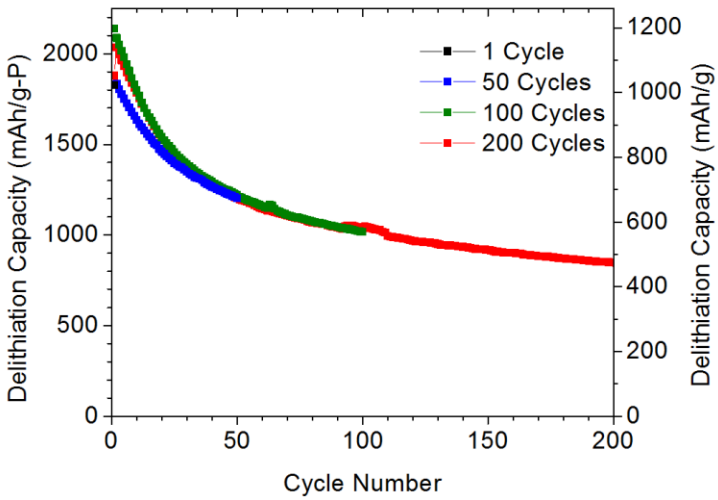

Figure 78. 900 mA/g-P (500 mA/g) galvanostatic cycling of P-C/PAA/CNT electrodes casted from a slurry which was not sonicated.

Figure 78 shows the cycle life of P-C/PAA/CNT electrodes casted from NMP without sonication. Whereas the sonicated slurries resulted in electrodes which retained ~60% of their initial capacity after 200 cycles, these electrodes only retained ~40% of their initial capacity. Massive SEI growth can clearly be seen in Figure 79 with extended

cycling, showing that the SEI continues to grow after the initial cycles. This agrees with the electrode degradation model previously proposed (Figure 75).

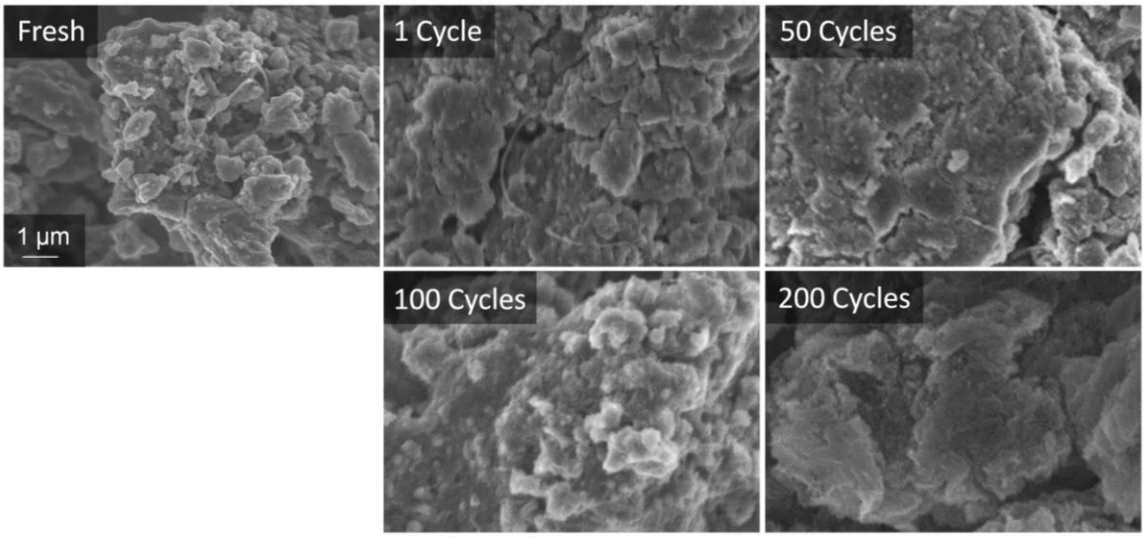

Figure 79. SEM images of P-C/PAA/CNT electrodes casted from a slurry that was sonicated and cycled for a number of cycles at 900 mA/g-P.

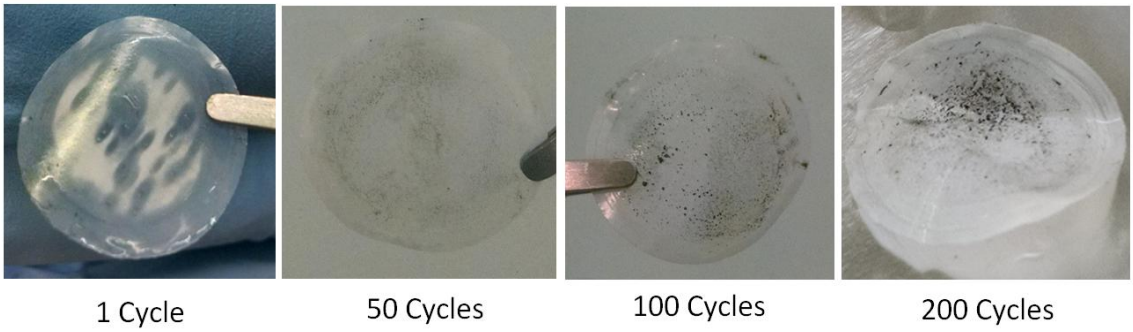

Figure 80. Pictures of the separator after different numbers of charge/discharge cycling.

Figure 80 shows how particles of the P-C/PAA/CNT electrode detached from the electrode, and were observed attached on the separator with increased charge/discharge cycling. To confirm that this was indeed particles of the electrode, SEM and EDS were performed on the electrode, and representative images are shown in Figure 81. After 1 cycle, small areas of Al could be detected via EDS through the P-C electrode in many

areas due to the low mass loading of the electrode. However, after 200 cycles, small areas of Al could not be observed, most likely due to thick SEI growth. Instead, large areas were observed where a large particle of P-C composite most likely fell out, leaving a crater through which Al could be observed.

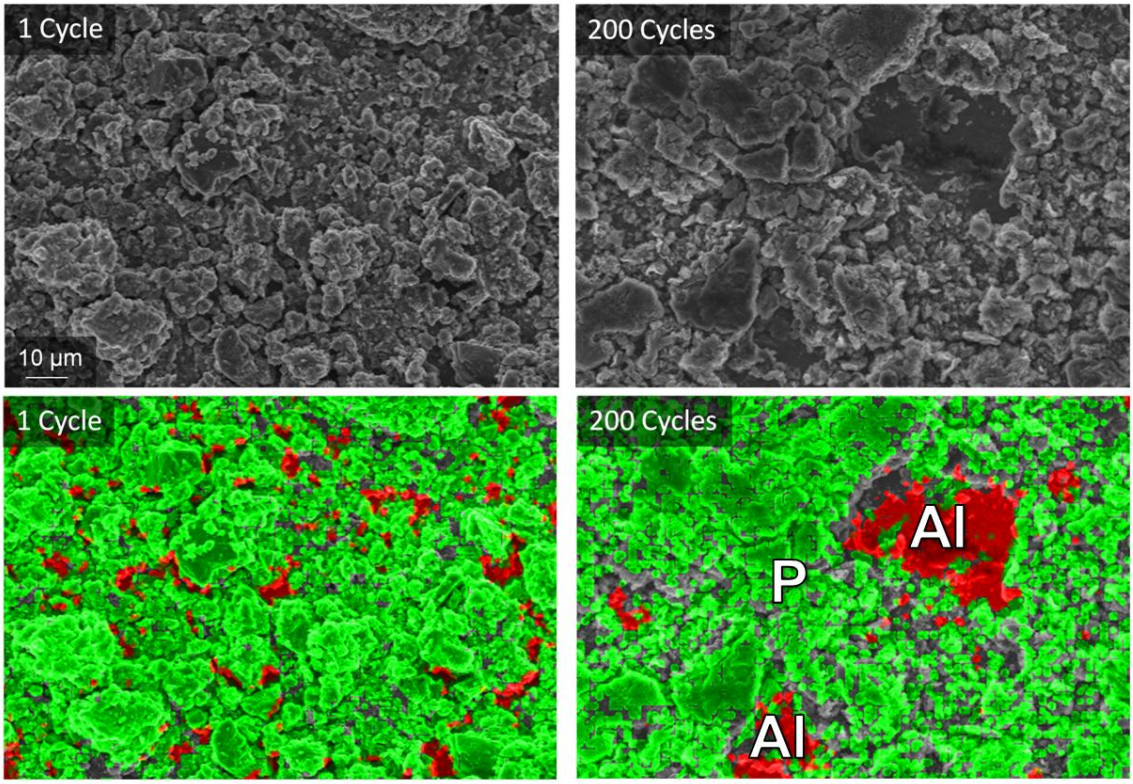

Figure 81. SEM of electrodes cycled for 1 cycle and 200 charge/discharge cycles and their EDS map overlays with P in green and Al in red.

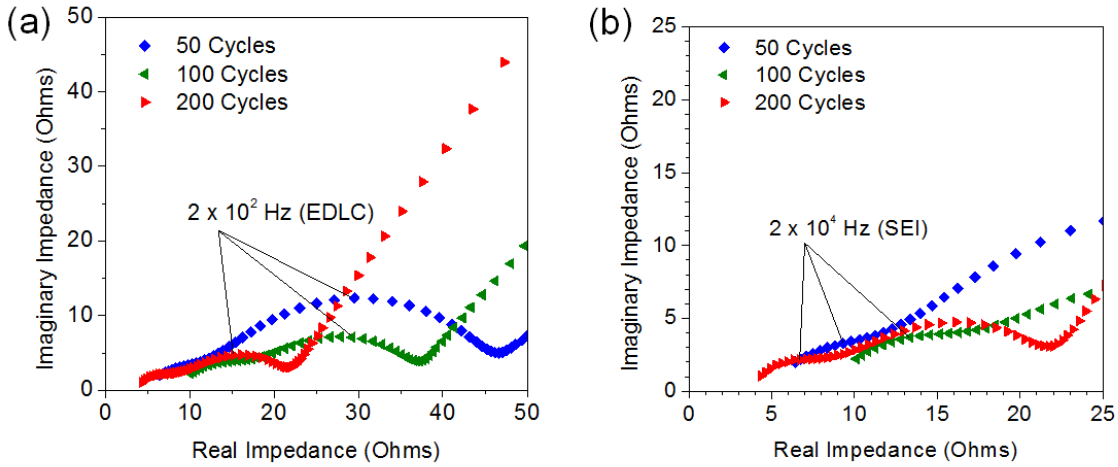

Figure 82. EIS spectra of the cells after charge/discharge cycling.

Figure 82 show the EIS spectra of the cells after cycling, through which 2 semicircles were identified with maximum imaginary impedance at approximately 200 Hz and 20,000 Hz. The two semicircles were assigned to the EDLC and SEI respectively based on their frequencies. While the SEI semicircle increases in size, the EDLC semicircle can clearly be seen to be decreasing in size with cycling. Lower capacitance is most likely due to the loss of electrical contact with particles, decreasing the gross area of the active electrode. On the other hand, the SEI impedance grows due to a continuously growing SEI layer.

10.5. Conclusion

P-C composite anodes were constructed using PB, ExG, and CNT for the carbon conductive additive and PAA and PVDF for the binder. Combined, these studies show that PAA/CNT electrodes perform well due to their enhanced mechanical properties, but that mechanical loss of electrical contact is still the dominant failure mode. Thorough drying, heating the electrodes in vacuum to at least 120 °C was found to be critical to

achieve good mechanical strength and hardness for PAA. For CNTs, sonication for good dispersion in the slurry was found to be critical for their effectiveness in improving cycle stability. A combination of ExG and PB could theoretically balance the low porosity and thus high ionic impedance of PB and the low surface area (for the binder to bond) and thus lower mechanical property of ExG. This in fact, is what is generally done in industry, but is foregone for many academic studies due to the difficulty in finding a good balance. We hypothesize however, that CNTs would still result in superior cycle stability due to their superior mechanical strength.

Even so, the P-C/PAA/CNT electrode still failed due to the loss of electrical contact. We hypothesized that this was due to the cracking of large particles. After 200 cycles, the electrodes appeared visually to be in tact (Figure 74) as opposed to the electrodes where CNTs were not well dispersed (Figure 81). Thus it appears that the particles are kept together due to a web of CNTs, but are electrically isolated due to the growth of SEI. Thus any further improvements of the phosphorus electrode's cycle stability may require a different synthesis approach of the P-C composite particles themselves.

Chapter 11. Conclusions and Recommendations

This thesis covered both the use of XPS in studying cell degradation and SEI formation, and the influences of the various components of the phosphorus anodes and processing methods. XPS analysis was enriched by many complementary analyses, showing how the SEI growth drove cell degradation. In the case of the LiFSI/DME chemistry, XPS was used to gain insights into the novel SEI chemistry.

Phosphorus anodes were constructed by ball milling phosphorus for extended periods of time, resulting in nanocrystalline phosphorus-carbon composites. These electrodes benefited greatly from carbon nanotubes providing good electrical contacts and mechanical stability to the electrode. The adhesion of the PAA and the dispersion of the carbon nanotubes in the slurry were found to be critical in constructing a well performing phosphorus anode. However, even with these improvements, the stability of the electrode was still hindered by the fracturing of large particles. To extend the cycle stability of phosphorus anodes further, studies are necessary to understand the lithation/delithiation mechanism of phosphorus, and how different allotropes and morphologies can be taken advantage of utilizing different synthesis methods. These studies are already underway at the moment, and will be published in future journal publications.

Li-ion battery chemistry still has much that is unexplored, untried, and unknown. By understanding the degradation mechanisms and material interactions, new electrode architectures and battery chemistries can be proposed and attempted. It is the authors hope that the work herein will be built upon in the context of the vast efforts being put into Li-ion batteries to develop new and better energy storage technologies of the future.

Appendix A. Ion beam etch rates

Table 15 shows qualitative data on the relative etch rates of various materials. As can be seen, the etch rate can vary significantly depending on the crystal direction. Ion beam etching in XPS also proceeds at a much slower rate than shown due to the large area, low voltage, and low current.

Table 15. Relative ion beam etch rates of various materials [194].

Material	Etch Rate (A/min)	Material	Etch Rate (A/min)
Ag	1050	**$Ni_{80}Fe_2O$**	292
Al	373	**NiCr**	309
Al_2O_3	48	**Os**	292
Au	630	**Pb**	1517
AZ 1350	117	**PbTe**	2199
Be	76	**Pd**	642
Bi	5133	**Pt**	362
C	64	**PZT Ceramic**	62
CdS	1283	**Rb**	2333
Co	262	**Re**	303
Cr	309	**Rh**	420
Cu	513	**Riston 14**	146
Fe	204	**Ru**	356
GaAs (100)	379	**Sb**	1889
GaAs (110)	933	**Si**	216
GaP (111)	927	**SiC**	204
GaPb (111)	1091	**SiO_2**	192
Ge	537	**Sn**	700
Hf	385	**Soda Glass**	117
InSb	887	**Ta**	245
Ir	344	**Ta_2O_5**	350
$LiNbO_3$	227	**TaC**	87
Mg	131	**TaN**	233
Mn	507	**Ti**	192
Mo	239	**V**	181
Mo_2C	163	**W**	198
Nb	274	**Y**	554
Ni	309	**Zr**	332

Appendix B. Post-mortem TEM of NMC surface

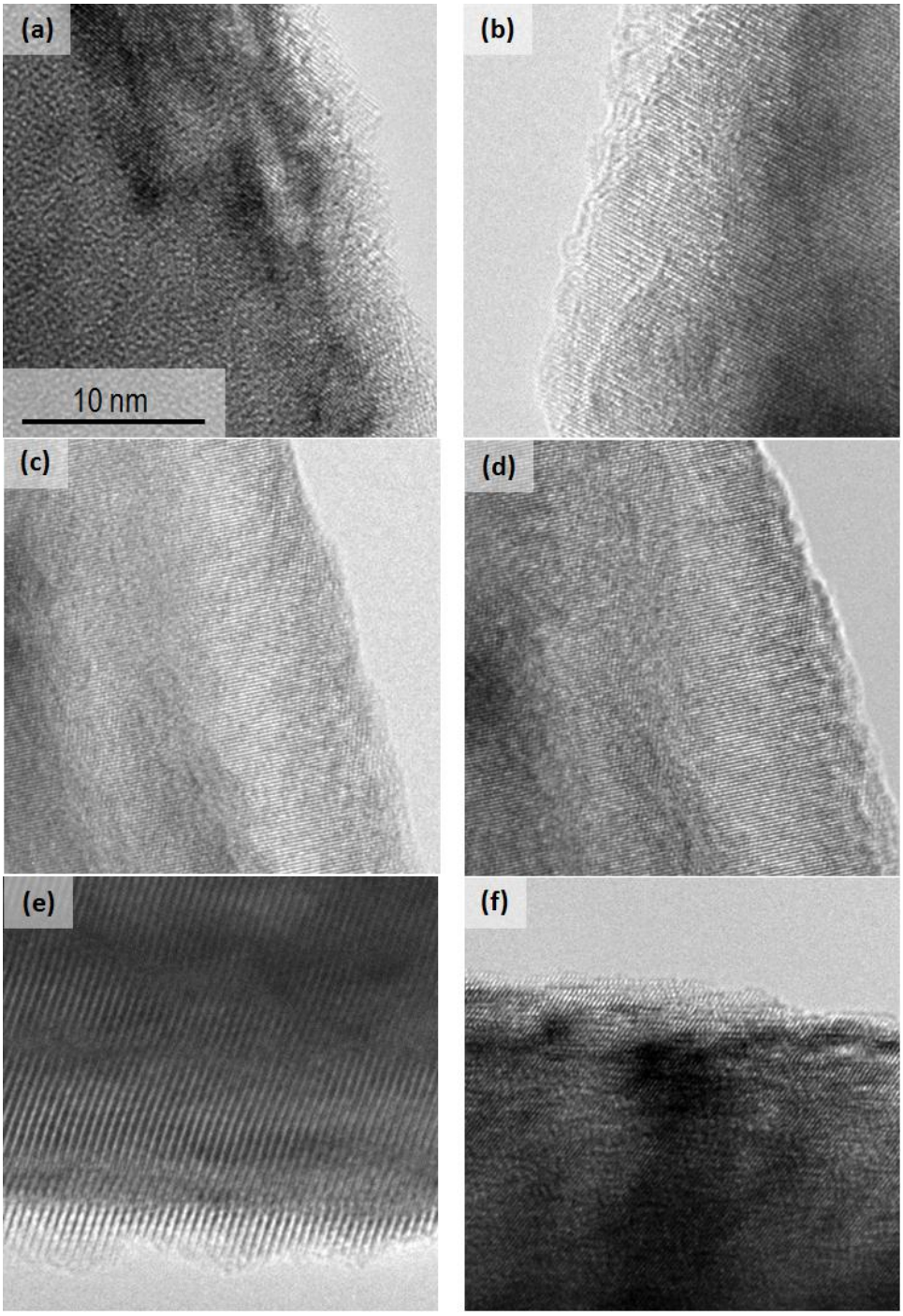

Figure 83. TEM of Fresh NMC powder from electrode (Section 6.3.2) showing crystallinity to the very edge of the particle. (a,b) Particle 1 (c,d) Particle 2 (e) Particle 3 (f) Particle 4.

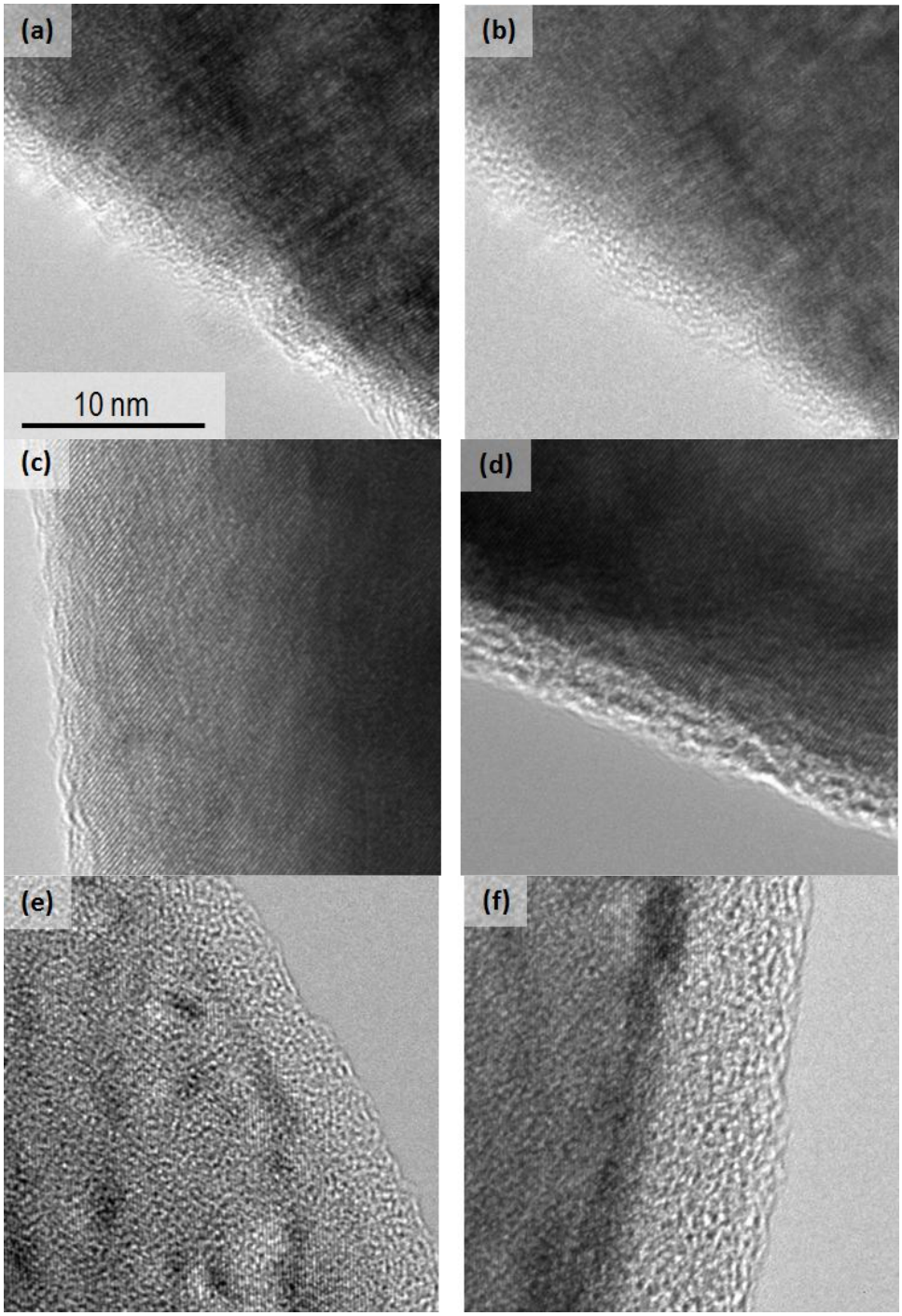

Figure 84. TEM of 3200 hour aged NMC powder from electrode (Section 6.3.2) showing amorphous layer on surface of electrode. (a,b) Particle 1 (c,d) Particle 2 (e,f) Particle 3.

Appendix C. XPS Spectra Fits of Aged Commercial Battery Electrodes

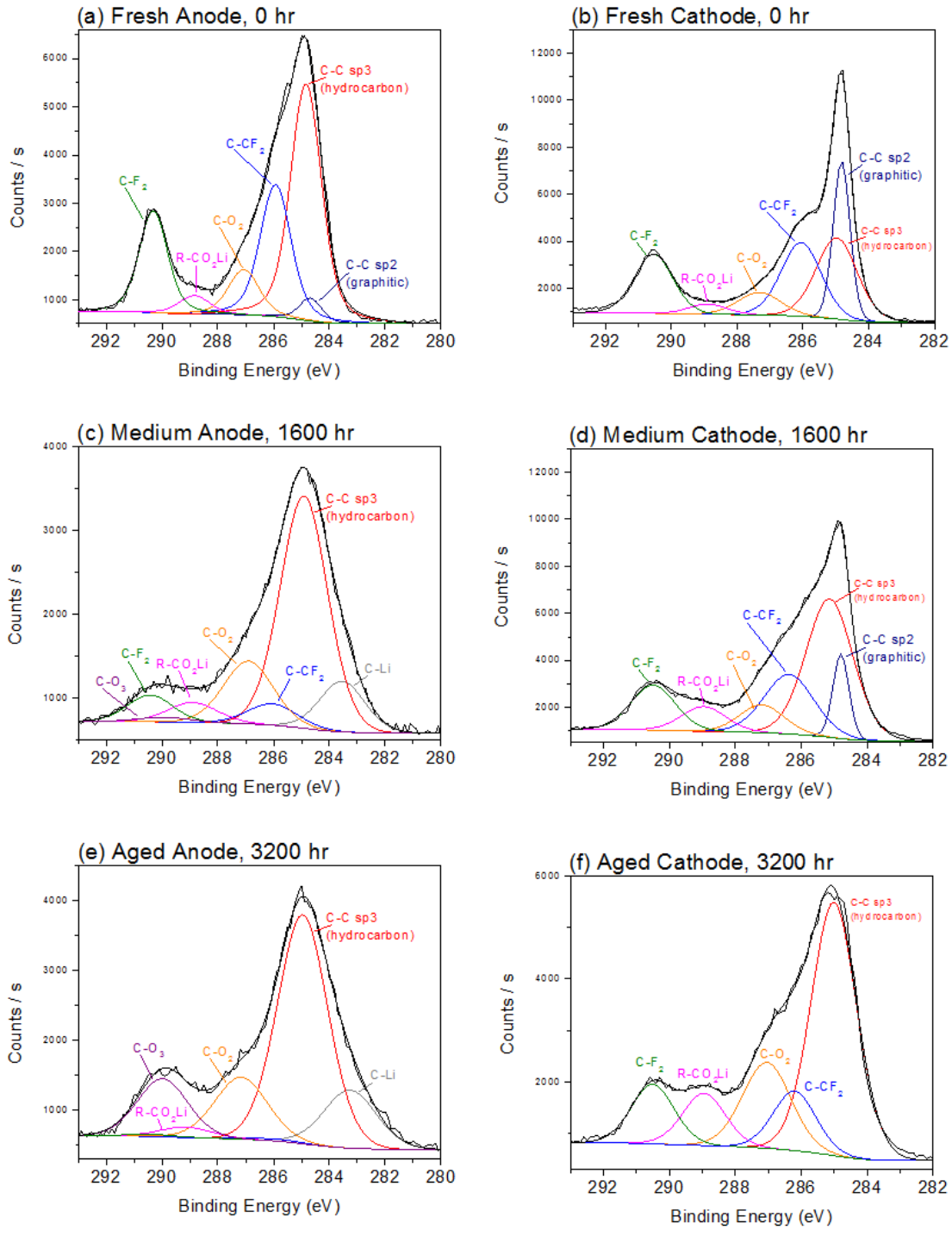

Figure 85. Fit details of the XPS C1 spectra for the anode (a,c,e) and cathode (b,d,f) of the fresh (a,b), 1600 hour (c,d), and 3200 hour (e,f) cells.

Appendix D. XPS Detection Limit

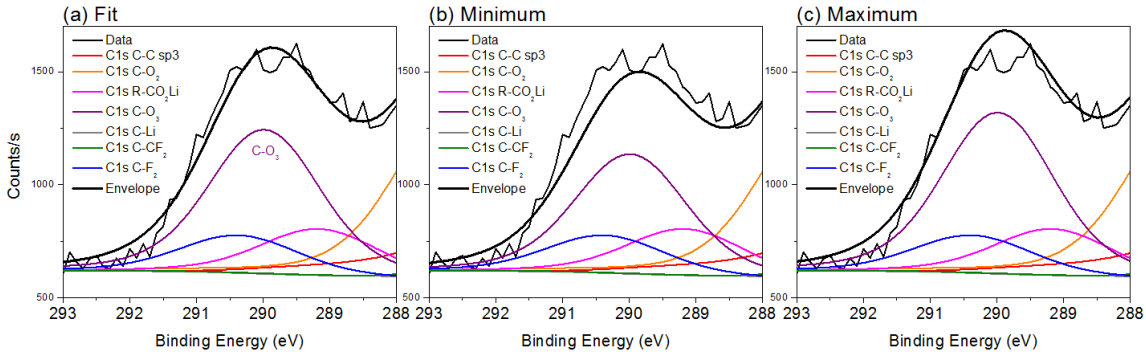

Figure 86. Comparison of the XPS C1s spectrum fit of the aged anode sample (i.e. 3200 hours, from Chapter 6.3.3), varying the peak height of the C-O_3 peak (a) to minimize the residual error, (b) to fit the minimum of the noise at the peak, and (c) to fit the maximum of the noise at the peak.

The noise in XPS data makes differences below ~1% atomic composition insignificant. As an example, the C-O_3 peak in the C1s spectrum of the aged sample from Chapter 6.3.3 is shown in Figure 86. The fitted data has been shown in comparison to adjustments of the C-O_3 peak to align with the maximum and minimum of the noise. The fitted spectrum in Figure 86a results in 3.9% atomic composition, while the minimum (Figure 86b) and minimum (Figure 86c) results in 3.42% and 4.30% respectively. While the fit envelope (the sum of all the peaks, Figure 86a) passes through the center of the noise for most of the spectrum, it is visible that this is not always true in the vicinity of ~292 eV binding energy, where it overshoots. It should be noted however, that if there is no peak overlap, elements can still be detected, although not quantified below this limit. Unfortunately, in the case of the C1s sp2 graphitic peak, there is heavy overlap with the C1s sp3 hydrocarbon peak, and thus adjustments in the neighboring peaks also have a large contribution to the error.

Appendix E. XPS Spectra Fits of Sulfonimide Electrolyte SEI

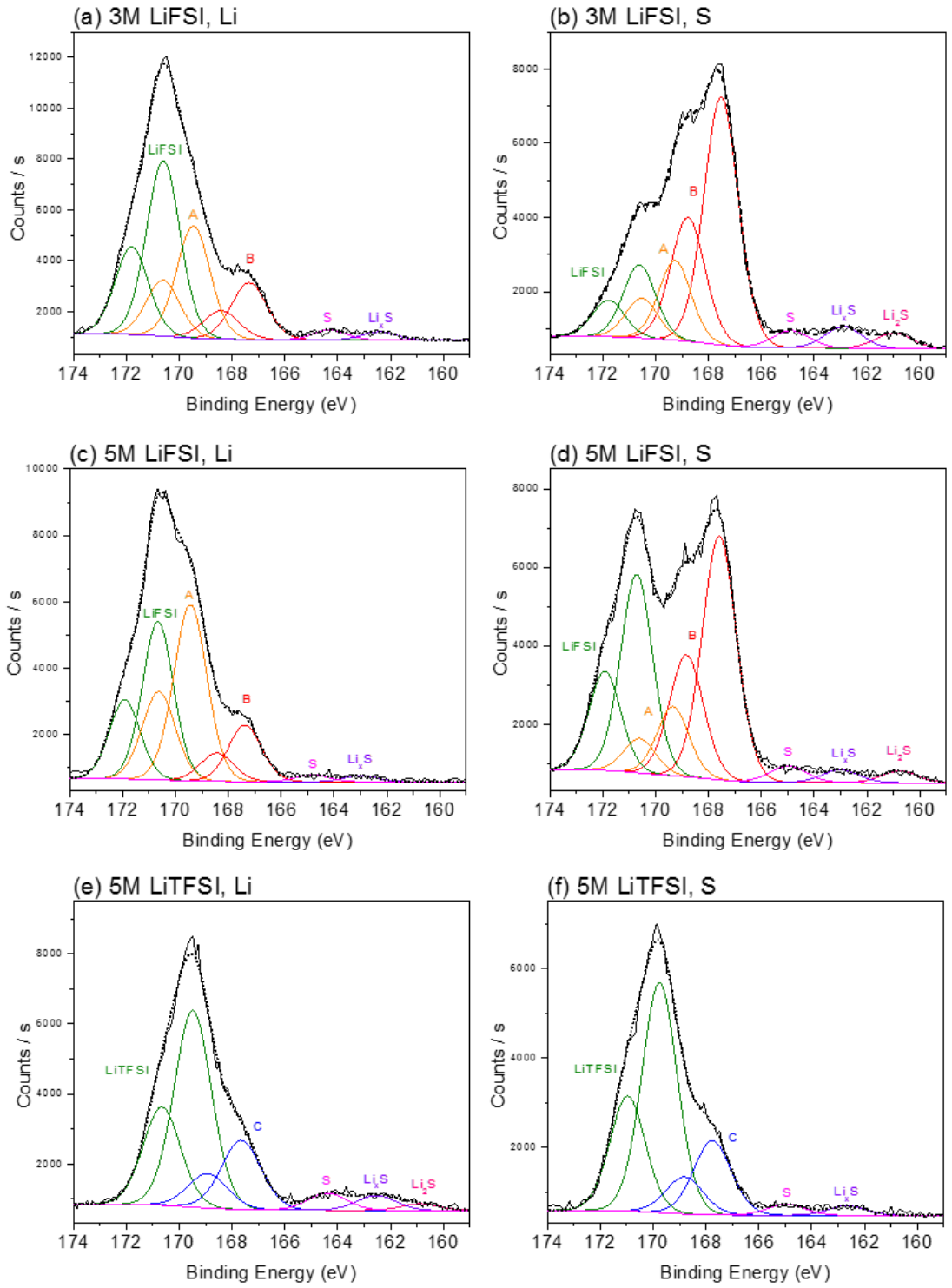

Figure 87. XPS S2p Spectra of Li anode (a,c,e) and S cathode (b,d,f) for cells with 3M LiFSI (a,b), 5M LiFSI (c,d), and 5M LiTFSI (e,f) salts.

Appendix F. Contribution of carbon to capacity

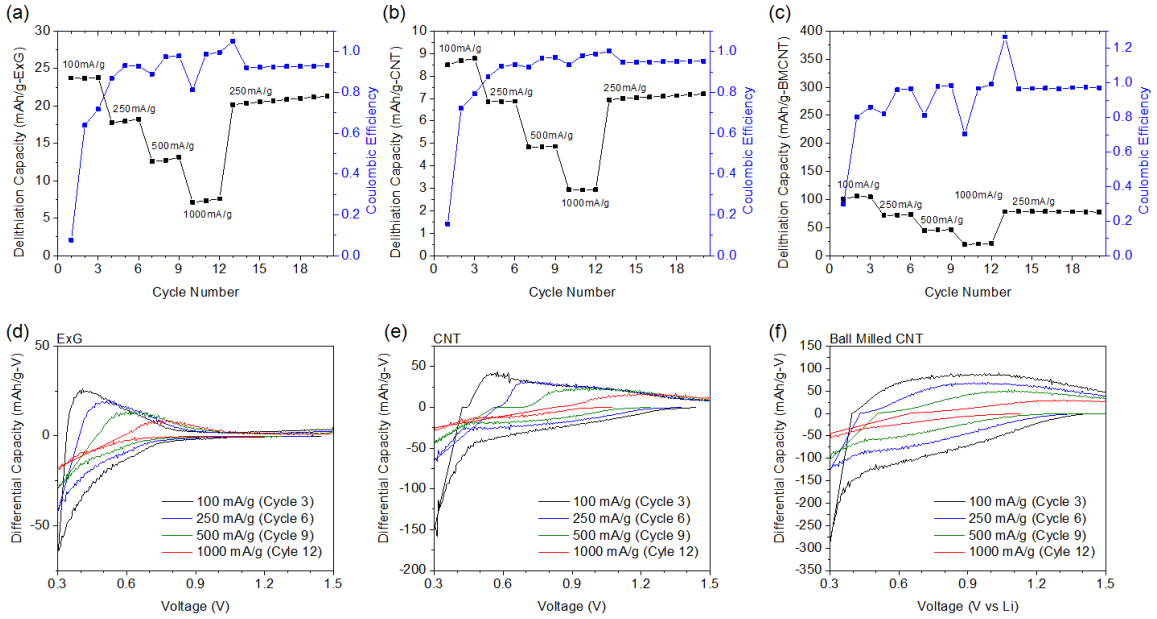

Figure 88. Rate test (a-c) cycle capacity and (d-f) differential capacity data for (a,d) ExG, (b,e) CNT, and (c,f) CNT balled milled for 24 hours. Cells were made with 10 wt. % PAA on Al current collectors, and cycled between 0.3-1.5V. Based on the capacities observed, the carbons did not have a significant contribution to lithium capacity in phosphorus electrodes except for the first cycle irreversible capacity.

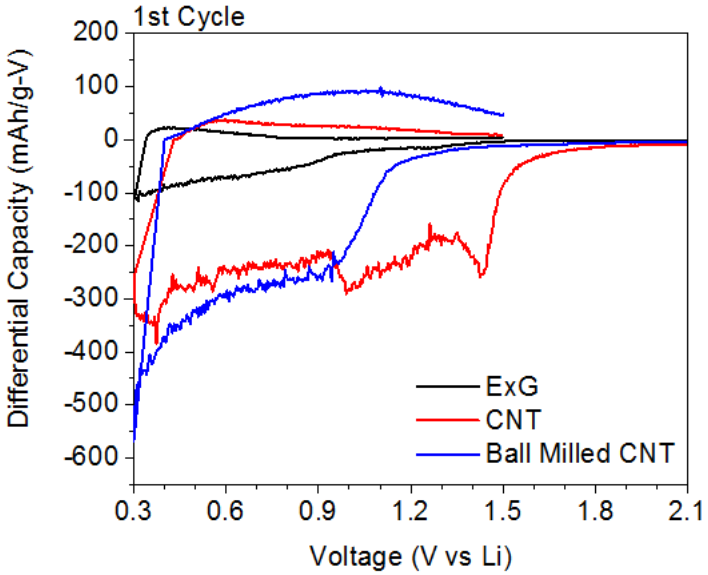

Figure 89. First cycle differential capacity plots of carbon electrodes cycled in Figure 88, at 100 mA/g rate, showing the irreversible capacity of the different carbons.

Appendix G. Drying of polymer films

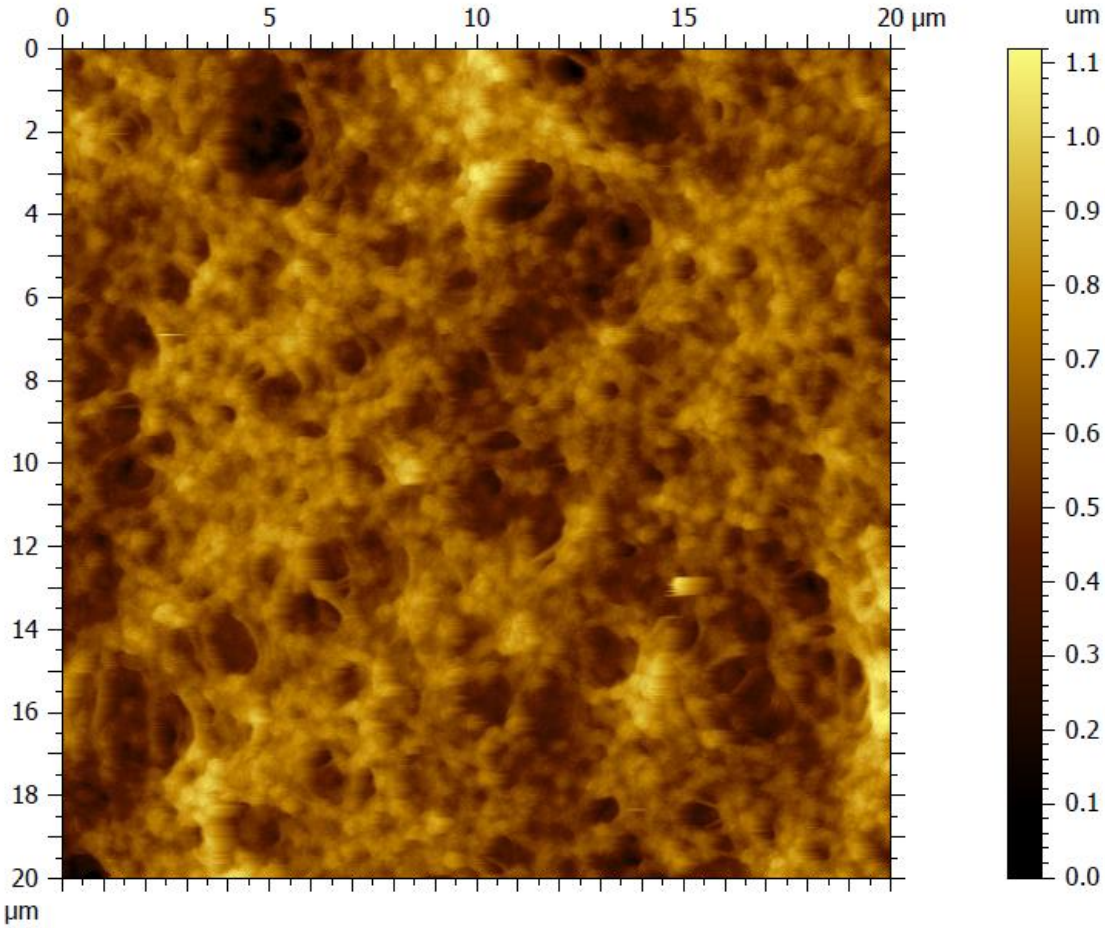

Figure 90. AFM image of PVDF film dried at 70 °C, showing a porous structure.

REFERENCES

1 Xu, W. *et al.* Lithium metal anodes for rechargeable batteries. *Energy & Environmental Science* **7**, 513-537, doi:10.1039/c3ee40795k (2014).

2 Harry, K. J., Hallinan, D. T., Parkinson, D. Y., MacDowell, A. A. & Balsara, N. P. Detection of subsurface structures underneath dendrites formed on cycled lithium metal electrodes. *Nat. Mater.* **13**, 69-73, doi:10.1038/nmat3793

3 Steiger, J., Richter, G., Wenk, M., Kramer, D. & Mönig, R. Comparison of the growth of lithium filaments and dendrites under different conditions. *Electrochem. Commun.* **50**, 11-14, doi:http://dx.doi.org/10.1016/j.elecom.2014.11.002 (2015).

4 Nitta, N., Wu, F., Lee, J. T. & Yushin, G. Li-ion battery materials: present and future. *Mater. Today* **18**, 252-264, doi:http://dx.doi.org/10.1016/j.mattod.2014.10.040 (2015).

5 Nitta, N. & Yushin, G. High-Capacity Anode Materials for Lithium-Ion Batteries: Choice of Elements and Structures for Active Particles. *Particle & Particle Systems Characterization* **31**, 317-336, doi:10.1002/ppsc.201300231 (2014).

6 Lux, S. F., Chevalier, J., Lucas, I. T. & Kostecki, R. HF Formation in LiPF6-Based Organic Carbonate Electrolytes. *ECS Electrochemistry Letters* **2**, A121-A123, doi:10.1149/2.005312eel (2013).

7 Basin, V. E. Advances in understanding the adhesion between solid substrates and organic coatings. *Progress in Organic Coatings* **12**, 213-250, doi:http://dx.doi.org/10.1016/0033-0655(84)80010-2 (1984).

8 Chen, Z., Christensen, L. & Dahn, J. R. Large-volume-change electrodes for Li-ion batteries of amorphous alloy particles held by elastomeric tethers. *Electrochemistry Communications* **5**, 919-923, doi:http://dx.doi.org/10.1016/j.elecom.2003.08.017 (2003).

9 Chen, Z., Christensen, L. & Dahn, J. R. Comparison of PVDF and PVDF-TFE-P as Binders for Electrode Materials Showing Large Volume Changes in Lithium-Ion Batteries. *Journal of The Electrochemical Society* **150**, A1073-A1078, doi:10.1149/1.1586922 (2003).

10 Li, J., Lewis, R. B. & Dahn, J. R. Sodium Carboxymethyl Cellulose: A Potential Binder for Si Negative Electrodes for Li-Ion Batteries. *Electrochemical and Solid-State Letters* **10**, A17-A20, doi:10.1149/1.2398725 (2007).

11 Magasinski, A. *et al.* Toward Efficient Binders for Li-Ion Battery Si-Based Anodes: Polyacrylic Acid. *ACS Appl. Mater. Interfaces* **2**, 3004-3010, doi:10.1021/am100871y (2010).

12 Kovalenko, I. *et al.* A Major Constituent of Brown Algae for Use in High-Capacity Li-Ion Batteries. *Science* **334**, 75-79, doi:10.1126/science.1209150 (2011).

13 Hochgatterer, N. S. *et al.* Silicon/graphite composite electrodes for high-capacity anodes: Influence of binder chemistry on cycling stability. *Electrochemical and Solid State Letters* **11**, A76-A80, doi:10.1149/1.2888173 (2008).

14 Komaba, S. *et al.* Comparative Study of Sodium Polyacrylate and Poly(vinylidene fluoride) as Binders for High Capacity Si-Graphite Composite Negative Electrodes in Li-Ion Batteries. *J. Phys. Chem. C* **116**, 1380-1389, doi:10.1021/jp204817h (2012).

15 Kovalenko, I. *et al.* A Major Constituent of Brown Algae for Use in High-Capacity Li-Ion Batteries. *Science* **333**, 75-79, doi:10.1126/science.1209150 (2011).

16 Hildebrand, J. H. SOLUBILITY. *J. Am. Chem. Soc.* **38**, 1452-1473, doi:10.1021/ja02265a002 (1916).

17 Hildebrand, J. H. SOLUBILITY. III. RELATIVE VALUES OF INTERNAL PRESSURES AND THEIR PRACTICAL APPLICATION. *J. Am. Chem. Soc.* **41**, 1067-1080, doi:10.1021/ja02228a004 (1919).

18 Scatchard, G. Equilibria in Non-electrolyte Solutions in Relation to the Vapor Pressures and Densities of the Components. *Chem. Rev.* **8**, 321-333, doi:10.1021/cr60030a010 (1931).

19 Hildebrand, J. H. & Scott, R. L. *The Solubility of Nonelectrolytes*. 3rd edn, (Reinhold Publishing Corporation, 1950).

20 Hansen, C. M. *Hansen Solubility Parameters, A User's Handbook.* (CRC Press LLC, 2000).

21 *Surface Tension, Hansen Solubility Parameters, Molar Volume, Enthalpy of Evaporation, and Molecular Weight of Selected Liquids*, <https://www.accudynetest.com/solubility_table.html> (2016).

22 Polymer Solutions - Solvents and Solubility Parameters Viscosity. 46-49 (Sigma-Aldrich).

23 Etacheri, V., Marom, R., Elazari, R., Salitra, G. & Aurbach, D. Challenges in the development of advanced Li-ion batteries: a review. *Energy & Environmental Science* **4**, 3243-3262, doi:10.1039/C1EE01598B (2011).

24 Smart, M. C., Ratnakumar, B. V. & Surampudi, S. Electrolytes for Low- Temperature Lithium Batteries Based on Ternary Mixtures of Aliphatic Carbonates. *Journal of The Electrochemical Society* **146**, 486-492, doi:10.1149/1.1391633 (1999).

25 Xu, K. Nonaqueous Liquid Electrolytes for Lithium-Based Rechargeable Batteries. *Chemical Reviews* **104**, 4303-4418, doi:10.1021/cr030203g (2004).

26 Rodríguez, A., Canosa, J., Domínguez, A. & Tojo, J. Viscosities of Dimethyl Carbonate or Diethyl Carbonate with Alkanes at Four Temperatures. New UNIFAC−VISCO Parameters. *Journal of Chemical & Engineering Data* **48**, 146-151, doi:10.1021/je020131a (2003).

27 1,3-Dioxolane. (2013). <http://www.standort-ludwigshafen.basf.de/group/corporate/site-ludwigshafen/en/literature-document:/Sales+Products+Dioxolane-Brochure--1+3+Dioxolane-English.pdf>.

28 Myers, B. J. (ed ACS Division of Organic Chemistry) (2016).

29 Henni, A., Naami, A. & Tontiwachwuthikul, P. Densities, Viscosities, and Derived Functions of Binary Mixtures: (Triethylene Glycol Dimethyl Ether + Water) and (N-Acetylmorpholine + Water) from 298.15 K to 343.15 K. *Journal of Chemical & Engineering Data* **50**, 1038-1042, doi:10.1021/je050021e (2005).

30 Tang, S. & Zhao, H. Glymes as versatile solvents for chemical reactions and processes: from the laboratory to industry. *RSC Advances* **4**, 11251-11287, doi:10.1039/C3RA47191H (2014).

31 Ein-Eli, Y., McDevitt, S. F. & Laura, R. The Superiority of Asymmetric Alkyl Methyl Carbonates. *Journal of The Electrochemical Society* **145**, L1-L3, doi:10.1149/1.1838196 (1998).

32 Li, B. *et al.* Properties of solid electrolyte interphase formed by prop-1-ene-1,3-sultone on graphite anode of Li-ion batteries. *Electrochimica Acta* **105**, 1-6, doi:http://dx.doi.org/10.1016/j.electacta.2013.04.142 (2013).

33 Aurbach, D., Markovsky, B., Weissman, I., Levi, E. & Ein-Eli, Y. On the correlation between surface chemistry and performance of graphite negative electrodes for Li ion batteries. *Electrochim. Acta* **45**, 67-86, doi:10.1016/s0013-4686(99)00194-2 (1999).

34 Dahbi, M., Ghamouss, F., Tran-Van, F., Lemordant, D. & Anouti, M. Comparative study of EC/DMC LiTFSI and LiPF6 electrolytes for electrochemical storage. *Journal of Power Sources* **196**, 9743-9750, doi:http://dx.doi.org/10.1016/j.jpowsour.2011.07.071 (2011).

35 Nishida, T., Nishikawa, K. & Fukunaka, Y. Diffusivity Measurement of LiPF6, LiTFSI, LiBF4 in PC. *ECS Transactions* **6**, 1-14, doi:10.1149/1.2831921 (2008).

36 Zinigrad, E., Larush-Asraf, L., Gnanaraj, J. S., Sprecher, M. & Aurbach, D. On the thermal stability of LiPF6. *Thermochimica Acta* **438**, 184-191, doi:http://dx.doi.org/10.1016/j.tca.2005.09.006 (2005).

37 Sloop, S. E., Pugh, J. K., Wang, S., Kerr, J. B. & Kinoshita, K. Chemical Reactivity of PF 5 and LiPF6 in Ethylene Carbonate/Dimethyl Carbonate Solutions. *Electrochemical and Solid-State Letters* **4**, A42-A44, doi:10.1149/1.1353158 (2001).

38 Lu, Z., Yang, L. & Guo, Y. Thermal behavior and decomposition kinetics of six electrolyte salts by thermal analysis. *Journal of Power Sources* **156**, 555-559, doi:http://dx.doi.org/10.1016/j.jpowsour.2005.05.085 (2006).

39 Yamamoto, O. *et al.* Proceedings of the Eighth International Meeting on Lithium BatteriesCorrosion of aluminum at high voltages in non-aqueous electrolytes containing perfluoroalkylsulfonyl imides; new lithium salts for lithium-ion cells. *J. Power Sources* **68**, 320-325, doi:http://dx.doi.org/10.1016/S0378-7753(97)02517-2 (1997).

40 Bolloli, M. *et al.* Fluorinated Carbamates as Suitable Solvents for LiTFSI-Based Lithium-Ion Electrolytes: Physicochemical Properties and Electrochemical Characterization. *The Journal of Physical Chemistry C* **119**, 22404-22414, doi:10.1021/acs.jpcc.5b07514 (2015).

41 Zhang, X. & Devine, T. M. Passivation of Aluminum in Lithium-Ion Battery Electrolytes with LiBOB. *J. Electrochem. Soc.* **153**, B365-B369, doi:10.1149/1.2218269 (2006).

42 Bloom, I., Christophersen, J. & Gering, K. Differential Voltage Analysis of High Power Lithium Ion Cells. *Meeting Abstracts* **MA2005-02**, 241 (2006).

43 Verma, P., Maire, P. & Novak, P. A review of the features and analyses of the solid electrolyte interphase in Li-ion batteries. *Electrochim. Acta* **55**, 6332-6341, doi:10.1016/j.electacta.2010.05.072 (2010).

44 Dubarry, M., Truchot, C. & Liaw, B. Y. Synthesize battery degradation modes via a diagnostic and prognostic model. *J. Power Sources* **219**, 204-216, doi:http://dx.doi.org/10.1016/j.jpowsour.2012.07.016 (2012).

45 Araki, K. & Sato, N. Chemical transformation of the electrode surface of lithium-ion battery after storing at high temperature. *J. Power Sources* **124**, 124-132, doi:http://dx.doi.org/10.1016/S0378-7753(03)00593-7 (2003).

46 Abraham, D. P., Spila, T., Furczon, M. M. & Sammann, E. Evidence of Transition-Metal Accumulation on Aged Graphite Anodes by SIMS. *Electrochemical and Solid State Letters* **11**, A226-A228, doi:10.1149/1.2987680 (2008).

47 Philippe, B. *et al.* Role of the LiPF6 Salt for the Long-Term Stability of Silicon Electrodes in Li-Ion Batteries – A Photoelectron Spectroscopy Study. *Chem. Mater.* **25**, 394-404, doi:10.1021/cm303399v (2013).

48 El Ouatani, L. *et al.* Surface film formation on a carbonaceous electrode: Influence of the binder chemistry. *J. Power Sources* **189**, 72-80, doi:http://dx.doi.org/10.1016/j.jpowsour.2008.11.031 (2009).

49 Choi, N.-S., Han, J.-G., Ha, S.-Y., Park, I. & Back, C.-K. Recent advances in the electrolytes for interfacial stability of high-voltage cathodes in lithium-ion batteries. *RSC Advances* **5**, 2732-2748, doi:10.1039/c4ra11575a (2015).

50 Garay, A. L., Pichon, A. & James, S. L. Solvent-free synthesis of metal complexes. *Chem. Soc. Rev.* **36**, 846-855, doi:10.1039/b600363j (2007).

51 Suryanarayana, C. Mechanical alloying and milling. *Prog. Mater Sci.* **46**, 1-184, doi:http://dx.doi.org/10.1016/S0079-6425(99)00010-9 (2001).

52 Koch, C. C. Materials Synthesis by Mechanical Alloying. *Annu. Rev. Mater. Sci.* **19**, 121-143, doi:10.1146/annurev.ms.19.080189.001005 (1989).

53 Shen, T. D. *et al.* The structure and property characteristics of amorphous/nanocrystalline silicon produced by ball milling. *J. Mater. Res.* **10**, 139-148, doi:doi:10.1557/JMR.1995.0139 (1995).

54 Indris, S., Bork, D. & Heitjans, P. Nanocrystalline Oxide Ceramics Prepared by High-Energy Ball Milling. *J. Mater. Synth. Process.* **8**, 245-250, doi:10.1023/a:1011324429011 (2000).

55 Milev, A., Wilson, M., Kannangara, G. S. K. & Tran, N. X-ray diffraction line profile analysis of nanocrystalline graphite. *Mater. Chem. Phys.* **111**, 346-350, doi:http://dx.doi.org/10.1016/j.matchemphys.2008.04.024 (2008).

56 Francke, M., Hermann, H., Wenzel, R., Seifert, G. & Wetzig, K. Modification of carbon nanostructures by high energy ball-milling under argon and hydrogen atmosphere. *Carbon* **43**, 1204-1212, doi:http://dx.doi.org/10.1016/j.carbon.2004.12.013 (2005).

57 Motozuka, S. *et al.* Effective preparation of graphite nanoparticles using mechanochemical solid-state reactions. *Solid State Commun.* **190**, 28-32, doi:http://dx.doi.org/10.1016/j.ssc.2014.03.023 (2014).

58 Milev, A., Tran, N., Kamali Kannangara, G. S. & Wilson, M. Influence of bond defects on coiling of graphite. *Science and Technology of Advanced Materials* **7**, 834-838, doi:http://dx.doi.org/10.1016/j.stam.2006.11.010 (2006).

59 Han, S. H., Gschneidner, K. A. & Beaudry, B. J. Preparation of a metastable high temperature phase (γ-Dy2S3) and a metastable high pressure phase (γ-Y2S3) by mechanical alloying and mechanical milling. *Scr. Metall. Mater.* **25**, 295-298, doi:http://dx.doi.org/10.1016/0956-716X(91)90181-Y (1991).

60 Ohtani, T., Motoki, M., Koh, K. & Ohshima, K. Synthesis of binary copper chalcogenides by mechanical alloying. *Mater. Res. Bull.* **30**, 1495-1504, doi:http://dx.doi.org/10.1016/0025-5408(95)00155-7 (1995).

61 Sen, S., Ram, M. L., Roy, S. & Sarkar, B. K. The structural transformation of anatase TiO 2 by high-energy vibrational ball milling. *J. Mater. Res.* **14**, 841-848 (1999).

62 Oliver, W. C. & Pharr, G. M. An improved technique for determining hardness and elastic modulus using load and displacement sensing indentation experiments. *J. Mater. Res.* **7**, 1564-1583, doi:doi:10.1557/JMR.1992.1564 (1992).

63 Zhou, W., Apkarian, R., Wang, Z. L. & Joy, D. in *Scanning Microscopy for Nanotechnology, Techniques and Applications* (eds Weilie Zhou & Zhong Lin Wang) Ch. 1, 1-40 (Springer New York, 2007).

64 Krumeich, F. 24 (Laboratory of Inorganic Chemistry, ETH Zurich, Zurich).

65 Frey, M. D. in *Scanning Microscopy for Nanotechnology, Techniques and Applications* (eds Weilie Zhou & Zhong Lin Wang) Ch. 4, 101-119 (Springer New York, 2007).

66 Williams, D. B. & Carter, C. B. *Transmission Electron Microscopy, A Textbook for Materials Science*. Second edn, 7 (Springer, 2009).

67 Muso. in *Wikimedia Commons* (2007).

68 Shindo, D. & Oikawa, T. in *Analytical Electron Microscopy for Materials Science* (Springer, 2002).

69 (ed Oxford Instruments) (Oxford Instruments, 2013).

70 Berlin, J. Analysis of Boron with Energy Dispersive X-ray Spectrometry; Advances in Light Element Analysis with SDD Technology. 19-21 (Bruker, 2011).

71 Mogk, D. W. *Time-of-Flight Secondary Ion Mass Spectrometry (ToF-SIMS),* <http://serc.carleton.edu/research_education/geochemsheets/techniques/ToFSIMS.html> (

72 Fulvio314. (Wikimedia Commons, 2013).

73 ATR – Theory and Applications. (PIKE Technologies, 2011).

74 Hydrargyrum. (Wikimedia Commons, 2011).

75 Briggs, D. *Surface analysis of polymers by XPS and static SIMS*. (Cambridge University Press, 1998).

76 Ning, X., Wang, Z. & Zhang, Z. Fermi Level shifting, Charge Transfer and Induced Magnetic Coupling at La0.7Ca0.3MnO3/LaNiO3 Interface. *Scientific Reports* **5**, 8460, doi:10.1038/srep08460

77 Barr, T. L. & Seal, S. Nature of the use of adventitious carbon as a binding energy standard. *Journal of Vacuum Science & Technology A* **13**, 1239-1246, doi:doi:http://dx.doi.org/10.1116/1.579868 (1995).

78 Shirley, D. A. High-Resolution X-Ray Photoemission Spectrum of the Valence Bands of Gold. *Physical Review B* **5**, 4709-4714 (1972).

79 Tougaard, S. Quantitative analysis of the inelastic background in surface electron spectroscopy. *Surface and Interface Analysis* **11**, 453-472, doi:10.1002/sia.740110902 (1988).

80 Végh, J. The Shirley background revised. *Journal of Electron Spectroscopy and Related Phenomena* **151**, 159-164, doi:http://dx.doi.org/10.1016/j.elspec.2005.12.002 (2006).

81 Estrade-Szwarckopf, H. XPS photoemission in carbonaceous materials: A "defect" peak beside the graphitic asymmetric peak. *Carbon* **42**, 1713-1721, doi:http://dx.doi.org/10.1016/j.carbon.2004.03.005 (2004).

82 Hufner, S. *Photoelectron Spectroscopy, Principles and Applications*. Third edn, (Springer, 2003).

83 Doniach, S. & Sunjic, M. Many-electron singularity in X-ray photoemission and X-ray line spectra from metals. *Journal of Physics C: Solid State Physics* **3**, 285 (1970).

84 Mahan, G. D. Collective excitations in x-ray spectra of metals. *Physical Review B* **11**, 4814-4824 (1975).

85 Kaciulis, S. Spectroscopy of carbon: from diamond to nitride films. *Surf. Interface Anal.* **44**, 1155-1161, doi:10.1002/sia.4892 (2012).

86 Edstrom, K., Herstedt, M. & Abraham, D. P. A new look at the solid electrolyte interphase on graphite anodes in Li-ion batteries. *J. Power Sources* **153**, 380-384, doi:10.1016/j.jpowsour.2005.05.062 (2006).

87 Andersson, A. M., Herstedt, M., Bishop, A. G. & Edström, K. The influence of lithium salt on the interfacial reactions controlling the thermal stability of graphite anodes. *Electrochimica Acta* **47**, 1885-1898, doi:http://dx.doi.org/10.1016/S0013-4686(02)00044-0 (2002).

88 Xiao, A., Yang, L., Lucht, B. L., Kang, S.-H. & Abraham, D. P. Examining the Solid Electrolyte Interphase on Binder-Free Graphite Electrodes. *J. Electrochem. Soc.* **156**, A318-A327, doi:10.1149/1.3078020 (2009).

89 Leroy, S., Martinez, H., Dedryvère, R., Lemordant, D. & Gonbeau, D. Influence of the lithium salt nature over the surface film formation on a graphite electrode in Li-ion batteries: An XPS study. *Appl. Surf. Sci.* **253**, 4895-4905, doi:http://dx.doi.org/10.1016/j.apsusc.2006.10.071 (2007).

90 Kim, H. *et al.* In Situ Formation of Protective Coatings on Sulfur Cathodes in Lithium Batteries with LiFSI-Based Organic Electrolytes. *Advanced Energy Materials* **5**, n/a-n/a, doi:10.1002/aenm.201401792 (2015).

91 Contarini, S. & Rabalais, J. W. Ion bombardment-induced decomposition of Li and Ba sulfates and carbonates studied by X-ray photoelectron spectroscopy. *Journal of Electron Spectroscopy and Related Phenomena* **35**, 191-201, doi:http://dx.doi.org/10.1016/0368-2048(85)80056-6 (1985).

92 Xu, K. *et al.* Syntheses and Characterization of Lithium Alkyl Mono- and Dicarbonates as Components of Surface Films in Li-Ion Batteries. *The Journal of Physical Chemistry B* **110**, 7708-7719, doi:10.1021/jp0601522 (2006).

93 Hamrin, K., Johansson, G., Gelius, U., Nordling, C. & Siegbahn, K. Valence Bands and Core Levels of the Isoelectronic Series LiF, BeO, BN, and Graphite Studied by ESCA. *Physica Scripta* **1**, 277 (1970).

94 Murch, G. E. & Thorn, R. J. Relation between orbital binding energies and ionicities in alkali and alkaline earth flourides. *Journal of Physics and Chemistry of Solids* **41**, 785-791, doi:http://dx.doi.org/10.1016/0022-3697(80)90088-8 (1980).

95 Louette, P., Bodino, F. & Pireaux, J.-J. Poly(acrylic acid) (PAA) XPS Reference Core Level and Energy Loss Spectra. *Surface Science Spectra* **12**, 22-26, doi:doi:http://dx.doi.org/10.1116/11.20050905 (2005).

96 Dedryvère, R. *et al.* Electrode/Electrolyte Interface Reactivity in High-Voltage Spinel LiMn1.6Ni0.4O4/Li4Ti5O12 Lithium-Ion Battery. *The Journal of Physical Chemistry C* **114**, 10999-11008, doi:10.1021/jp1026509 (2010).

97 Herstedt, M., Abraham, D. P., Kerr, J. B. & Edström, K. X-ray photoelectron spectroscopy of negative electrodes from high-power lithium-ion cells showing various levels of power fade. *Electrochimica Acta* **49**, 5097-5110, doi:http://dx.doi.org/10.1016/j.electacta.2004.06.021 (2004).

98 Bryngelsson, H., Stjerndahl, M., Gustafsson, T. & Edstrom, K. How dynamic is the SEI? *J. Power Sources* **174**, 970-975, doi:10.1016/j.jpowsour.2007.06.050 (2007).

99 Tasaki, K. *et al.* Solubility of Lithium Salts Formed on the Lithium-Ion Battery Negative Electrode Surface in Organic Solvents. *J. Electrochem. Soc.* **156**, A1019-A1027, doi:10.1149/1.3239850 (2009).

100 Kim, G.-H., Smith, K., Lee, K.-J., Santhanagopalan, S. & Pesaran, A. Multi-Domain Modeling of Lithium-Ion Batteries Encompassing Multi-Physics in Varied Length Scales. *J. Electrochem. Soc.* **158**, A955-A969, doi:10.1149/1.3597614 (2011).

101 Volkert, C. A. & Minor, A. M. Focused ion beam microscopy and micromachining. *MRS Bull.* **32**, 389-395, doi:10.1557/mrs2007.62 (2007).

102 Aurbach, D. & Gottlieb, H. THE ELECTROCHEMICAL-BEHAVIOR OF SELECTED POLAR AROTIC SYSTEMS. *Electrochim. Acta* **34**, 141-156, doi:10.1016/0013-4686(89)87079-3 (1989).

103 Ravdel, B. *et al.* Thermal stability of lithium-ion battery electrolytes. *J. Power Sources* **119**, 805-810, doi:10.1016/s0378-7753(03)00257-x (2003).

104 Plakhotnyk, A. V., Ernst, L. & Schmutzler, R. Hydrolysis in the system LiPF6-propylene carbonate-dimethyl carbonate-H2O. *J. Fluorine Chem.* **126**, 27-31, doi:10.1016/j.jfluchem.2004.09.027 (2005).

105 Kovalenko, I. *et al.* A Major Constituent of Brown Algae for Use in High-Capacity Li-ion Batteries *Science* **334 no. 6052**, 75-79 (2011).

106 Magasinki, A. *et al.* Towards Efficient Binders for Li-ion Battery Si-Based Anodes: Polyacrylic Acid. *ACS Appl. Mater. Interfaces* **2**, 3004-3010 (2010).

107 Ota, H., Sakata, Y., Inoue, A. & Yamaguchi, S. Analysis of Vinylene Carbonate Derived SEI Layers on Graphite Anode. *J. Electrochem. Soc.* **151**, A1659-A1669-A1659-A1669 (2004).

108 Abraham, D. P., Spila, T., Furczon, M. M. & Sammann, E. Evidence of Transition-Metal Accumulation on Aged Graphite Anodes by SIMS. *Electrochem. Solid-State Lett.* **11**, A226-A228-A226-A228 (2008).

109 Aurbach, D., Markovsky, B., Shechter, A., EinEli, Y. & Cohen, H. A comparative study of synthetic graphite and Li electrodes in electrolyte solutions based on ethylene carbonate dimethyl carbonate mixtures. *J. Electrochem. Soc.* **143**, 3809-3820, doi:10.1149/1.1837300 (1996).

110 Aurbach, D., Levi, M. D., Levi, E. & Schechter, A. Failure and stabilization mechanisms of graphite electrodes. *J. Phys. Chem. B* **101**, 2195-2206, doi:10.1021/jp962815t (1997).

111 Aurbach, D., Gofer, Y., Benzion, M. & Aped, P. THE BEHAVIOR OF LITHIUM ELECTRODES IN PROPYLENE AND ETHYLENE CARBONATE - THE MAJOR FACTORS THAT INFLUENCE LI CYCLING EFFICIENCY. *J. Electroanal. Chem.* **339**, 451-471, doi:10.1016/0022-0728(92)80467-i (1992).

112 Herstedt, M., Andersson, A. M., Rensmo, H., Siegbahn, H. & Edstrom, K. Characterisation of the SEI formed on natural graphite in PC-based electrolytes. *Electrochim. Acta* **49**, 4939-4947, doi:10.1016/j.electacta.2004.06.006 (2004).

113 Andersson, A. M. & Edstrom, K. Chemical composition and morphology of the elevated temperature SEI on graphite. *J. Electrochem. Soc.* **148**, A1100-A1109, doi:10.1149/1.1397771 (2001).

114 Andersson, A. M., Henningson, A., Siegbahn, H., Jansson, U. & Edstrom, K. Electrochemically lithiated graphite characterised by photoelectron spectroscopy. *J. Power Sources* **119**, 522-527, doi:10.1016/s0378-7753(03)00277-5 (2003).

115 Kang, S. H., Abraham, D. P., Xiao, A. & Lucht, B. L. Investigating the solid electrolyte interphase using binder-free graphite electrodes. *J. Power Sources* **175**, 526-532, doi:10.1016/j.jpowsour.2007.08.112 (2008).

116 Miyayama, T., Sanada, N., Bryan, S. R., Hammond, J. S. & Suzuki, M. Removal of Ar+ beam-induced damaged layers from polyimide surfaces with argon gas cluster ion beams. *Surf. Interface Anal.* **42**, 1453-1457, doi:10.1002/sia.3675 (2010).

117 Thevenin, J. G. & Muller, R. H. IMPEDANCE OF LITHIUM ELECTRODES IN A PROPYLENE CARBONATE ELECTROLYTE. *J. Electrochem. Soc.* **134**, 273-280, doi:10.1149/1.2100445 (1987).

118 Peled, E., Golodnitsky, D. & Ardel, G. Advanced model for solid electrolyte interphase electrodes in liquid and polymer electrolytes. *J. Electrochem. Soc.* **144**, L208-L210, doi:10.1149/1.1837858 (1997).

119 INEEL. FreedomCAR Battery Test Manual for Power-Assist Hybrid Electric Vechicles. (U.S. Department of Energy, 2003).

120 Bandhauer, T. M., Garimella, S. & Fuller, T. F. A Critical Review of Thermal Issues in Lithium-Ion Batteries. *Journal of The Electrochemical Society* **158**, R1-R25, doi:10.1149/1.3515880 (2011).

121 Zhang, X., Sastry, A. M. & Shyy, W. Intercalation-Induced Stress and Heat Generation within Single Lithium-Ion Battery Cathode Particles. *Journal of The Electrochemical Society* **155**, A542-A552, doi:10.1149/1.2926617 (2008).

122 Edström, K., Gustafsson, T. & Thomas, J. O. The cathode–electrolyte interface in the Li-ion battery. *Electrochim. Acta* **50**, 397-403, doi:http://dx.doi.org/10.1016/j.electacta.2004.03.049 (2004).

123 Jang, D. H., Shin, Y. J. & Oh, S. M. Dissolution of spinel oxides and capacity losses in 4V Li/LixMn2O4 coils. *J. Electrochem. Soc.* **143**, 2204-2211 (1996).

124 Gowda, S. *et al.* Oxidation State of Cross-over Manganese Species on the Graphite Electrode of Lithium-ion Cells. *PCCP*, doi:10.1039/C4CP00764F (2014).

125 Etacheri, V. *et al.* Effect of Fluoroethylene Carbonate (FEC) on the Performance and Surface Chemistry of Si-Nanowire Li-Ion Battery Anodes. *Langmuir* **28**, 965-976, doi:10.1021/la203712s (2012).

126 Zheng, H. H., Sun, Q. N., Liu, G., Song, X. Y. & Battaglia, V. S. Correlation between dissolution behavior and electrochemical cycling performance for LiNi1/3Co1/3Mn1/3O2-based cells. *J. Power Sources* **207**, 134-140, doi:10.1016/j.jpowsour.2012.01.122 (2012).

127 Han, X. *et al.* A comparative study of commercial lithium ion battery cycle life in electrical vehicle: Aging mechanism identification. *J. Power Sources* **251**, 38-54, doi:10.1016/j.jpowsour.2013.11.029 (2014).

128 Lee, J. T. *et al.* Comparative study of the solid electrolyte interphase on graphite in full Li-ion battery cells using X-ray photoelectron spectroscopy, secondary ion mass spectrometry, and electron microscopy. *Carbon* **52**, 388-397, doi:10.1016/j.carbon.2012.09.049 (2013).

129 Zhang, Q. & White, R. E. Calendar life study of Li-ion pouch cells. *J. Power Sources* **173**, 990-997, doi:10.1016/j.jpowsour.2007.08.044 (2007).

130 Broussely, M. *et al.* Aging mechanism in Li ion cells and calendar life predictions. *J. Power Sources* **97–98**, 13-21, doi:http://dx.doi.org/10.1016/S0378-7753(01)00722-4 (2001).

131 Ploehn, H. J., Ramadass, P. & White, R. E. Solvent diffusion model for aging of lithium-ion battery cells. *J. Electrochem. Soc.* **151**, A456-A462, doi:Doi 10.1149/1.1644601 (2004).

132 Wright, R. B. *et al.* Calendar- and cycle-life studies of advanced technology development program generation 1 lithium-ion batteries. *J. Power Sources* **110**, 445-470, doi:Pii S0378-7753(02)00210-0 (2002).

133 Stiaszny, B. *et al.* Electrochemical characterization and post-mortem analysis of aged LiMn2O4–NMC/graphite lithium ion batteries part II: Calendar aging. *J. Power Sources* **258**, 61-75, doi:http://dx.doi.org/10.1016/j.jpowsour.2014.02.019 (2014).

134 Ecker, M. *et al.* Calendar and cycle life study of Li(NiMnCo)O2-based 18650 lithium-ion batteries. *J. Power Sources* **248**, 839-851, doi:http://dx.doi.org/10.1016/j.jpowsour.2013.09.143 (2014).

135 Bloom, I., Potter, B. G., Johnson, C. S., Gering, K. L. & Christophersen, J. P. Effect of cathode composition on impedance rise in high-power lithium-ion cells: Long-term aging results. *J. Power Sources* **155**, 415-419, doi:10.1016/j.jpowsour.2005.05.008 (2006).

136 Joshi, T., Eom, K., Yushin, G. & Fuller, T. F. Effects of Dissolved Transition Metals on the Electrochemical Performance and SEI Growth in Lithium-Ion Batteries. *J. Electrochem. Soc.* **161**, A1915-A1921, doi:10.1149/2.0861412jes (2014).

137 Eom, K., Joshi, T., Bordes, A., Do, I. & Fuller, T. F. The design of a Li-ion full cell battery using a nano silicon and nano multi-layer graphene composite anode. *J. Power Sources* **249**, 118-124, doi:http://dx.doi.org/10.1016/j.jpowsour.2013.10.087 (2014).

138 Gao, J., Lowe, M. A., Kiya, Y. & Abruña, H. D. Effects of Liquid Electrolytes on the Charge–Discharge Performance of Rechargeable Lithium/Sulfur Batteries: Electrochemical and in-Situ X-ray Absorption Spectroscopic Studies. *The Journal of Physical Chemistry C* **115**, 25132-25137, doi:10.1021/jp207714c (2011).

139 Yim, T. *et al.* Effect of chemical reactivity of polysulfide toward carbonate-based electrolyte on the electrochemical performance of Li–S batteries. *Electrochim. Acta* **107**, 454-460, doi:http://dx.doi.org/10.1016/j.electacta.2013.06.039 (2013).

140 Suo, L., Hu, Y.-S., Li, H., Armand, M. & Chen, L. A new class of Solvent-in-Salt electrolyte for high-energy rechargeable metallic lithium batteries. *Nat Commun* **4**, 1481, doi:http://www.nature.com/ncomms/journal/v4/n2/suppinfo/ncomms2513_S1.html (2013).

141 Scheers, J., Fantini, S. & Johansson, P. A review of electrolytes for lithium–sulphur batteries. *J. Power Sources* **255**, 204-218, doi:http://dx.doi.org/10.1016/j.jpowsour.2014.01.023 (2014).

142 Zhang, S., Ueno, K., Dokko, K. & Watanabe, M. Recent Advances in Electrolytes for Lithium–Sulfur Batteries. *Advanced Energy Materials* **5**, n/a-n/a, doi:10.1002/aenm.201500117 (2015).

143 Han, H.-B. *et al.* Lithium bis(fluorosulfonyl)imide (LiFSI) as conducting salt for nonaqueous liquid electrolytes for lithium-ion batteries: Physicochemical and electrochemical properties. *J. Power Sources* **196**, 3623-3632, doi:http://dx.doi.org/10.1016/j.jpowsour.2010.12.040 (2011).

144 Qian, C. *et al.* Solution-Phase Synthesis of Single-Crystalline Iron Phosphide Nanorods/Nanowires. *J. Am. Chem. Soc.* **126**, 1195-1198, doi:10.1021/ja038401c (2004).

145 Qian, J. *et al.* High rate and stable cycling of lithium metal anode. *Nat Commun* **6**, doi:10.1038/ncomms7362 (2015).

146 Toy, A. D. F. in *The Chemistry of Phosphorus* Vol. 3 389-406 (Pergamon, 1973).

147 Corbridge, D. E. C. & Lowe, E. J. Structure of White Phosphorus: Single Crystal X-Ray Examination. *Nature* **170**, 629-629 (1952).

148 Kawashima, K., Ding, J. Z., Hosono, H. & Abe, Y. Electrical Properties of Silver Photodoped Amorphous Red Phosphorus. *Phosphorus, Sulfur, and Silicon and the Related Elements* **51**, 157-160, doi:10.1080/10426509008040705 (1990).

149 Peck, D. R. *Supplement III, Phosphorus*. 149–227 (John Wiley & Sons, 1971).

150 Thurn, H. & Kerbs, H. Crystal Structure of Violet Phosphorus. *Angewandte Chemie International Edition in English* **5**, 1047-1048, doi:10.1002/anie.196610473 (1966).

151 Bridgman, P. W. TWO NEW MODIFICATIONS OF PHOSPHORUS. *J. Am. Chem. Soc.* **36**, 1344-1363, doi:10.1021/ja02184a002 (1914).

152 Bachmann, K. J. & Buehler, E. Phase Equilibria and Vapor Pressures of Pure Phosphorus and of the Indium/Phosphorus System and Their Implications Regarding Crystal Growth of InP. *J. Electrochem. Soc.* **121**, 835-846, doi:10.1149/1.2401931 (1974).

153 DeWitt, D. C. in *Phosphorus* Vol. 36 (ed John J. McKetta Jr) (CRC Press, 1990).

154 Plucker, J. & Hittorf, J. W. On the Spectra of Ignited Gases and Vapours, with Especial Regard to the Different Spectra of the Same Elementary Gaseous Substance. *Philosophical Transactions of the Royal Society of London* **155**, 1-29, doi:10.1098/rstl.1865.0001 (1865).

155 Li, L. *et al.* Black phosphorus field-effect transistors. *Nat Nano* **9**, 372-377, doi:10.1038/nnano.2014.35

156 Favron, A. *et al.* Photooxidation and quantum confinement effects in exfoliated black phosphorus. *Nat. Mater.* **14**, 826-832, doi:10.1038/nmat4299

157 Andres, C.-G. *et al.* Isolation and characterization of few-layer black phosphorus. *2D Materials* **1**, 025001 (2014).

158 Akahama, Y., Kobayashi, M. & Kawamura, H. Simple-cubic\char21{}simple-hexagonal transition in phosphorus under pressure. *Physical Review B* **59**, 8520-8525 (1999).

159 Clark, S. M. & Zaug, J. M. Compressibility of cubic white, orthorhombic black, rhombohedral black, and simple cubic black phosphorus. *Physical Review B* **82**, 134111 (2010).

160 Nilges, T., Kersting, M. & Pfeifer, T. A fast low-pressure transport route to large black phosphorus single crystals. *J. Solid State Chem.* **181**, 1707-1711, doi:http://dx.doi.org/10.1016/j.jssc.2008.03.008 (2008).

161 Maruyama, Y., Suzuki, S., Kobayashi, K. & Tanuma, S. Synthesis and some properties of black phosphorus single crystals. *Physica B+C* **105**, 99-102, doi:http://dx.doi.org/10.1016/0378-4363(81)90223-0 (1981).

162 Park, C. M. & Sohn, H. J. Black phosphorus and its composite for lithium rechargeable batteries. *Adv. Mater.* **19**, 2465-+, doi:10.1002/adma.200602592 (2007).

163 Yu, X.-f., Ushiyama, H. & Yamashita, K. Comparative Study of Sodium and Lithium Intercalation and Diffusion Mechanism in Black Phosphorus from First-principles Simulation. *Chem. Lett.* **43**, 1940-1942, doi:10.1246/cl.140741 (2014).

164 Li, W., Yang, Y., Zhang, G. & Zhang, Y.-W. Ultrafast and Directional Diffusion of Lithium in Phosphorene for High-Performance Lithium-Ion Battery. *Nano Lett.* **15**, 1691-1697, doi:10.1021/nl504336h (2015).

165 Nazri, G. Preparation, structure and ionic conductivity of lithium phosphide. *Solid State Ionics* **34**, 97-102, doi:http://dx.doi.org/10.1016/0167-2738(89)90438-4 (1989).

166 Sun, L.-Q. *et al.* Electrochemical Activity of Black Phosphorus as an Anode Material for Lithium-Ion Batteries. *The Journal of Physical Chemistry C* **116**, 14772-14779, doi:10.1021/jp302265n (2012).

167 Stan, M. C., Zamory, J. v., Passerini, S., Nilges, T. & Winter, M. Puzzling out the origin of the electrochemical activity of black P as a negative electrode material for lithium-ion batteries. *Journal of Materials Chemistry A* **1**, 5293-5300, doi:10.1039/c3ta10380c (2013).

168 Qian, J., Qiao, D., Ai, X., Cao, Y. & Yang, H. Reversible 3-Li storage reactions of amorphous phosphorus as high capacity and cycling-stable anodes for Li-ion batteries. *Chemical communications (Cambridge, England)* **48**, 8931-8933, doi:10.1039/c2cc34388f (2012).

169 Cheol-Min, P. *et al.* High-Rate Capability and Enhanced Cyclability of Antimony-Based Composites for Lithium Rechargeable Batteries. *J. Electrochem. Soc.* **154**, doi:10.1149/1.2761829 (2007).

170 Darwiche, A. *et al.* Better Cycling Performances of Bulk Sb in Na-Ion Batteries Compared to Li-Ion Systems: An Unexpected Electrochemical Mechanism. *J. Am. Chem. Soc.* **134**, 20805-20811, doi:10.1021/ja310347x (2012).

171 Sun, J. *et al.* Formation of Stable Phosphorus–Carbon Bond for Enhanced Performance in Black Phosphorus Nanoparticle–Graphite Composite Battery Anodes. *Nano Lett.* **14**, 4573-4580, doi:10.1021/nl501617j (2014).

172 Li, W.-J., Chou, S.-L., Wang, J.-Z., Liu, H.-K. & Dou, S.-X. Simply Mixed Commercial Red Phosphorus and Carbon Nanotube Composite with Exceptionally Reversible Sodium-Ion Storage. *Nano Lett.* **13**, 5480-5484, doi:10.1021/nl403053v (2013).

173 Korolev, V. V., Talanov, N. D. & Astakhova, G. V. MECHANISM OF OXIDATION OF RED PHOSPHORUS BY OXYGEN IN AIR. *Inorg. Mater.* **22**, 1063-1064 (1986).

174 Shechkov, G. T., Domin, A. V. & Neskorodova, N. M. LOW-TEMPERATURE OXIDATION OF RED PHOSPHORUS. *Russ. J. Appl. Chem.* **66**, 1501-1504 (1993).

175 Whitehead, A. H. & Schreiber, M. Current Collectors for Positive Electrodes of Lithium-Based Batteries. *J. Electrochem. Soc.* **152**, A2105-A2113, doi:10.1149/1.2039587 (2005).

176 Ichitsubo, T. *et al.* Influence of Mechanical Strain on the Electrochemical Lithiation of Aluminum-Based Electrode Materials. *J. Electrochem. Soc.* **159**, A14-A17, doi:10.1149/2.038201jes (2011).

177 Liu, Y. *et al.* In Situ Transmission Electron Microscopy Observation of Pulverization of Aluminum Nanowires and Evolution of the Thin Surface Al2O3 Layers during Lithiation-Delithiation Cycles. *Nano Lett.* **11**, 4188-4194, doi:10.1021/nl202088h (2011).

178 Zhang, S. S. A review on electrolyte additives for lithium-ion batteries. *J. Power Sources* **162**, 1379-1394, doi:http://dx.doi.org/10.1016/j.jpowsour.2006.07.074 (2006).

179 Li, J., Christensen, L., Obrovac, M. N., Hewitt, K. C. & Dahn, J. R. Effect of heat treatment on Si electrodes using polyvinylidene fluoride binder. *J. Electrochem. Soc.* **155**, A234-A238, doi:10.1149/1.2830545 (2008).

180 Li, J., Dahn, H. M., Krause, L. J., Le, D.-B. & Dahn, J. R. Impact of Binder Choice on the Performance of α-Fe2O3 as a Negative Electrode. *J. Electrochem. Soc.* **155**, A812-A816, doi:10.1149/1.2969433 (2008).

181 Gordon, D. *et al.* Enhancing Cycle Stability of Lithium Iron Phosphate in Aqueous Electrolytes by Increasing Electrolyte Molarity. *Advanced Energy Materials* **6**, n/a-n/a, doi:10.1002/aenm.201501805 (2016).

182 Ramanujapuram, A. *et al.* Degradation and stabilization of lithium cobalt oxide in aqueous electrolytes. *Energy & Environmental Science* **9**, 1841-1848, doi:10.1039/c6ee00093b (2016).

183 Koo, B. *et al.* A Highly Cross-Linked Polymeric Binder for High-Performance Silicon Negative Electrodes in Lithium Ion Batteries. *Angewandte Chemie-International Edition* **51**, 8762-8767, doi:10.1002/anie.201201568 (2012).

184 Ryou, M.-H. *et al.* Mussel-Inspired Adhesive Binders for High-Performance Silicon Nanoparticle Anodes in Lithium-Ion Batteries. *Adv. Mater.* **25**, 1571–1576, doi:10.1002/adma.201203981 (2013).

185 Song, J. *et al.* Advanced Sodium Ion Battery Anode Constructed via Chemical Bonding between Phosphorus, Carbon Nanotube, and Cross-Linked Polymer Binder. *ACS Nano* **9**, 11933-11941, doi:10.1021/acsnano.5b04474 (2015).

186 Socrates, G. *Infrared and Raman Characteristic Group Frequencies: Tables and Charts*. 3rd edn, (John Wiley & Sons Ltd., 2004).

187 Arndt, K. F. *et al.* Poly(vinyl alcohol)/poly(acrylic acid) hydrogels: FT-IR spectroscopic characterization of crosslinking reaction and work at transition point. *Acta Polym.* **50**, 383-390, doi:10.1002/(sici)1521-4044(19991201)50:11/12<383::aid-apol383>3.0.co;2-z (1999).

188 Eisenberg, A., Yokoyama, T. & Sambalido, E. Dehydration kinetics and glass transition of poly(acrylic acid). *Journal of Polymer Science Part A-1: Polymer Chemistry* **7**, 1717-1728, doi:10.1002/pol.1969.150070714 (1969).

189 Cox, B. G. *Acids and Bases: Solvent Effects On Acid-Base Strength*. (Oxford University Press, 2013).

190 Burns, J. C. *et al.* The Impact of Intentionally Added Water to the Electrolyte of Li-ion Cells: I. Cells with Graphite Negative Electrodes. *J. Electrochem. Soc.* **160**, A2281-A2287, doi:10.1149/2.101311jes (2013).

191 Wang, J., Eng, C., Chen-Wiegart, Y.-c. K. & Wang, J. Probing three-dimensional sodiation-desodiation equilibrium in sodium-ion batteries by in situ hard X-ray nanotomography. *Nat Commun* **6**, doi:10.1038/ncomms8496 (2015).

192 Weker, J. N. *et al.* In situ nanotomography and operando transmission X-ray microscopy of micron-sized Ge particles. *Energy & Environmental Science* **7**, 2771-2777, doi:10.1039/c4ee01384k (2014).

193 Feng, X. *et al.* Scalable shear-exfoliation of high-quality phosphorene nanoflakes with reliable electrochemical cycleability in nano batteries. *2D Materials* **3**, 025005 (2016).

194 MicroFab. *Ion Beam Etch Rates*, <http://www.microfabnh.com/ion_beam_etch_rates.php>